



Water-tightness Airborne Detection Implementation

D3.1 Definition of optimal wavelengths and cameras for service provision

Authors:

ONERA : Frédéric Y-M, Chatelard C, Barillot P, Krapez J.-C, Louvet Y, Hélias F, Ph. Déliot

SCP: I. Le Goff, J-F. Puigt, G. Serra



This project has received funding from the European Union's Horizon 2020 research and innovation programme under grant agreement No 689239.

Technical references

Project Acronym	WADI
Project Title	Water-tightness Airborne Detection Implementation
Project Coordinator	Elena Gaboardi, youris.com (YOURIS) elena.gaboardi@youris.com
Project Duration	October 2016 – March 2020 (42 months)
Deliverable No.	D3.1
Dissemination level*	PU
Work Package	WP 3 - Demonstration of Airborne Innovative Techniques
Task	T 3.1 –Definition of optimal wavelengths and cameras
Lead beneficiary	2 (ONERA)
Contributing beneficiary/ies	1 (YOURIS) - 6 (SCP) - 7 (NTGS) - 11 (GG)
Due date of deliverable	31 July 2017
Actual submission date	v1.0: 2 August 2017 – v1.2: 31 October 2017

PU = Public

PP = Restricted to other programme participants (including the Commission Services)

RE = Restricted to a group specified by the consortium (including the Commission Services)

CO = Confidential, only for members of the consortium (including the Commission Services)

D3.1 Definition of optimal wavelengths and cameras

v	Date	Beneficiary	Author
1.0	13/07/2017	ONERA	Chatelard C., Frédéric Y.-M, Krapez JC., Hélias F., Louvet Y., Barillot Ph., Déliot Ph.
1.0	13/07/2017	SCP	I. Le goff, JF. Puigt,G. Serra.
1.0	13/07/2017	NTGS	Ramirez I., Estrella J., Correia E.
1.0	13/07/2017	Galileo GeoSystems	Barba J., Sanchis J.
1.0	31/07/2017	YOURIS	Gaboardi E., Schmid E.
1.1	20/10/2017	ONERA	Chatelard C.
1.2	31/10/2017	YOURIS	Gaboardi E., Barbieri A., Meneghello V.

D3.1 Definition of optimal wavelengths and cameras



Disclaimer

This project has received funding from the European Union's Horizon 2020 research and innovation programme under grant agreement No 689239.

The sole responsibility for the content of this report lies with the authors. It does not necessarily reflect the opinion of the European Union. The European Commission is not responsible for any use that may be made of the information contained therein.

Executive Summary

1 TRIALS USING AERIAL HYPERSPECTRAL/IR PLATFORM

The development of an airborne water leak detection surveillance service requires the stage of determining the optimized detection wavelength. The wavelength determination process involves an optical hyper-spectral camera used in measurement campaign and WADI took the advantage of the availability of ONERA's aerial platform called BUSARD, instrumented by two hyper-spectral and one IR imaging devices to collect hyperspectral/IR images database.

The airborne tests have been conducted over several areas belonging to the water network infrastructure provided by SCP. SCP and ONERA have defined at the beginning of the WP3 a strategy of selection of the areas of interest as a function of:

- the period of the airborne measurement (February, April, and July),
- requirements for the data processing (methods proposed by ONERA)
- end-users requirements inside D2-1 report

The validity and the robustness of the data processing for the soil humidity detection by optical remote sensing also depend on ground truth measurement. A set of instrumentation has been deployed during the BUSARD campaign to measure physical parameters on the ground.

2 TRIALS ASSESSMENT, OPTIMIZED DETECTION WAVELENGTHS DETERMINATION AND MEASUREMENT STRATEGY

The trials of the BUSARD campaign (WADI-1, WADI-2 & WADI-3) represent the WADI images database for the determination of optimized wavelengths for leakage detection. All these trials require an assessment before the extraction and the exploitation of the relevant physical parameters from the database. Once the measures corrected and validated, the results are employed by the triangle/trapezoid method [2.3.1] for soil moisture evaluation (humidity maps). At the end, a set of optimized detection wavelengths is determined as a function of the corresponding trials (soil and vegetation) and a measurement strategy is designed. This strategy provides guidance for physical effect observation.

3 MULTISPECTRAL AND IR CAMERAS SELECTION

Based on requirements elaborated in WP2, this Subtask has led to the establishment of an overall requirements collection consisting of some high level functional and non-functional requirements. Building on this set of requirements, recommendations for the optimal selection of a flying VNIR multi-spectral/IR cameras payload have been issued.



D3.1 Definition of optimal wavelengths and cameras

The outcome of this subtask will be useful as a starting point to write the Technical Specification documents for the cameras and other necessary complementary components (IMU, gyro stabilizing mounts, onboard computing system...), which will provide documentation to prospective cameras providers. These points that will constrain the architecture of the system will be defined based also on requirements elaborated in WP2, on-board platform constraints, and other relevant considerations (e.g. the easiness of use, best value for money, best time to deliver...).

The most promising infrared and multi-spectral cameras existing in the market and operating at the optimized wavelength defined under Task 3.1.1 will then be selected and purchased.



Table of Content

Foreword.....	1
1 Trials using aerial hyperspectral/IR platform.....	3
1.1 BUSARD flight campaigns description.....	3
1.1.1 Objective.....	3
1.1.2 Demonstration Sites selection.....	3
1.1.3 Instrumentation implemented.....	12
1.1.4 Areas of interest.....	13
1.2 Airborne measurements.....	14
1.2.1 WADI 1 campaign.....	14
1.2.2 WADI 2 campaign.....	20
1.2.3 WADI 3 campaign.....	22
1.3 Ground truth measurements.....	24
1.3.1 WADI 1 campaign.....	24
1.3.2 WADI 2 campaign.....	28
1.3.3 Acoustic and ground investigation on Esparron site.....	32
1.3.4 WADI 3 campaign.....	35
1.4 Conclusion.....	37
2 Trials assessment, optimized detection wavelengths determination and measurement strategy.....	39
2.1 Introduction.....	39
2.2 Pre-processing of airborne optical remote sensing.....	39
2.2.1 Hyperspectral data pre processing.....	39
2.2.2 IR pre-data processing.....	42
2.2.3 Registration of pre-processed images data.....	45
2.3 Data processing for getting information on the water presence in soil or in vegetation.....	46
2.3.1 Principle of the "trapezoid" method with different variants.....	46
2.3.2 Other Water Indexes.....	52
2.4 WADI 1 Campaign.....	53



D3.1 Definition of optimal wavelengths and cameras

2.4.1	Application of the VI-TIR Trapezoid method to Esparron and St Maximin data	53
2.4.2	Assessment of other Water Indexes to Esparron data.....	59
2.4.3	Comparison of the results	70
2.5	WADI 2 Campaign.....	71
2.5.1	Le Tholonet	71
2.5.2	Rians.....	77
2.5.3	Vauvenargues.....	80
2.5.4	Saint-Maximin	84
2.6	Conclusion	85
2.7	WADI 3 Campaign.....	85
2.8	Optimized detection wavelengths determination	86
2.9	Measurement strategy	87
2.9.1	The nature of the effect observed.....	87
2.9.2	The surveillance constraints and requirements from water provider	87
2.9.3	Data processing requirements	88
2.9.4	Complementary use of aircraft and UAV platform	88
3	Multispectral and IR cameras selection.....	89
3.1	Identification of the requirements for the airborne multi-spectral/IR cameras	89
3.1.1	Requirements	90
3.1.2	Constraints	92
3.2	Recommendations for the optimal selection of a flying multi-spectral/IR cameras and IMU payload.....	93
3.2.1	IR camera	93
3.2.2	Multispectral VNIR/SWIR camera	94
3.2.3	Inertial Measurement Unit (IMU) and GPS.....	94
4	Conclusions	96
5	References	99
6	Annex 1: Potential IR sensor candidates.....	1
7	Annex 2: Potential VNIR/SWIR multispectral sensor candidates.....	2

List of Acronyms

BUSARD	Banc d'essais Ultra léger pour Systèmes Aéroportés de Recherche sur les Drones
GCP	Ground Control Point
IMU	Inertial Measurement Unit
IR	InfraRed
LWIR	Long Wave InfraRed ([8.0-12.0 μm] waveband)
SMC	Soil Moisture Content
MSL	Mean Sea Level
NDVI	Normalized Difference Vegetation Index
SCP	Société du Canal de Provence
SWIR	Short Wavelength InfraRed ([1.0-2.5 μm] waveband)
S/N	Signal to Noise ratio
UAV	Unmanned Aerial Vehicle
VNIR	Visible and Near InfraRed ([0.4-1.0 μm] waveband)
WP n	Work Package n
DEM	Digital Elevation Model
NETD	Noise Equivalent Temperature Difference



Foreword

WADI is a H2020 funded project (Grant Agreement No. 689239) aimed at developing an airborne water leak detection surveillance service in water transportation infrastructures. The project relies on an innovative concept of coupling and optimising off-the-shelf optical remote sensing devices and their application on two complementary aerial platforms - manned and unmanned. These platforms are used for distinctive purposes in infrastructure performance observation, i.e.: long distance and strategic infrastructure monitoring, and difficult and/or dangerous areas observation.

The current deliverable D3.1 "*Definition of optimal wavelengths and cameras for service provision*" belongs to Work Package 3 viz. "*Demonstration of Airborne Innovative Techniques*", which primary aim is to provide all elements necessary for the airborne operational environment demonstration of the WADI concept at the two pilot sites of the project (WP5 and WP6).

The airborne measurement campaigns using hyperspectral/IR platform will serve as a basis to determine the optimized detection wavelengths. Under this WP the most suitable, existing (off-the-shelf) cameras operating at the defined wavelengths will be selected and purchased. Other components necessary for the system airborne use, such as on-board computing, inertial platform, and integration console, will be defined and supplied. The selected cameras will be adapted/ integrated/ validated on the manned and the UAV platform. The proposed in-flight validation will result in the availability of an instrumented platform, and will provide preliminary data measurements for the data processing task.

Deliverable D3.1 specifically refers to the outcome of Subtasks 3.1.1, 3.1.2 and 3.1.3, as detailed below.

- Subtask 3.1.1. *Trials using aerial hyper-spectral /IR platform* have led to the development of hyperspectral (VNIR and SWIR spectral domains) and TIR panchromatic images database from which the relevant physical parameters (soil temperature, spectral reflectance...) have been extracted (subtask 3.1.2). Airborne measurements were conducted over several areas belonging to the water network infrastructure provided by SCP with ONERA's aerial platform (BUSARD) instrumented with two hyperspectral and one infrared cameras.
- Subtask 3.1.2 *Trials assessment, optimized detection wavelengths determination and measurement strategy*. Trials have been assessed for the three parts of the BUSARD campaign (WADI-1, WADI-2 & WADI-3) and the images database has been prepared for the WADI data processing. The results achieved with the two first parts of the BUSARD campaign (WADI-1, WADI-2) have been analysed and compared in order to determine the best wavelengths for the water leakage detection. Due to a lack of time, the last series of measurements performed in July (WADI-3) will be processed later and will be used for the validation cases of smart data processing delivered by the WP4. The measurement strategy has been refined and takes into account several requirements also defined in the GA and



complemented by the return on experience of the BUSARD campaign (airborne measurement & data processing).

- Subtask 3.1.3 *Multi-spectral and IR cameras selection* has led to identification of an overall requirements collection consisting of some high level functional and non-functional (operational and interface) requirements. Selected requirements are distributed in several categories according to airborne cameras architecture: general, sensors, control/command and data acquisition, airborne platform. Building on this set of requirements, recommendations for the optimal selection of a flying VNIR multi-spectral/IR cameras payload have been issued. The outcome of this subtask will be useful as a starting point to write the Technical Specification documents for the cameras and other necessary complementary components (IMU...)

The report preparation has been coordinated by ONERA, with key content inputs from SCPand with active collaboration from NTGS and GG.



1 Trials using aerial hyperspectral/IR platform

WADI develops an airborne water leak detection surveillance service in water transportation infrastructures. The project relies on an innovative concept of coupling and optimising off-the-shelf optical remote sensing devices and their application on two complementary aerial platforms - manned and unmanned. The platforms are used for distinctive purposes in infrastructure performance observation, i.e.: long distance and strategic infrastructure monitoring, and difficult and/or dangerous areas observation.

This section focuses on the airborne field campaigns conducted with ONERA's BUSARD instrumented aerial platform over several areas belonging to the water network infrastructure provided by SCP.

1.1 BUSARD flight campaigns description

1.1.1 Objective

The objective of BUSARD flight campaigns is to collect hyperspectral (VNIR/SWIR) and IRT images database for the optimized detection wavelengths determination for the future WADI prototype (water leaks detection in water transportation infrastructures outside urban areas).

1.1.2 Demonstration Sites selection

1.1.2.1 WADI 1 campaign – February 2017

For the organisation of this first flight campaign, SCP has selected parts of its network with a high probability to encounter water leaks or high moisture areas.

To do so, at first, water balance figures of 2015 were used. The global efficiency ratio of SCP in 2015 was 88%. Nine water intakes were identified with efficiency ratio of associated networks lower than 80%, and 3 parts of distribution networks depending from our main water intake (Boutre) had efficiency ratio of distribution lower than 80%.

Some of these identified points were not selected for the following reasons:

- Flow meter accuracy is probably involved in low efficiency ratio,
- Urban areas not suitable for WADI devices
- Distribution networks with many junctions between the main without flowmeters,
- Networks with very small volumes,
- Areas far from Salon airport and difficult to explore with BUSARD platform
- High probability of leakage localisation under a river
- Aerial pipe.

Finally, two areas have been identified as interesting for their low water balance probably due to water leakages:

- “Cabardèle”, with an expected leakage rate of 3 to 4 l/s (leakage rate is estimated with night measurements of the tank level during winter).
- “St Marc Jaumegarde”, with an expected leakage rate of 2 l/s.



Figure 1: Cabardèle area.



Figure 2: St Marc Jaumegarde area.

To complete this selection, we selected other networks where field operators have identified high probability of leakage:

- “Valtrede” area where SCP has encountered chronic problems of breaks and seal leakages with a feeder (flags in the map bellow correspond to breaks events in the past ten years).
- “Esparron” (83) where SCP operating center has been alerted by high moisture area not far from the pipes localization.

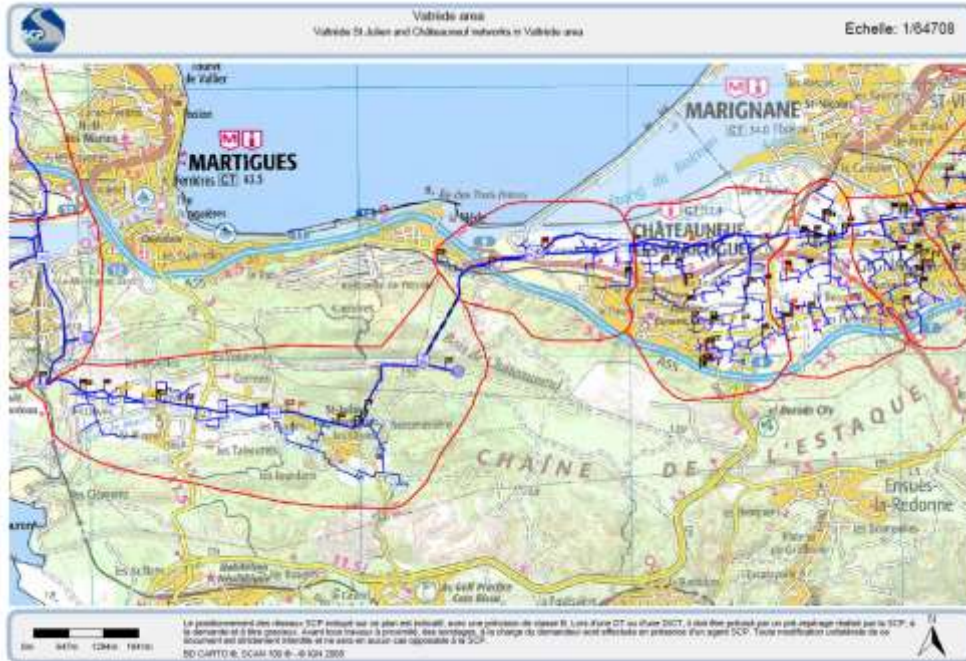


Figure 3: Valtrede area.

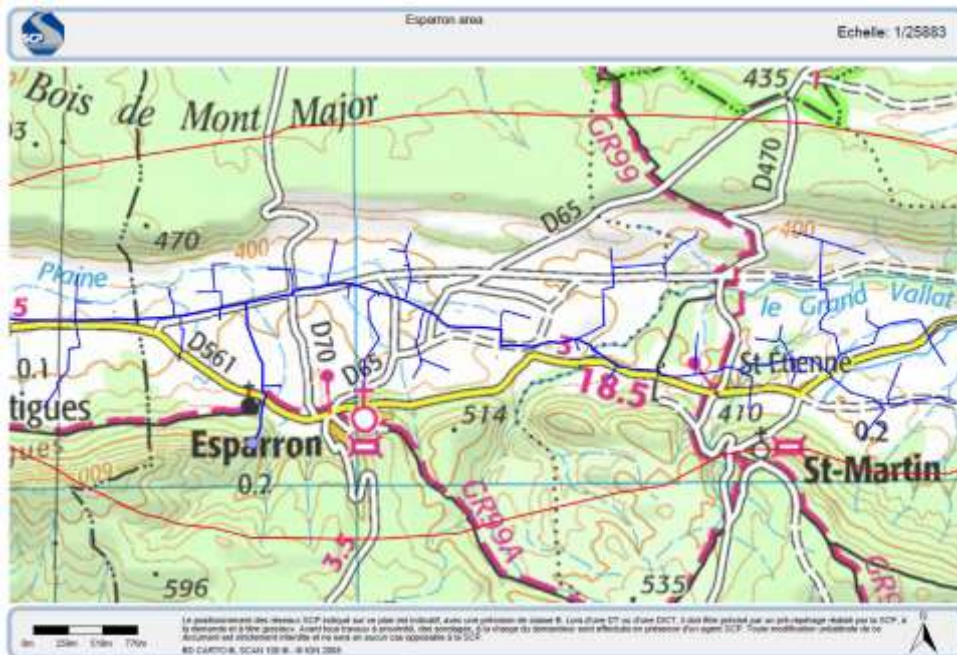


Figure 4: Esparron area.

Finally, since end-user requirements report (D2.1) has identified an expected service provided by surveillance about “leak detection on canals and evolution of cracks associated, two open channel sites were selected:

- The Pigoudet open channel in Rians area, which is quite an old one. The canal is equipped with a drainage system. The outlets of this drainage system were pointed in the map because they are areas with a good probability of high moisture content.
- The St Maximin open channel, which presents many cracks and which refurbishment with a bituminous lining is planned between the first and the second flight campaign.



Figure 5: Pigoudet open channel with localization of drainage system outlets.



Figure 6: St Maximin open channel before and after refurbishment.

To increase the probability of high moisture areas detection during the flights:

- A fire hydrant was opened in Cabardèle area a few hours before the flight,
- The level of the Pigoudet canal (Rians) was increased a few days before the flights in order to increase the flow rate of drainage system outlets.



Figure 7: Fire hydrant opened in Cabardèle before the flight

1.1.2.2 WADI 2 campaign – April 2017

To be sure to meet water leaks during this campaign, SCP has built artificial water leaks. To choose the sites for these artificial leaks, SCP has selected plots according to several criteria:

- The owner of the plot is SCP (700 plots)
- The kind of pipe (size and material) is suitable for easily connecting a new pipe.
- Distance from operating center and Salon airport
- Flat ground
- Short vegetation.

A short list of 10 plots has been visited by SCP team and 5 areas have been proposed to ONERA. Finally, the sites of Tholonet, Vauvenargues and Rians have been selected.



Figure 8: Tholonet site – DN80 – Grey cast Iron

In these three areas, new pipes in high density polyethylene DN 32, 40 and 50 have been connected to the existing pipe and buried at a depth of about 1 meter. The connection with the existing pipe was equipped with valve, flow meter, recorder and a pressure regulator. Calibrated holes were drilled in this new pipe to generate leakages. The diameter of those holes allows various leakage flows according to D2-1 report's level.



Figure 9: Vauvenargues site – DN100 Ductile Iron.



Figure 10: Rians site – DN150 Ductile Iron.

	Pressure : 1 bar	Pressure : 10 bars
Diameter : 5mm	0,5 m ³ /h	1,4 m ³ /h
Diameter : 10 mm	1,4 m ³ /h	8,3 m ³ /h

Table 1: Theoretical leak flows.

In Vauvenargues and Rians sites, it was possible to bury a long pipe with several holes of various diameters and positions.

Site	Number of holes and distance between them	Diameter of holes	Maximum flow rate	Position of holes
Tholonet	1	10 mm	1,4m ³ /h for 1 bar	side
Vauvenargues	4-15m	10 mm 5 mm	1,4m ³ /h for 1 bar 1,4m ³ /h for 10 bar	Side and Bottom
Rians	2-15 m	10 mm	1,4m ³ /h for 1 bar	Side and Bottom

Table 2: Characteristics of the pipes in Vauvenargues and Rians sites.

In each site, a control zone with similar dig works but without any pipe buried has been used to evaluate dig works effects.

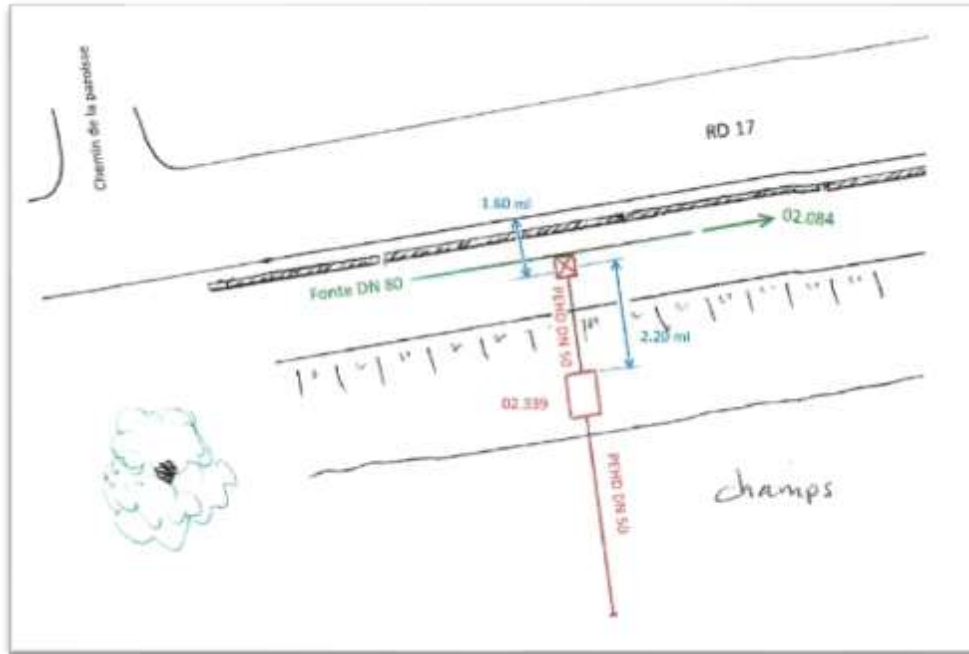


Figure 11: Installation diagram – Tholonet site -1 lateral hole of 10 mm diameter

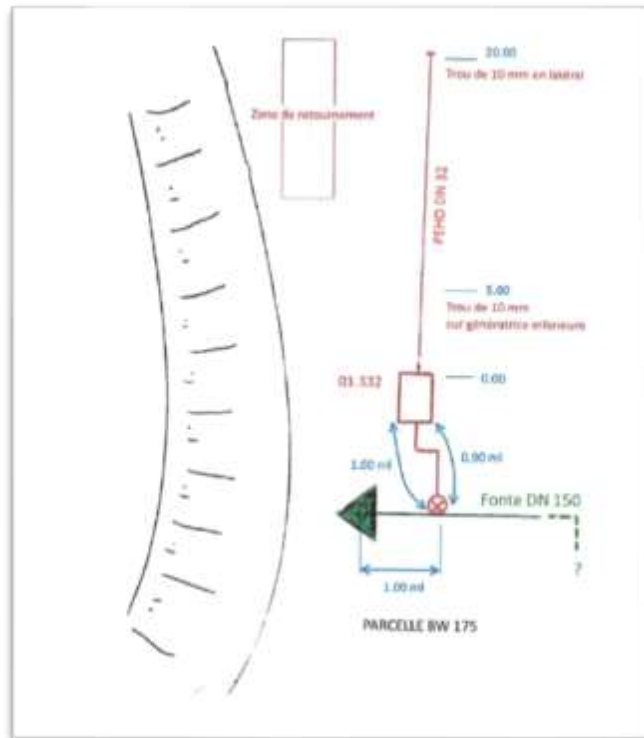


Figure 12: Installation diagram – Rians site.

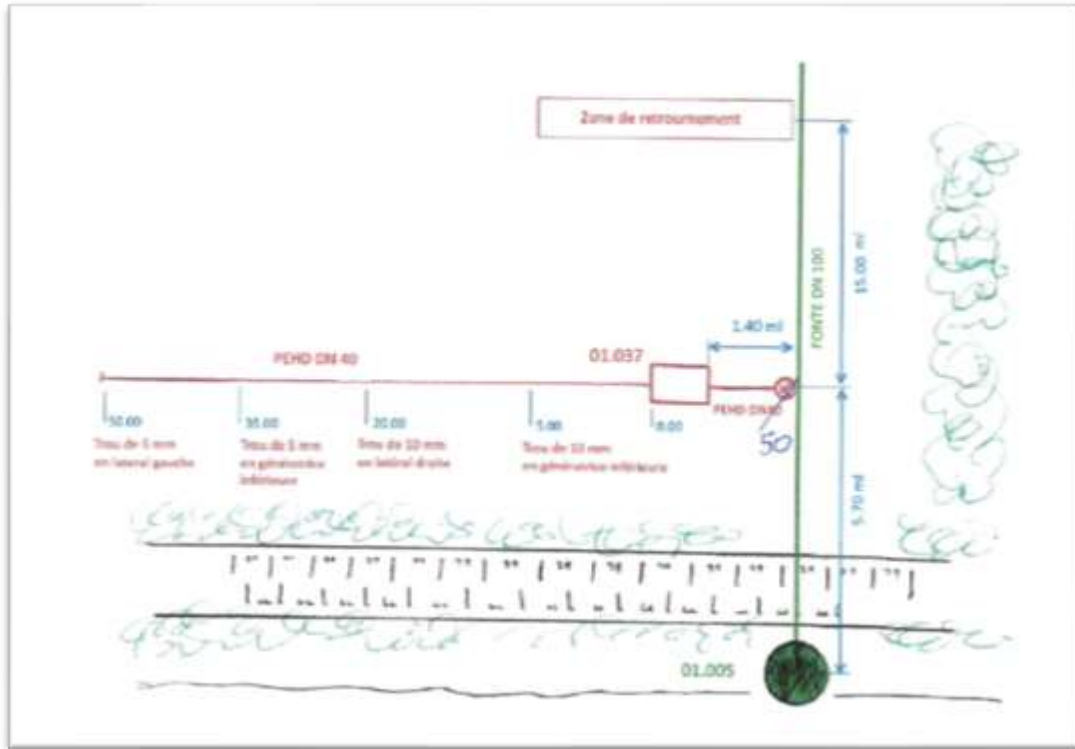


Figure 13: Installation diagram – Vauvenargues site.



Figure 14: Artificial water leaks works : connection with existing pipe, trench for new pipe, hole for leak.



Figure 15: Control zone.

A month after the dig works, we opened the valve and started the flow trials. According to D2-1 report we started with a flow of $0,8\text{m}^3/\text{h}$ but after $1/4\text{h}$, puddles appeared on the ground, and the manhole was flooded. So, we had to adapt the flow rate target to obtain high moisture areas but not puddles. This was achieved with flow rates between $0,1$ and $0,25\text{ m}^3/\text{h}$.



Figure 16: Excessive flowrate effects.



Figure 17: Ground effect of limited flowrate.

1.1.3 Instrumentation implemented

1.1.3.1 Airborne sensors

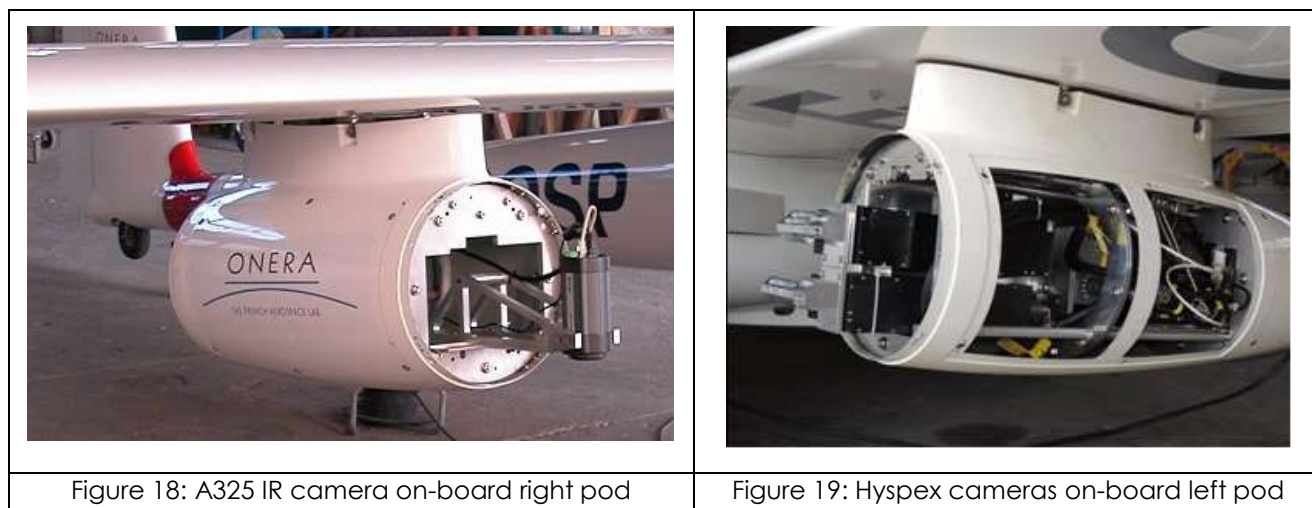
The main technical specifications of the airborne hyperspectral and infrared cameras are given in the following table.

Technical features	Hypex VNIR	Hypex SWIR	FLIR A325 ¹	FLIR A655sc ²
Acquisition mode	Push-broom	Push-broom	Snapshot	Snapshot
Number of pixels	1600	320	320x240	640x480
Waveband	0.4-1.0 μm	1.0-2.5 μm	8-14 μm	8-14 μm
Number of spectral bands	160	256	1	1
Spectral resolution	3.7 nm	6 nm	-	-
Viewing geometry	Nadir-looking	Nadir-looking	Nadir-looking	Nadir-looking
Swath width @ 800 m (AGL)	239 m	194 m	355 x 266 m	355 x 266 m
Pitch on the ground @ 800 m	0.15 x 0.30 m	0.60 x 0.60 m	1.10 x 1.10 m	0.55 x 0.55 m

Table 3: Hyperspectral and IR cameras specifications

FLIR A325 camera has been used during WADI 1 campaign (February 2017) while FLIR A655sc camera, purchased in the frame of WADI project, was used during WADI 2 campaign (April 2017).

Figures below present the on-board installation of the cameras.



¹Camera implemented during WADI 1 campaign

²Camera implemented during WADI 2 and 3 campaigns

1.1.3.2 Ground instrumentation

The instrumentation used for ground truth measurements is listed below.

Instrumentation	Retrieved parameters	Where?
Optris portable infrared thermometer LS	Temperature	At each outdoor background characterization
GPS	Coordinates of particular elements in the areas of interest	At each flight acquisition and outdoor background characterization
Nikon camera	Pictures of the areas of interest	At each flight acquisition and outdoor background characterization
Soil moisture sensor	Soil humidity	At each outdoor background characterization
Aluminium targets (1.1 x 1.1 m ²)	IR images geo-referencing	At each flight acquisition

Table 4: List of instrumentation participating to the ground truth measurements

Figures below present part of the ground instrumentation.

		
Figure 20: Soil moisture sensor	Figure 21: IR thermometer	Figure 22: Aluminium target

1.1.4 Areas of interest

The validity and robustness of water leak detection methods is largely dependent on the feasibility of testing data processing algorithms within geographically diverse environments. The criteria for the selection of areas of interest, from a data processing point of view, are given below:

- Zone covering at least 10x10 pixels (GSD : VNIR 30cm & SWIR 60 cm @800m)
- Flat ground
- Soil moisture detection methods: bared soil, without vegetation
- Detection of indirect effects on vegetation

BUSARD airborne measurements have been conducted over three areas belonging to the water network infrastructure provided by SCP:

- Cabardèle
- Aix-en-Provence
- Valtrède

The specific geographical location of these areas, close to the BUSARD base (ONERA's headquarter in Salon de Provence), enabled ONERA to make ground truth measurements with greater ease and at a lower cost.



Figure 23: Water network infrastructure provided by SCP

1.2 Airborne measurements

In order to get useful hyperspectral and infrared data for the determination of a set of optimized detection wavelengths, three airborne field campaigns have been conducted over the water network infrastructure provided by SCP:

- WADI 1 (February 2017): overflight over uncontrolled water leakages areas
- WADI 2 (April 2017): overflight over controlled water leakages areas
- WADI 3 (July 2017): overflight over controlled water leakages areas

1.2.1 WADI 1 campaign

1.2.1.1 Uncontrolled water leakages areas

Data are acquired along an axis of rectilinear flight, at constant altitude. Each flight line is defined by three waypoints:

- 1st waypoint: locate point. Start record waypoint for IR camera (approximately 10 s before start record waypoint for hyperspectral cameras)
- 2nd waypoint: beginning of the imaged area (start record waypoint for hyperspectral cameras)
- 3rd waypoint: end record waypoint

Several sites with potential as water leakages areas have been identified and selected by SCP. They are presented below.

1.2.1.1.1 Cabardèle area

This area is located to the east of Salon-de-Provence.



Figure 24: Flight line above Cabardèle (red: gallery, yellow: flight line)

1.2.1.1.2 Aix-en-Provence area

This area is composed of the following sites: Vauvenargues, Rians (cuvette du Pigoudet), Esparron, Saint-Maximin, Le Tholonet.

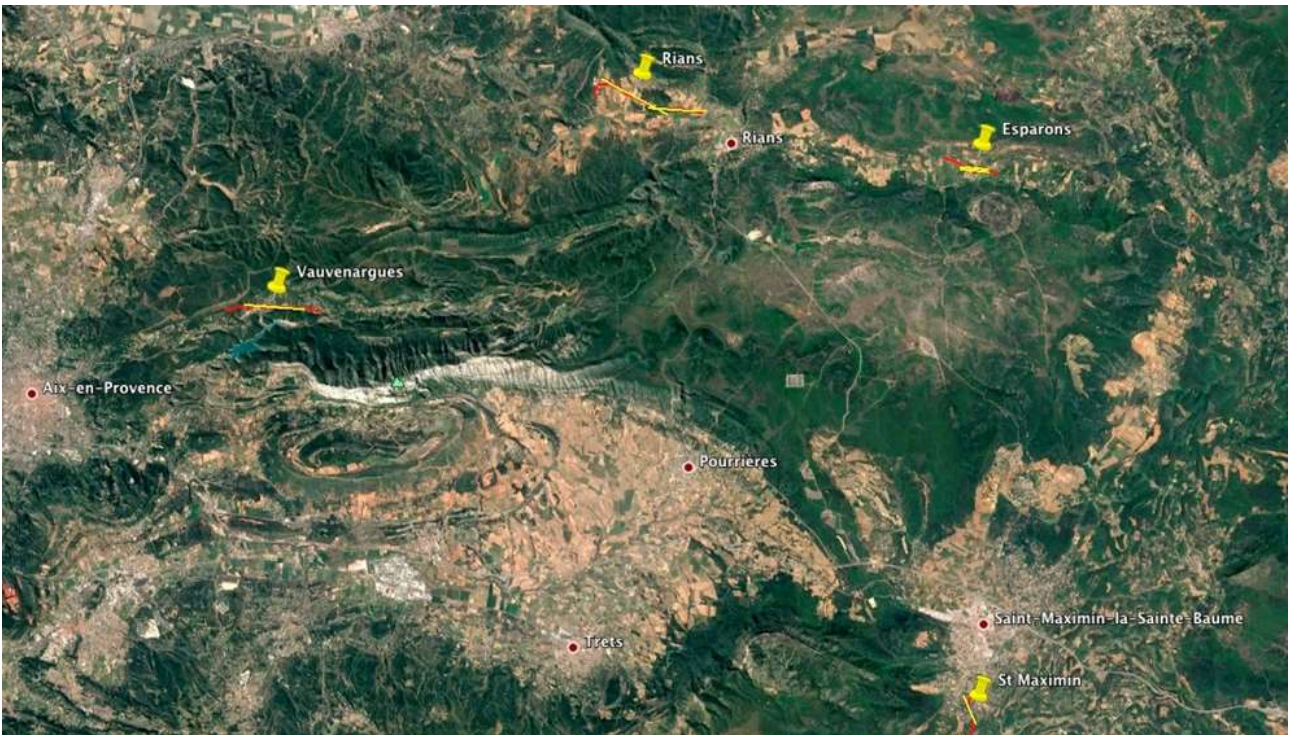


Figure 25: Overview of Aix-en-Provence area



Figure 26: Flight line above Rians (Cuvette du Pigoudet) (red: canal, yellow: flight line)

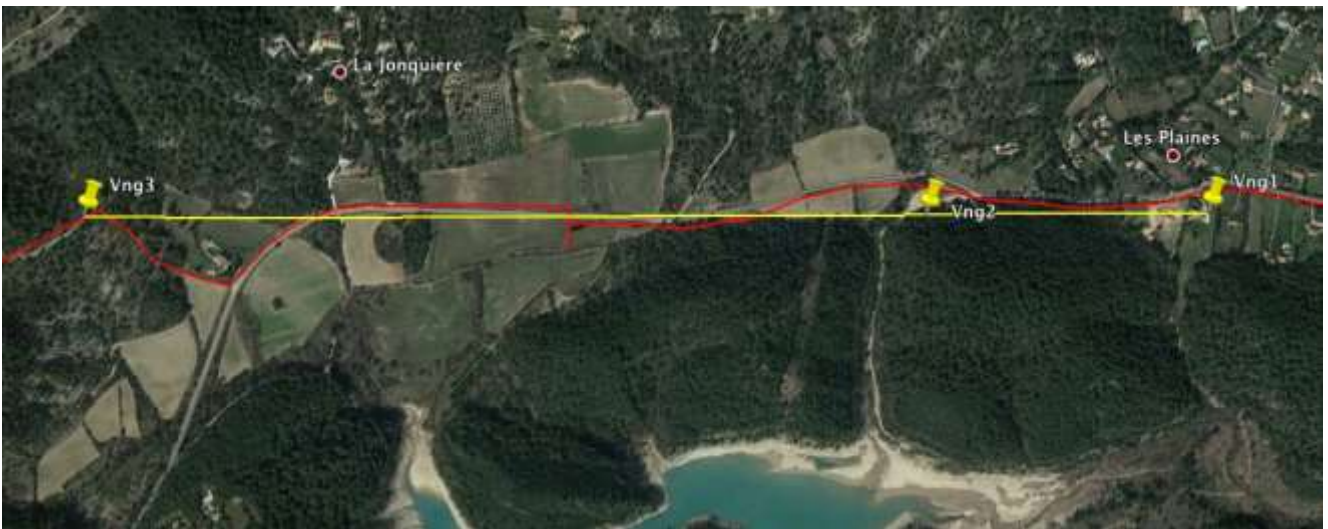


Figure 27: Flight line above Vauvenargues (red: gallery, yellow: flight line)



Figure 28: Flight line above Saint-Maximin (red: canal, yellow: flight line)



Figure 29: Flight line above Esparron (red: gallery, yellow: flight line)

1.2.1.1.3 Valtrède area

This area is composed of the following sites: Châteauneuf-les-Martigues, Saint-Julien, Saint-Pierre.



Figure 30: Overview of Valtrède area (red: gallery, yellow: flight line)



Figure 31: Flight line above Châteauneuf-les-Martigues (red: gallery, yellow: flight line)



Figure 32: Flight line above Saint-Julien (red: gallery, yellow: flight line)



Figure 33: Flight line above Saint-Pierre (red: gallery, yellow: flight line)

1.2.1.2 Flights description

A description of each flight is given in the following table.

Site	Date	Aircraft speed (m/s)	Aircraft heading (°)	Altitude above ground (m)	Flight altitude (ft)	Flight line length (m)
Cabardèle (line 1)	03/02/17	36	107	800	3022	3500
Cabardèle (line 3)	03/02/17	36	107	800	3022	2600
St Maximin	16/02/17	36	337	800	3740	1100
Rians West	16/02/17	36	299	800	3760	2600
Rians East	16/02/17	36	279	800	3760	2000
Esparron North	16/02/17	36	276	800	4000	1000
Esparron South	16/02/17	36	276	800	4000	1000
Vauvenargues	16/02/17	36	275	800	3760	2160
Châteauneuf-les-M	23/02/17	33	266	757	2500	3700
Saint-Julien	23/02/17	31.6	287	677	2500	1600



Saint-Pierre	23/02/17	30,5	279	722	2500	3200
--------------	----------	------	-----	-----	------	------

Table 5: WADI 1 campaign flights description

The objective of the first flight (Cabardèle) was to validate the global operating system and ground truth measurements methodology (functional check flight).

The following items were controlled during this flight:

- Monitoring of IMU operation (orientation, lever arm)
- Checking hyperspectral, IR and IMU data acquisition
- Confirming the correct functioning for data pre-processing chain

Table summarizes the data collected by sensors during the WADI 1 campaign flights (green: valid data). The flights were completed without incident, all the planned activities have been carried out. The cameras implementation procedure has been improved and validated.

Site	Date	IR Sequence name	IR Seq n°	IR images	Hypex Sequence name	Hypex images	Comment
Cbd North	03/02/17	wadicbd	0007		cbd170203a	01	Central line
			0008			02	North line (offset: 50m)
			0009			03	South line (offset: 50m)
0010				04		Central line	
0011				05		North line (offset: 50m)	
0012				06		South line (offset: 50m)	
CBD HC			0013			07	High freq. acquisition
St Maximin	16/02/17	wadi-aix2017 0216	0002		stm170216a	01	Improper alignment
			0003			02	Lateral offset (canal)
			0004	7 to 20		03	Ok
Rians West	16/02/17	wadi-aix2017 0216	0005	10 to 42	stm170216a	04	Defocus (IR image)
			0006	14 to 49		05	Ok
Rians East	16/02/17	wadi-aix2017 0216	0011	4 to 30	stm170216a	10	Slightly offset
			0012	4 to 35		11	Ok
Esparron North	16/02/17	wadi-aix2017 0216	0007	3 to 13	stm170216a	06	
			0008	3 to 15		07	Ok
Esparron South	16/02/17	wadi-aix2017 0216	0009	3 to 14	stm170216a	08	Ok
			0010	1 to 11		09	Delay (Hypex)
Vauvenargues	16/02/17	wadi-aix2017 0216	0013	8 to 29	stm170216a	12	Turbulences
Châteauneuf	23/02/17	wadicht0001			cht170223a_01		3 rd waypoint offset
		wadicht0002			02 et 03		Hypex shut-off; IR Ok.
		wadicht0003			cht170223a_04		Ok, vibrations
St Julien	23/02/17	wadistj0001			stj170223a_01		Ok
		wadistj0002			stj170223a_02		Ok, presence of blur
St Pierre	23/02/17	wadistp0002					
		wadistp0003			stp170223a_02		Off axis
		wadistp0004			stp170223a_03		1 st waypoint offset
		wadistp0005			stp170223a_04		Ok

Table 6: Hyperspectral and IR data collected during WADI 1 flights

1.2.2 WADI 2 campaign

1.2.2.1 Controlled water leakages areas

WADI-2 campaign was scheduled during the period between 18 and 28 April 2017. Unfortunately, bad weather did not allow us to carry more than one flight (21st of April).

1.2.2.1.1 Aix-en-Provence area

This area is composed of Le Tholonet, Vauvenargues, Rians and Saint-Maximin sites.

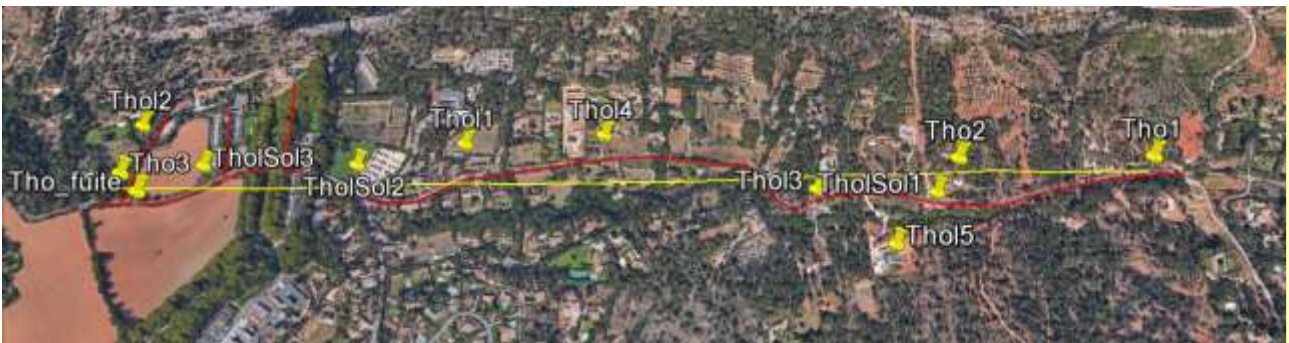


Figure 34: Flight line above Le Tholonet (red: canal, yellow: flight line, fuite: position of the leakage)

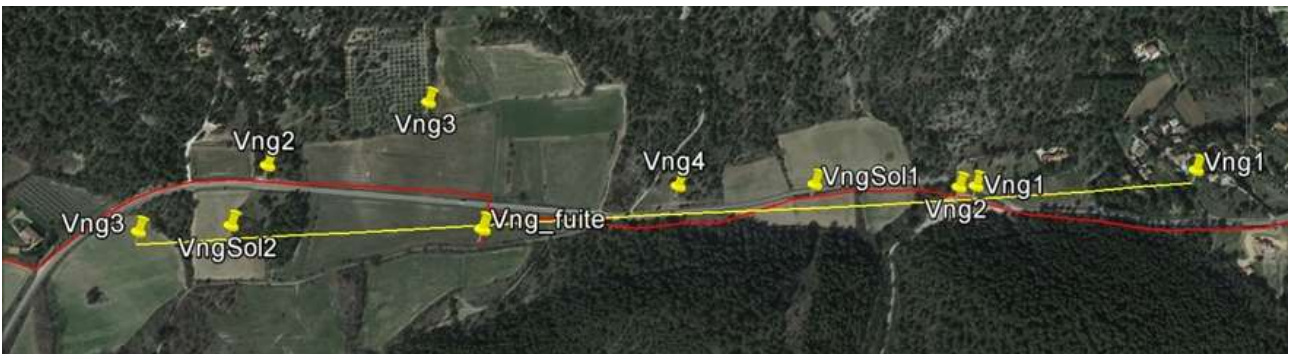


Figure 35: Flight line above Vauvenargues (red: gallery, yellow: flight line, fuite: position of the leakage)



Figure 36: Flight line above Rians (Cuvette du Pigoudet) (red: canal, yellow: flight line)



Figure 37: Flight line above Saint-Maximin (red: canal, yellow: flight line)

1.2.2.2 Flights description

A description of each flight is given in the following table.

Site	Date	Aircraft speed (m/s)	Aircraft heading (°)	Altitude above ground (m)	Flight altitude (ft)	Flight line length (m)
Le Tholonet	21/04/17	36	273	800	3225	1500
Vauvenargues	21/04/17	36	275	800	3760	2160
Rians East	21/04/17	36	279	800	3760	2000
Saint-Maximin	21/04/17	36	337	800	3740	1100

Table 7: WADI 2 campaign flights description

Table summarizes the data collected by sensors during the WADI 2 campaign flight (green: valid data). All the flights were completed without incident, the planned activities have been carried out.

Site	Date	IR Sequence name	IR Seq n°	IR images	Hypex Sequence name	Hypex images	Comment
Le Tholonet	21/04/17	wadi2_aix2017_0421	000001	3-18	aix170421	01	Img17: blurry image
			000002	4-19		02	Ok
			000011			11	1 st waypoint offset
Vauvenargues	21/04/17	wadi2_aix2017_0421	000003	5-16	aix170421	03	Significant roll
			000004	6-15		04	Roll at the end
			000010	5-15		10	Img6: blurry image
Rians East	21/04/17	wadi2_aix2017_0421	000005		aix170421	05	Leakage position missed
			000006	6-28		06	Ok
			000009	6-26		09	Not quite rectilinear
Saint-Maximin	21/04/17	wadi2_aix2017	000007	3-13	aix170421	07	Ok

		0421	000008	3-14		08	Significant roll
--	--	------	--------	------	--	----	------------------

Table 8: Hyperspectral and IR data collected during WADI 2 flight

1.2.3 WADI 3 campaign

1.2.3.1 Controlled water leakages areas

WADI-3 campaign was scheduled during the period between 07 and 13 July 2017 over Aix-en-Provence area composed of Le Tholonet, Vauvenargues, Rians like WADI-2 campaign.

- The conditions for WADI 3 campaign are described below:
- Low flowrate during 1 month
- Harvest and new crops in artificial leaks area
- Dryer conditions than for WADI 2 campaign

1.2.3.2 Flights description

A description of each flight is given in the following table.

Site	Date	Aircraft speed (m/s)	Aircraft heading (°)	Altitude above ground (m)	Flight altitude (ft)	Flight line length (m)
Le Tholonet	07/07/2017	36	273	800	3390	1500
Vauvenargues	07/07/2017	36	269	800	3763	1200
Rians East	07/07/2017	36	287	800	3763	1750
Le Tholonet	10/07/2017	36	273	800	3390	1500
Vauvenargues	10/07/2017	36	269	800	3763	1200
Rians East	10/07/2017	36	287	800	3763	1750
Le Tholonet	11/07/2017	36	273	800	3390	1500
Vauvenargues	11/07/2017	36	269	800	3763	1200
Rians East	11/07/2017	36	287	800	3763	1750
Le Tholonet	12/07/2017	36	273	800	3390	1500
Vauvenargues	12/07/2017	36	269	800	3927	1200
Rians East	12/07/2017	36	287	800	3927	1750
Esparron South	12/07/2017	36	276	800	4160	1750
Esparron North	12/07/2017	36	276	800	4160	1750

Table 9 : WADI-3 campaign flights description

Table summarizes the data collected by sensors during the WADI 3 campaign flight (green: valid data). All the flights were completed without incident; the planned activities have been carried out.

Site	Date	IR Sequence name	IR Seq n°	IR images	Hypex Sequence name	Hypex images	Comment
Rians East	07/07/2017	Wadi3_aix20170707	000001	0 - 20	riae170707a	01	
			000002	0 - 21	riae170707a	02	OK
			000003	0 - 19	riae170707a	03	
Vauvenargues	07/07/2017	Wadi3_aix20170707	000004	0 - 16	Vng170707a	01	
			000005	0 - 14	Vng170707a	02	OK
Le tholonet	07/07/2017	Wadi3_aix20170707	000006	0 - 18	Thl170707a	01	
			000007	0 - 19		02	OK
Rians East	10/07/2017	Wadi3_aix20170710	000001	0 - 20	riae170710a	01	
			000002	0 - 21		02	OK
Vauvenargues	10/07/2017	Wadi3_aix20170710	000003	0 - 16	Vng170710a	03	
			000004	-		04	
			000005	0 - 14		05	OK
Le Tholonet	10/07/2017	Wadi3_aix20170710	000006	0 - 18		06	OK
			000007	-		07	
			000008	0 - 19		08	
Rians East	11/07/2017	Wadi3_aix20170711	000001		riae170711a	01	
			000002			02	
			000003			03	
			000004			04	
			000005			05	OK
Vauvenargues	11/07/2017	Wadi3_aix20170711	000006		Vng170711a	01	
			000007			02	OK
			000008			03	
Le Tholonet	11/07/2017	Wadi3_aix20170711	000009		thl170711a	01	
			000010			02	
			000011			03	OK

Table 10 : Hyperspectral and IR data collected during WADI 3 flights

1.3 Ground truth measurements

1.3.1 WADI 1 campaign

During this campaign, passive targets (aluminium panels) have been deployed along with a soil moisture sensor in order to measure the ground truth.

1.3.1.1 Cabardèle flight

Three flight lines were done over this site, laterally offset from 50 m. The location of aluminium panels (targets) is given below. The soil moisture sensor was not used during this functional check flight.



Figure 38: Ground truth measurement areas and aluminium panels positioning for Cabardèle flight

<p>Name: GCP1 Date: 03/02/2017 Location : Cabardèle Z(MSL): 133,081 m Latitude: 43,59899144° Longitude: 5,21492286° Moisture content : no data</p> 	<p>Name: GCP2 Date: 03/02/2017 Location : Cabardèle Z(MSL): 117,316 m Latitude: 43,60224265° Longitude: 5,20132973° Moisture content : no data</p> 	<p>Name: GCP3 Date: 03/02/2017 Location : Cabardèle Z(MSL): 103,449 m Latitude: 43,60511116° Longitude: 5,1883382° Moisture content : no data</p> 
<p>Name: GCP4 Date: 03/02/2017 Location : Cabardèle Z(MSL): 102,763 m Latitude: 43,60521054° Longitude: 5,18851407° Moisture content : no data</p> 	<p>Name: GCP5 Date: 03/02/2017 Location : Cabardèle Z(MSL): 133,276 m Latitude: 43,59903446° Longitude: 5,21490857° Moisture content : no data</p> 	<p>Name: GCP6 Date: 03/02/2017 Location : Cabardèle Z(MSL): 139 m Latitude: 43,596807° Longitude: 5,221072° Moisture content : no data</p>

Table 11: Ground truth data for Cabardèle flight

1.3.1.2 Aix-en-Provence flight

The location of aluminium panels is given in the following figures. The soil moisture sensor has been used during this flight.



Figure 39: Ground truth measurement areas for Esparron flight



Figure 40: Ground truth measurement areas for Rians flight

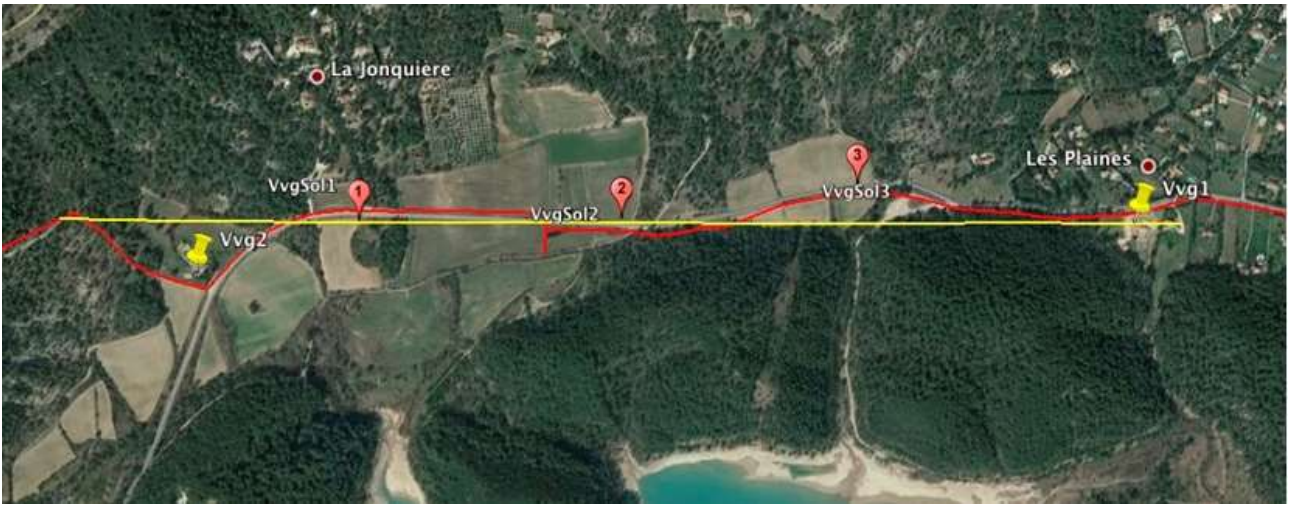


Figure 41: Ground truth measurement areas for Vauvenargues flight

<p>Name: EspSol1 Date: 16/02/2017 Location : Esparron Z(MSL): 413,644 m Latitude: 43,59672948° Longitude: 5,8699585° Moisture content : no data</p> 	<p>Name: EspSol2 Date: 16/02/2017 Location : Esparron Z(MSL): 414,682 m Latitude: 43,59673021° Longitude: 5,869763092° Moisture content : 28.1-30.7-32.8 %</p> 	<p>Name: EspSol3 Date: 16/02/2017 Location : Esparron Z(MSL): 405,484 m Latitude: 43,5974507° Longitude: 5,85656106° Moisture content : 14.2-16.6-19.2 %</p> 
<p>Name: RiaSol1 Date: 16/02/2017 Location : Rians Z(MSL): 348,398 m Latitude: 43,61773288° Longitude: 5,72560155° Moisture content : no data</p> 	<p>Name: RiaSol2 Date: 16/02/2017 Location : Rians Z(MSL): 348,022 m Latitude: 43,62575981° Longitude: 5,70439071° Moisture content : 19 to 26 %</p> 	<p>Name: RiaSol3 Date: 16/02/2017 Location : Rians Z(MSL): 349,279 m Latitude: 43,6153821° Longitude: 5,74570744° Moisture content : 8 to 29 %</p> 
<p>Name: VvgSol1 Date: 16/02/2017 Location : Vauvenargues</p>	<p>Name: VvgSol2 Date: 16/02/2017 Location : Vauvenargues</p>	<p>Name: VvgSol3 Date: 16/02/2017 Location : Vauvenargues</p>

<p>Z(MSL): 347,911 m Latitude: 43,55683671° Longitude: 5,54911269° Moisture content : 18.2 %</p> 	<p>Z(MSL): 351,894 m Latitude: 43,55648886° Longitude: 5,55539983° Moisture content : 11.6 %</p> 	<p>Z(MSL): 346,743 m Latitude: 43,55672342° Longitude: 5,56111295° Moisture content : 20.4 %</p> 
---	---	---

Table 12: Ground truth data for Aix-en-Provence flight (16-02-2017)

1.3.1.3 Valtrède flight

The location of aluminium panels is given in the following table. The soil moisture sensor has been used during this flight.

<p>Name: Cht_GCP1 Location : Châteauneuf-les-M. Latitude: 43,395887° Longitude: 5,159721° Moisture content :</p>	<p>Name: Cht_GCP2 Location : Châteauneuf-les-M. Latitude: 43,39503° Longitude: 5,149495° Moisture content : 7.9 – 6 – 4 – 4.8 – 8.8 – 6.2 %</p>	<p>Name: Cht_GCP3 Location : Châteauneuf-les-M. Latitude: 43,394775° Longitude: 5,138548° Moisture content : 16.2 – 14.8 – 11.9 – 8.6 %</p>
<p>Name: Stj_GCP2 Location : St Julien Latitude: 43,369425° Longitude: 5,085660° Moisture content</p>	<p>Name: Stj_GCP3 Location : St Julien Latitude: 43,368068° Longitude: 5,091633° Moisture content : 8.6 – 12.2 – 8.2 – 14.8 – 14.2 %</p>	
<p>Name: Stp_GCP1 Location : St Pierre Latitude: 43,372432° Longitude: 5,050649° Moisture content : 15.4 – 7 – 6 – 7.6 – 14.8 – 12.2 %</p>	<p>Name: Stp_GCP2 Location : St Pierre Moisture content : 3.2 – 8.2 – 6.9 – 9.6 %</p>	

Table 13: Ground truth data for Valtrède flight (23-02-2017)

1.3.2 WADI 2 campaign

During this campaign, passive targets (aluminium panels) have been deployed along with temperature and soil moisture sensors in order to measure the ground truth.

1.3.2.1 Aix-en-Provence flight (21-04-2017)

The location of aluminium panels is given in the following figures.

<p>Name: ThoSol1 Date: 21/04/2017 Location : Le Tholonet</p> 	<p>Name: ThoSol2 Date: 21/04/2017 Location : Le Tholonet</p> 	<p>Name: ThoSol3 Date: 21/04/2017 Location : Le Tholonet</p> 
<p>Name: VvgSol1 Date: 21/04/2017 Location : Vauvenargues</p> 	<p>Name: VvgSol2 Date: 21/04/2017 Location : Vauvenargues</p> 	
<p>Name: RiaSol1 Date: 21/04/2017 Location : Rians</p> 	<p>Name: RiaSol2 Date: 21/04/2017 Location : Rians</p> 	

Table 14: Ground truth data for Aix-en-Provence flight (21-04-2017)

The soil moisture sensor and infrared thermometer have been used during this flight. The location of the measuring points is given in the following figures.

Values of soil moisture and temperature are given in table 13.



Figure 42: Position of the measuring points for the Rians (left) and Le Tholonet (right) areas.

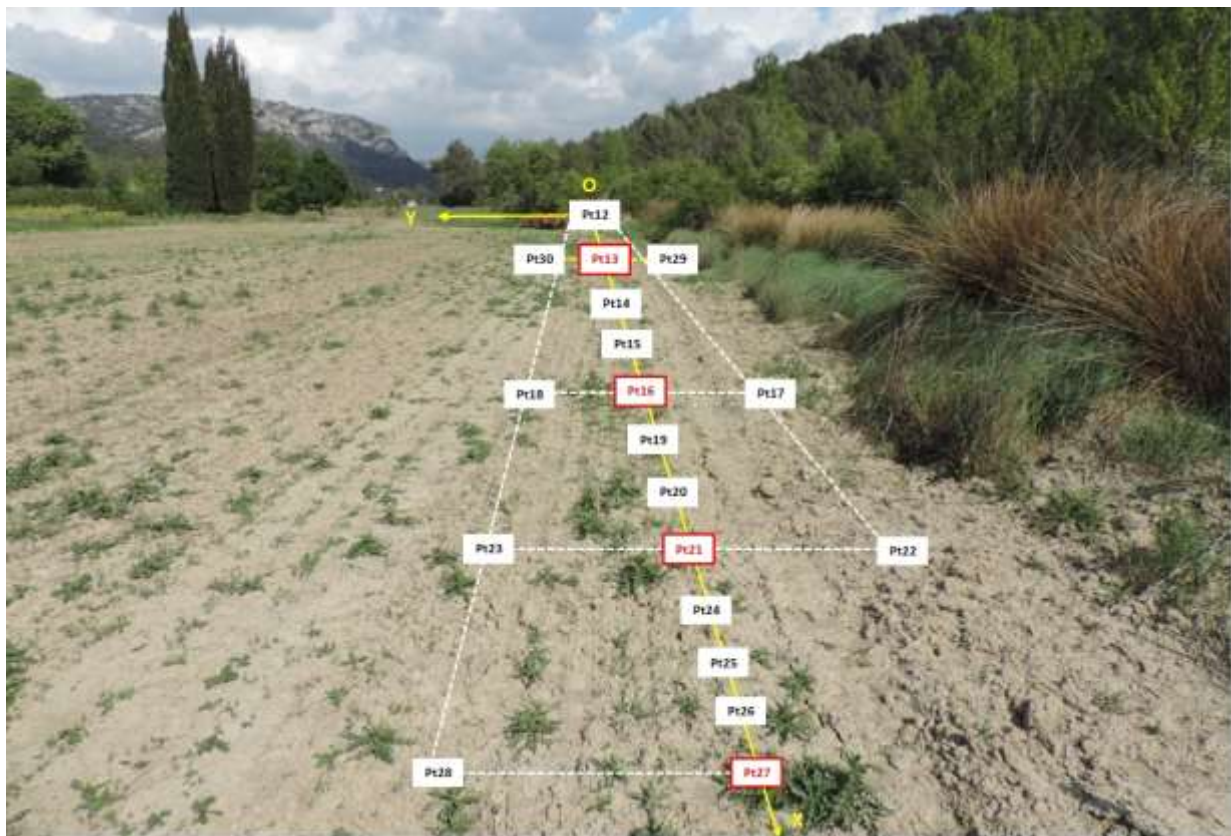


Figure 43: Position of the measuring points for the Vauvenargues area.

D3.1 Definition of optimal wavelengths and cameras



Point	Time	T (°C)	RH1 (%)	RH2 (%)	RH3 (%)	<RH> (%)	Z (MSL)	Longitude (°)	Latitude (°)	(X,Y)	Comment
Pt00	11:24	20,1	22,2	23,6	20,3	22,0	349,831	5,74565305	43,61533103	(0,0)	Rians area. In red: position of leakages Flow rate value: 80 l/hr
Pt01	11:26	17,2	32,6	40,4	40,6	37,9	348,561	5,74565864	43,61537951	(+5m,0)	
Pt02	11:29	25,6	15,3	18,5	18,4	17,4	349,821	5,74566008	43,61542263	(+10m,0)	
Pt03	11:31	27,3	9,6	6,4	12,5	9,5	349,983	5,74565857	43,61547295	(+15 m, 0)	
Pt04	11:35	23,3	-	-	-	-	349,983	5,74565857	43,61547295	(+20 m,0)	
Pt05		22,0	6,4	2,2	4,8	4,5				(+15 m, -2 m)	
Pt06		25,7	4,2	7,9		6,1				(+15 m, +2 m)	
Pt07		30,7	3,4	8,0	3,6	5,0				(+10 m,+2 m)	
Pt08		24,7	14,5	6,8		10,7				(+10 m,-2 m)	
Pt09		16,5	27,4	29,5	29,4	28,8				(+5 m,-1 m)	
Pt10		22,4	11,7	10,1	11,3	11,0				(+5 m,+1 m)	
Pt11		23,4	13,0	12,6	9,0	11,5				(0,+1 m)	
Pt12	14:00	31,0	4,5	8,0	8,0	6,8	346,930	5,55341407	43,55601495	(0,0)	Vauvenargues area. In red: position of leakages. Flow rate value: 300 l/hr
Pt13	14:08	22,7	38,4	40,8	42,6	40,6	346,844	5,55328407	43,55602387	(+5 m, 0)	
Pt14	14:16	36,8	17,0	20,0	22,3	19,8	346,405	5,55322527	43,55602877	(+10 m, 0)	
Pt15	14:12	30,2	11,0	11,0	13,6	11,9	346,478	5,55318718	43,55602907	(+15 m, 0)	
Pt16	14:20	17,3	46,4	47,6	43,2	45,7	346,243	5,55315449	43,55602882	(+20.5 m, 0)	
Pt17		22,6	31,0	29,8	32,6	31,1				(+20.5 m, -1 m)	
Pt18		25,3	14,3	12,8	15,9	14,3				(+20.5 m, +1 m)	
Pt19	14:40	26,0	23,6	19,8	22,6	22,0	346,054	5,55310430	43,55602597	(+25 m, 0)	
Pt20	14:43	27,4	12,7	13,0	14,6	13,4	346,043	5,55304095	43,55603118	(+30 m, 0)	
Pt21	14:45	26,4	10,2	12,0	12,8	11,7	346,029	5,55298268	43,55603374	(+35 m, 0)	
Pt22		23,6	5,3	9,2	7,2	7,2				(+35 m, -1 m)	
Pt23		27,7	16,6	15,0	25,0	18,9				(+35 m, +1 m)	
Pt24	14:52	30,7	23,7	23,2	21,4	22,8	345,588	5,55291788	43,55604041	(+40 m, 0)	
Pt25	14:57	34,1	24,8	29,6	28,6	27,7	345,552	5,55285596	43,55604551	(+45 m, 0)	
Pt26	14:59	31,2	14,4	15,0	15,8	15,1	345,641	5,55279703	43,55605069	(+50 m, 0)	
Pt27	15:01	27,7	21,2	21,8	21,8	21,6	345,528	5,55276273	43,55605528	(+52.5 m, 0)	
Pt28		29,7	22,1	20,9	21,6	21,5				(+52.5 m, +1 m)	
Pt29		28,4	21,1	20,4	21,6	21,0				(+5 m, -1 m)	
Pt30		29,2	10,2	13,6	15,0	12,9				(+5 m, +1 m)	
Pt31	15:54	35,2	7,0	3,9	7,6	6,2	182,378	5,50619825	43,52204561	(0,+1 m)	Le Tholonet area. Leakage is located at (+5 m, 0) position Flow rate value: 180 l/hr
Pt32	15:58	31,2	30,4	29,0	29,4	29,6	182,422	5,50619767	43,52202702	(+2 m, 0)	
Pt33	16:00	21,2	45,8	48,6	48,0	47,5	181,334	5,50618729	43,52201175	(+4 m, 0)	
Pt34	16:02	18,7	45,4	45,6	45,0	45,3	180,900	5,50618923	43,52199454	(+6 m, 0)	
Pt35	16:04	15,7	32,8	33,0	35,8	33,9	181,692	5,50618884	43,52197131	(+8 m, 0)	
Pt36	16:09	34,3	7,2	7,8	7,5	7,5	182,181	5,50637301	43,52203613	(0,0)	Le Tholonet: control area (no leakage)
Pt37	16:12	27,2	9,4	9,3	10,4	9,7	181,926	5,50637046	43,52201275	(+4 m, 0)	
Pt38	16:15	27,6	13,6	21,6	19,2	18,1	182,142	5,50637073	43,52200217	(+6 m, 0)	

Table 15: Temperature (T) and soil moisture (RH) values measured on the different sites.



Figure 44: Vauvenargues area: pictures of the soil on the site of controlled leakages (flow rate: 300 l/h).



Figure 45: Vauvenargues area: pictures of the soil on the site of controlled leakages (flow rate: 720 l/h).

1.3.3 Acoustic and ground investigation on Esparron site

During the flights of February over Esparron site, high moisture areas were detected with WADI methods.

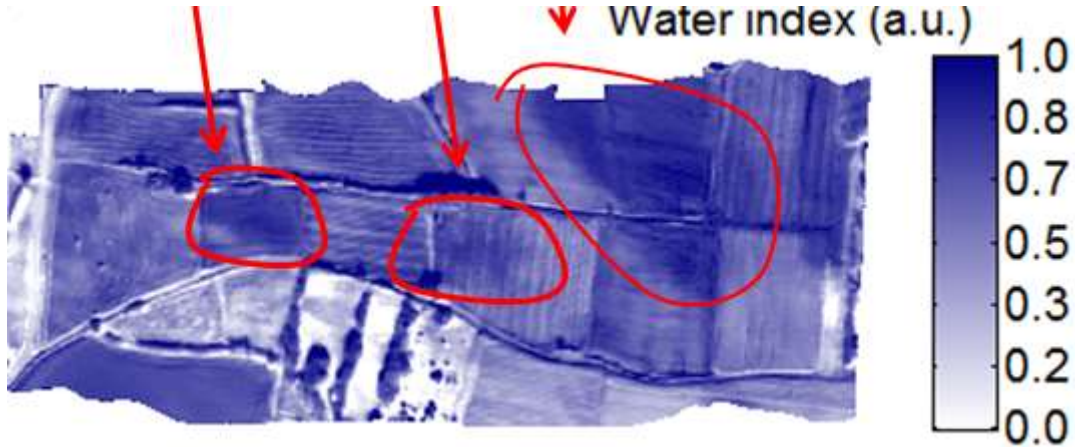


Figure 46 : Result of data processing on Esparron site

SCP and ONERA decided to use an acoustic method out this place and to dig to confirm the presence of water leaks.

It was done the 12th of June on the area between the WADi-2 & WADi-3 campaigns.

First, SCP used microphone on hydrants and accessible parts of the pipe (man holes).



Figure 47 : microphone used for leak detection

With this first investigation method, SCP has not detected any strong signal but only a suspicion of leak not far from the hydrant 02020. On the ground, puddles were found not

far from the drain valve and between the drain valve and the connecting manhole that was completely drowned.



Figure 48 : Puddle not far from the drain valve



Figure 49 : Puddle between the drain valve and the connecting manhole, and drowned manhole

In order to identify the origin of water, SCP used the acoustic correlation method between the aerial points connected with the pipe.



Figure 50 : devices for acoustic correlation method

The analysis of the signal was not conclusive and this method has not identified any water leak in the pipe.

Finally, we choose to dig and put the microphone directly on the pipe in three points:

- Around the drain valve,
- Around the puddle,
- In the upper part of the wet area shown by WADI humidity maps.



Figure 51 : digging works and microphone located directly on the pipe

It confirmed that there was no leak on the pipe.

In conclusion, those complementary ground investigations:

- Have confirmed the presence of the high moisture areas detected by WADI tools even if all its localization are not completely concordant (high moisture 1m deep around the hydrant 02020 not detected by WADI method, and low moisture at the depth of 1 meter at the upper part of the wet area shown by WADI water index maps)
- Have rebutted the hypothesis of water leak. The origin of water is probably natural even if the surface vegetation does not seem typical of wet areas.

This raises awareness on the importance of the analysis of the WADI context to minimize false interpretation of water leak detection results.

1.3.4 WADI 3 campaign

During this campaign, passive targets (aluminium panels) have been deployed along with temperature and soil moisture sensors in order to measure the ground truth.

1.3.4.1 Aix-en-Provence flight (07-07-2017)

The location of aluminium panels is given in the following figures.

<p>Name: ThoSol1 Date: 07/07/2017 Location : Le Tholonet</p> 	<p>Name: ThoSol2 Date: 07/07/2017 Location : Le Tholonet</p> 	<p>Name: ThoSol3 Date: 07/07/2017 Location : Le Tholonet</p> 
<p>Name: VvgSol1 Date: 07/07/2017 Location : Vauvenargues</p> 	<p>Name: VvgSol2 Date: 07/07/2017 Location : Vauvenargues</p> 	
<p>Name: RiaSol1 Date: 07/07/2017 Location : Rians</p> 	<p>Name: RiaSol2 Date: 07/07/2017 Location : Rians</p> 	<p>Name: RiaSol3 Date: 07/07/2017 Location : Rians</p> 

Table 16: Ground truth data for Aix-en-Provence flight (07-07-2017)

The soil moisture sensor and infrared thermometer were not used during this flight.

1.3.4.2 Aix-en-Provence flight (10-07-2017)

The location of aluminium panels are the same that those of the 2017/07/07 (Table 16).

The soil moisture sensor and infrared thermometer were used during this flight. Values of soil moisture and temperature are given in table 17 (the location of the measuring points is given on figures 43 and 44).

Point	Time	T (°C)	RH1 (%)	RH2 (%)	RH3 (%)	<RH> (%)	Z (MSL)	Longitude (°)	Latitude (°)	(X,Y)	Comment
Pt01	11h30	28,6	41,0	39,0	35,0	38,3	348,561	5,74565864	43,61537951	(+5m,0)	Rians area.
Pt04		43,0	7,3	5,0	2,2	4,8	349,983	5,74565857	43,61547295	(+20 m,0)	Flow rate value: 260
Pt13	14h15	40,1	1,4	8,0	1,2	3,5	346,844	5,55328407	43,55602387	(+5 m, 0)	Vauvenargues area.
Pt16		30,3	7,0	42,0	2,0	17,0	346,243	5,55315449	43,55602882	(+20.5 m, 0)	In red: position of leakages.
Pt21		33,6	3,3	11,2	3,4	6,0	346,029	5,55298268	43,55603374	(+35 m, 0)	Flow rate value: 240
Pt27		37,9	8,2	7,4	4,6	6,7	345,528	5,55276273	43,55605528	(+52.5 m, 0)	Flow rate value: 240
Pt32	15h15	55,6	1,5			1,5	182,422	5,50619767	43,52202702	(+2 m, 0)	Le Tholonet area.
Pt33		31,2	45,0			45,0	181,334	5,50618729	43,52201175	(+4 m, 0)	Leakage is located at
Pt34		29,4	41,5			41,5	180,900	5,50618923	43,52199454	(+6 m, 0)	(+5 m, 0) position
Pt35		40,0	0,0			0,0	181,692	5,50618884	43,52197131	(+8 m, 0)	Flow rate value: 300

Table 17 : Temperature (T) and soil moisture (RH) values measured on the different sites (10/07/2017).

1.3.4.3 Aix-en-Provence flight (11-07-2017)

The location of aluminium panels are the same that those of the 2017/07/07 (Table 16).

The soil moisture sensor and infrared thermometer have been used during this flight. Values of soil moisture and temperature are given in table 18 (the location of the measuring points is given on figures 43 and 44).

Point	Time	T (°C)	RH1 (%)	RH2 (%)	RH3 (%)	<RH> (%)	Z (MSL)	Longitude (°)	Latitude (°)	(X,Y)	Comment
Pt01	11h30	31,3	41,0	39,0	35,0	38,3	348,561	5,74565864	43,61537951	(+5m,0)	Rians area.
PT02		40,0		13,4		13,4				10,0	Flow rate value: 180 l/hr
PT04		41,5		3,6		3,6	349,983	5,74565857	43,61547295	20,0 m	
Pt13	13h35	33,0					346,844	5,55328407	43,55602387	(+5 m, 0)	Vauvenargues area.
Pt16		31,0	34,6	47,2	36,1	39,3	346,243	5,55315449	43,55602882	(+20.5 m, 0)	In red: position of leakages.
Pt21		34,3	1,5	10,4	4,8	5,6	346,029	5,55298268	43,55603374	(+35 m, 0)	Flow rate value: 300 l/hr
Pt27		31,8	2,7	10,4	13,3	8,8	345,528	5,55276273	43,55605528	(+52.5 m, 0)	Flow rate value: 300 l/hr
Pt32	15h15	42,0	18,3			18,3	182,422	5,50619767	43,52202702	(+2 m, 0)	Le Tholonet area.
Pt33		30,4	44,8			44,8	181,334	5,50618729	43,52201175	(+4 m, 0)	Leakage is located at
Pt34		29,4	42,0			42,0	180,900	5,50618923	43,52199454	(+6 m, 0)	(+5 m, 0) position

Table 18 : Temperature (T) and soil moisture (RH) values measured on the different sites (11/07/2017).

1.3.4.4 Aix-en-Provence flight (12-07-2017)

The location of aluminium panels are the same that those of the 2017/07/07 (Table 16).

The soil moisture sensor and infrared thermometer have not been used during this flight.

1.4 Conclusion

Between February and July 2017, airborne measurements were conducted over several areas belonging to the water network infrastructure provided by SCP with ONERA's aerial platform BUSARD instrumented with two hyperspectral cameras and one uncooled infrared camera.

Apart from the weather which reduced flight opportunities, all the planned activities have been carried out, the flight axis have been completed without incident and the hyperspectral and IR data have been pre-processed (geometrics and radiometric correction, registration).

D3.1 Definition of optimal wavelengths and cameras



These trials have led to the development of hyperspectral (VNIR and SWIR spectral domains) and TIR panchromatic images database from which the relevant physical parameters (soil temperature, spectral reflectance...) will be extracted (subtask 3.1.2). These results will be used as a basis to determine the optimized detection wavelengths for the future WADI prototype.



2 Trials assessment, optimized detection wavelengths determination and measurement strategy

2.1 Introduction

The three parties of the BUSARD campaign (WADI-1, WADI-2 & WADI-3) carried out during Task 3.1 represent the WADI images database which contains the physical parameters (reflectance and temperature) necessary for the determination of optimized wavelengths for leakage detection. Before the exploitation of these physical parameters, all the trials need to be assessed. This operation, called the pre-processing, is included in the complex hyper-spectral and IR data processing. The next step consists in using the physical parameters extracted from the ortho-images database to generate the humidity maps. In the end, a set of optimized detection wavelengths is determined as a function of the corresponding trials (soil and vegetation) and a measurement strategy is designed. This strategy provides guidance for the physical effect observation.

2.2 Pre-processing of airborne optical remote sensing

This section of the document presents the pre-processing of hyperspectral & IR data recorded with the Hypspx (VNIR & SWIR) and FLIR IR cameras. It describes how to take into account the velocity, positions and attitudes of the aircraft for the ortho-rectification process of each image.

2.2.1 Hyperspectral data pre processing

Hyperspectral cameras imaging principle is a scanning mode usually called "pushbroom". It consists in acquiring the images line by line by taking advantage of the motion of the plane over the scene of interest. However the flight of the aircraft is not regular, neither in altitude, nor in velocity, nor in attitude with effects such as roll, pitch and yaw. Consequently it raised the problem to place pixels at the exact position they should appear on the map, making what we call further an ortho-image which is compatible with a use in geographical system information (GIS). This stage from raw image to ortho-image is a complex process called ortho-rectification which implies a projection into a system of standard geographical coordinates. During this process we need to take into account the topography and line of sight of the cameras using DEM (Digital Elevation Model), geographic reference images to find GCP (Ground Control Point) and IMU (Inertial Motion Unit) data. All these different operations (orthorectification, georeferencing and projection) are linked and will be called ortho-rectification.

The figure below shows the various data used in the process of orthorectification of the hyperspectral data pre-processing:

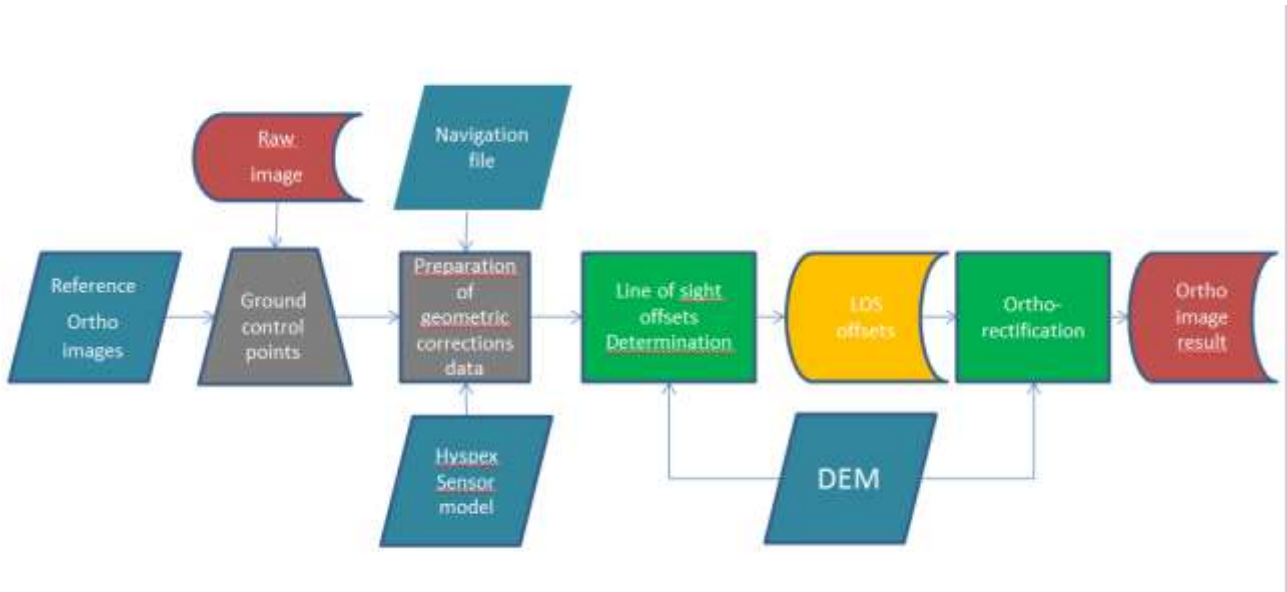


Figure 52 : Hyperspectral data pre- processing chain

2.2.1.1 GPS and IMU data

A necessary component for airborne hyperspectral data collection is a GPS and Inertial Motion Unit (IMU). The IMU used during the Busard campaign is the IMAR itrace F-200 which is equipped of a directional gyroscope hybridized with a global positioning system (GPS). This essential component provides not only file of navigation with GPS information at the location of each captured line frame but it also provides the orientation of the aircraft with regard to roll, pitch, and yaw axes.

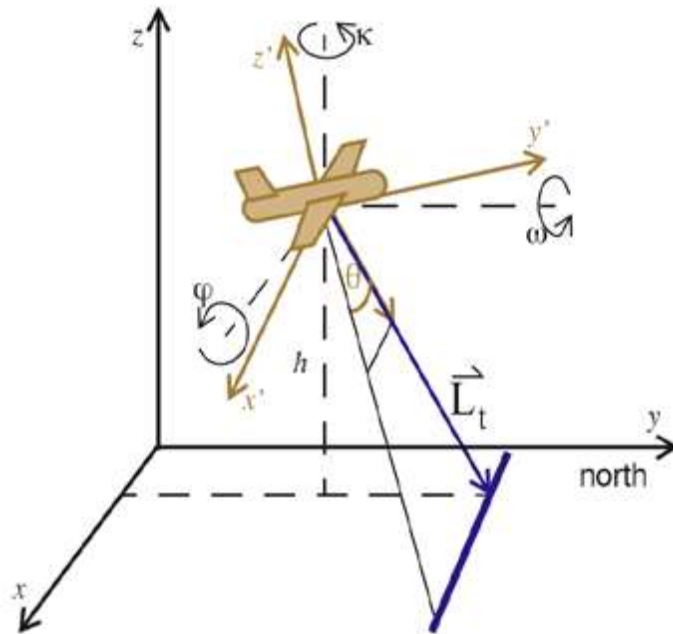


Figure 53 :Aircraft Orientation

2.2.1.2 Reference data and Digital Elevation Models (DEMs)

As public research institution we have access to the ortho images of reference from database BDORTHO of IGN (French National Geographical Institute) at the sampling rate of 50 cm throughout France. The six-axis attitude information (GPS, gyroscope) can be used along with digital elevation models (DEMs) to orthorectify the hyperspectral image data set. The DEM used in the Hypsrex chain for the Busard campaign comes from the RGE ALTI@5m database provided for each part of the French territory. The sampling rate of 5 m is sufficient for the areas with low variability of relief.

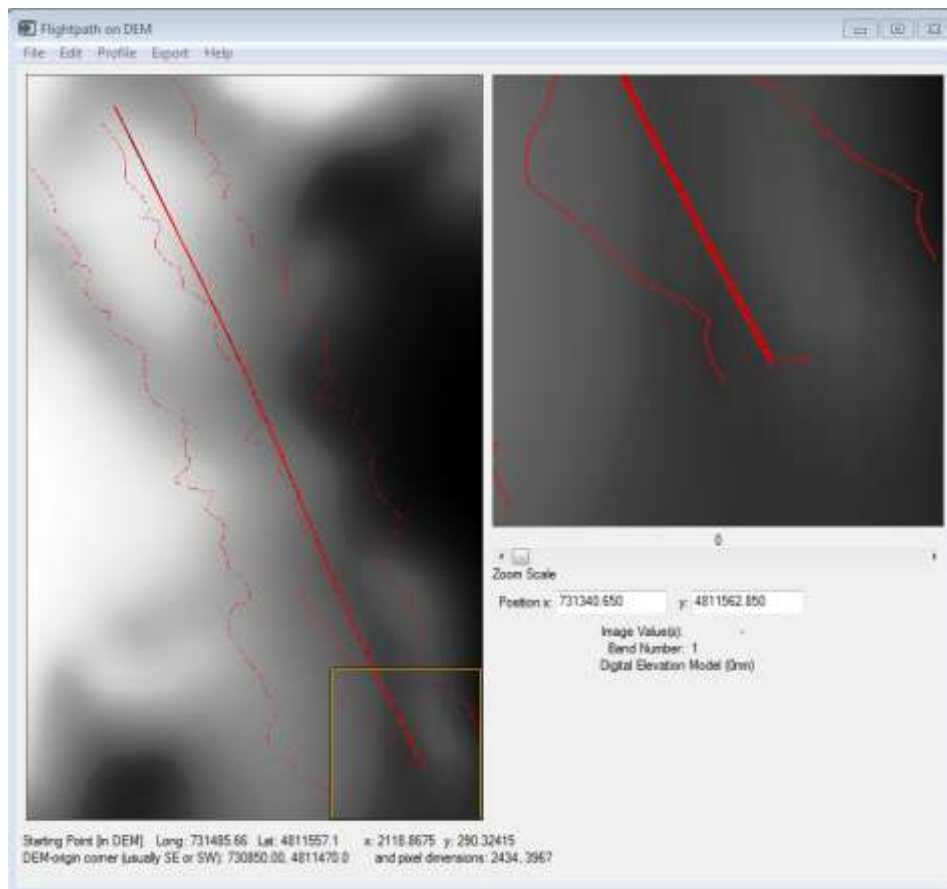


Figure 54 aircraft attitude information on DEM

2.2.1.3 Offsets for the line of sight

There is an offset between the line of sight and the axis of the inertial unit due to mechanical assembly which cannot allow a constant and reproducible alignment of the position of the sensors and the inertial unit. The assessment principle of these offsets is based on the comparison between points of known coordinates (Ground Control Points) from ortho images of reference and the position of these points projected on the DEM from the airborne image and their parameters of positions (x, y, z, roll, pitch and yaw).

2.2.1.4 Example of pre-processed hyperspectral images

Figure 55 gives the location of one infrastructure of SCP named “Pigoudet” the result of the pre-processing for hyperspectral images acquired during the 1st part of the Busard campaign (WADI-1, February) over one SCP site (Rians).

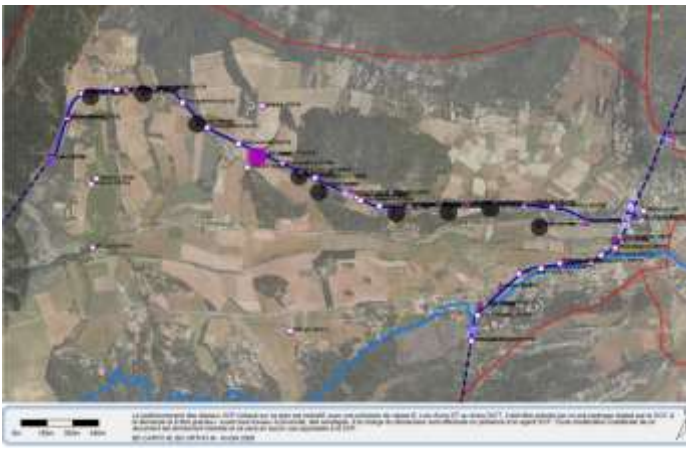
	
<p>Pigoudet open channel with localization</p>	<p>Rians site near Aix-en Provence</p>
	
<p>RGB image of SWIR camera</p>	<p>RGB image of VNIR camera</p>

Figure 55 VNIR & SWIR image over Rians site

2.2.2 IR pre-data processing

2.2.2.1 IMU data

The pre data processing for IR images involves, like hyperspectral images, knowledge for every image of its GPS position and the orientation of the camera. But there is only one inertial unit on the BUSARD platform which is located inside the left pod of the motorglider and associated to the hyperspectral payload:

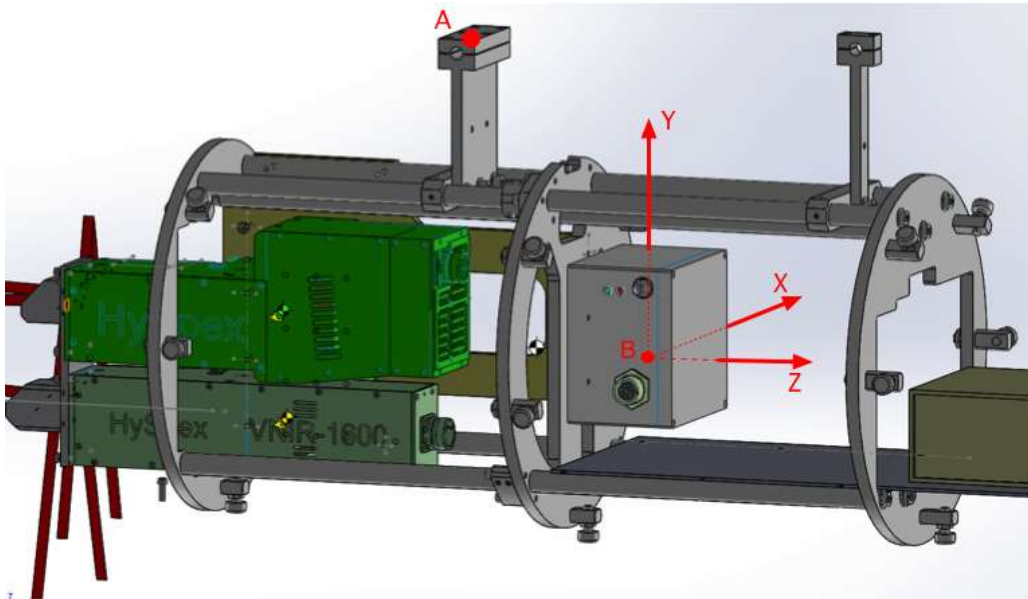


Figure 56 : IMU location in the left pod of BUSARD

In the absence of one inertial unit dedicated to the IR camera in the right pod, lever arms are calculated for the IR payload and converted in the axis of the IMU which allows the ortho-rectification of the IR images:



Aircraft axis

IMU axis

Figure 57 : Aircraft and IMU axis

Orthorectification process requires an overlap of 60% between each image, leading approximately to 0,5 Hz frame rate while IMU data are acquired at 200Hz.

A ground post processing tool developed at ONERA allows the automatic extraction of position and orientation of each image from the IMU data, in a text file.

Then, Onera uses CORELATOR 3D software from Simactive, to generate infrared ortho-images and ortho-mosaic results. The software needs the position and orientation of each image and the position of ground points control. Infrared mosaics are saved as GEOTIFF format.

2.2.2.2 Example of pre-processed IR images

The figure below shows the results of the pre-processing for TIR images acquired during the 1st part of the Busard campaign (WADI-1, February) over four SCP sites (Le tholonet, Vauvenargues, Rians, St Maximin).

The checks carried with Google Earth show a good agreement between georeferenced infrared mosaic and Google Earth:

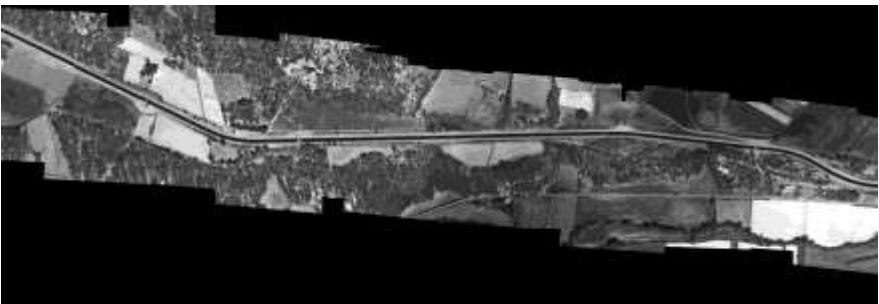
	
<p>IR ortho-mosaic from Le Tholonet</p>	<p>IR ortho-mosaic from Vauvenargues</p>
<p>from</p> 	
<p>IR ortho-mosaic from Rians</p>	<p>IR ortho-mosaic from St Maximin</p>

Figure 58 : IR ortho-mosaic

2.2.3 Registration of pre-processed images data

2.2.3.1 IDL and GEFOLKI tools

The implementation of image processing algorithms requires to work on registered images. In our case of heterogeneous remote sensing images (VNIR, SWIR, TIR), this stage of coregistration will be done with the module GEFOLKI developed in Matlab language (GeFolki software, Brigot, 2016). This tool requires a preliminary step which consists in re-sampling images in such a way that each image has the same pixel size projected on the ground and the same number of pixels.

The method used consists initially in sub-sampling by a factor of two the VNIR image corresponding to the SWIR image which has the lower spatial resolution.

Secondly, a simple graphical user interface (GUI) enables to visualize the images from the three channels (VNIR, SWIR, TIR) and to select the common amer point. The contrast/brightness adjustments are optimized for each displayed image.

Then, an algorithm automatically determines the common zone of the three images, based on the position of the amer point in the image and the dimension of the image. The three images are saved in BSQ format (Band SeQuential) compatible with the modules of the data processing chain.

The preliminary module developed in IDL language offers the following capabilities:

- Importation of multispectral images (VNIR,SWIR) in BSQ format
- Importation of IR mosaic in GEOTIFF format
- Image Display / manual selection of common amer point to the three images
- Re-sampling, calculation of the common area to the three images and recording of the three images in BSQ format with the same size (width, length) and the same pixel size.

An example of the result is shown on two VNIR and SWIR images acquired over the East Rians zone.

Figure 59 presents the superposition of 2 raw images (with VNIR image re-sampled).

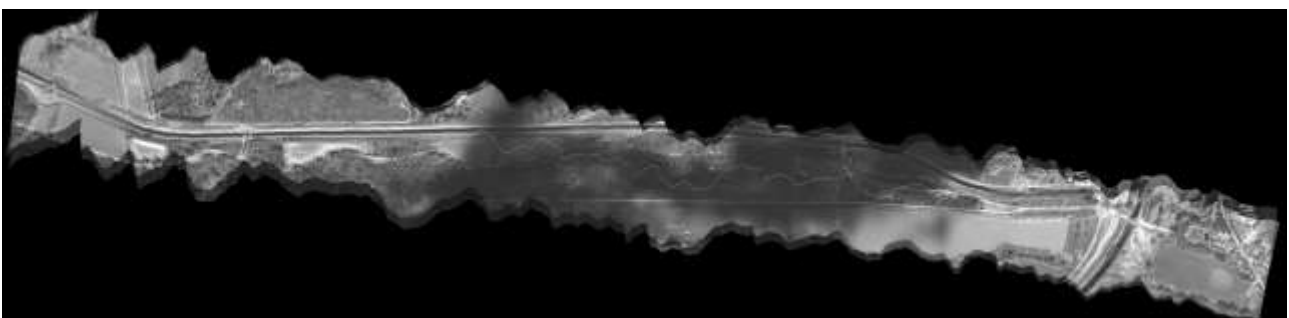


Figure 59 : Raw VNIR + 50 % SWIR images

Figure 60 presents the overlapping of the two aligned images resulting from the IDL tool.

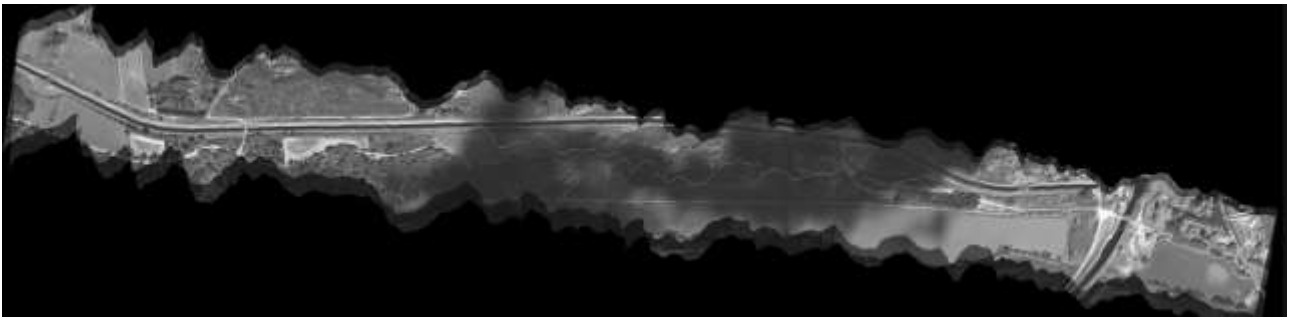


Figure 60 : pre-aligned VNIR + 50 % SWIR images

Furthermore, IR images (not represented here to avoid overloading the figures) overlap perfectly with the VNIR & SWIR images.

2.3 Data processing for getting information on the water presence in soil or in vegetation

2.3.1 Principle of the “trapezoid” method with different variants

Vegetation and soil temperatures have long been recognized as an indicator of water availability. As a matter of fact, under proper water supply, the transpiration cools the leaves towards air temperature. Water is exchanged through the stomata, i.e. the pores in the leaf epidermis. On the opposite, under water stress condition, the plant closes its stomata to limit transpiration. This leads to foliage temperature increase. Similarly, the soil surface temperature is inversely correlated with water content due to evaporation. Additionally, soil drying induces a reduction of soil thermal inertia which also leads to soil temperature increase. Hence, the temperature as remotely measured by an infrared camera should provide a powerful indicator of the moisture content of the soil.

However a series of difficulties appear for the following two reasons. The first one is that the infrared response of the vegetation is not the same as the response of the bare soil, because of a difference in temperature (due to different thermal transfer processes and different boundary conditions) but also in infrared emissivity. The second reason is a consequence of the previous one and of the fact that most pixels are generally a mixture of vegetation and soil; hence the radiance reaching the elementary detector is thus a combination of the radiance coming from leaves and from soil. As a consequence, the brightness temperature depends on temperature and emissivity of both soil and vegetation and also on the vegetation cover fraction. For this reason, the problem of evaluating the soil moisture is underdetermined when only considering the brightness temperature: a same brightness temperature value can be associated with a large range of soil moisture. It is thus necessary to add other observation data to reduce this under-determination and finally produce a more faithful indicator of the soil moisture.

A method proposed a few years ago consists in jointly analysing the temperature and a vegetation index which is used as a proxy of the vegetation cover. Such index could be

the classical NDVI (Normalized Difference Vegetation Index) which corresponds to the normalized difference between the spectral reflectances in the red and in the near infrared (typically at about 0.65 μm and 0.8 μm , i.e. on each part of the red edge induced by the chlorophyll differential spectral behaviour; this red edge extends from about 0.675 and about 0.765-0.8).

$$\text{NDVI} = \frac{\rho_{\text{NIR}} - \rho_{\text{RED}}}{\rho_{\text{NIR}} + \rho_{\text{RED}}}$$

This index is strongly correlated with the vegetation cover: it ranges from about 0.1 for bare soil to values close to 0.8 for dense and green vegetation, depending on the wavelength choice. It is also correlated with foliage density which is expressed by LAI, Leaf Area Index (total surface of leaves per unit surface). However NDVI is also sensitive to the soil spectral characteristics. Other indexes were proposed for being less dependent on soil background). Among them we considered OSAVI (Optimized Soil Adjusted Vegetation Index) (Rondeaux et al., 1996).

$$\text{OSAVI} = \frac{\rho_{0.86} - \rho_{0.66}}{\rho_{0.86} + \rho_{0.66} + 0.16}$$

When plotting the two-dimensional distribution of temperature and vegetation index (T-VI) corresponding to an area with well distributed vegetation cover and moisture content, one gets a scatter of triangular or trapezoidal shape (see figure 1). The four vertices correspond to the extreme conditions of a crop (Moran 1994): the bottom vertices (low VI) correspond to dry and saturated bare soil, whereas the upper vertices (high VI) correspond to well-irrigated and water stressed full cover vegetation. The left limit is called the "wet" edge (or "cold" edge) whereas the right limit is called the "dry" edge (or "warm" edge).

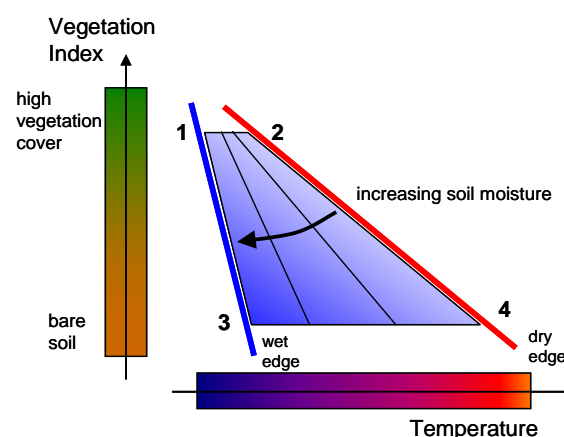


Figure 61 : Principle of soil moisture mapping from a Temperature-Vegetation Index (T-VI) plot (Moran 1994, Sandholt 2002, Krpez, 2005, 2009, 2012).

The vertices of the trapezoidal distribution correspond to: 1 : well-watered full cover, 2 : non-transpiring full cover, 3 : wet bare soil, 4 : dry bare soil. Soil moisture increases from the dry edge (on the right) to the wet edge (on the left).

There are several methods for calibrating the trapezoidal scatterplot, i.e. for assigning a water content value to each point between these four vertices (see the review in Krapez 2009).

The method of Moran 1994 is based on the use of the Penman-Monteith equation for evapotranspiration. It allows expressing the difference between surface temperature and air temperature for the limiting cases corresponding to the four vertices of the trapezoidal T-VI plot (see fig. 1). It is admitted that the soil dryness linearly increases when moving from the wet edge to the dry edge (Moran 1994, Sandholt, 2002). For this reason, a soil moisture index (the Water Availability Index - WAI) can be defined from the relative distance, at constant VI, of a given point to the dry edge (Krapez 2009) : $WAI = 1 - WDI$, where WDI is the Water Deficit Index defined in (Moran 1994). Similarly, it is argued that the vegetation stress increases from the wet edge to the dry edge. A consequence is that the position of a given point relatively to these border lines could also be a measure of the evapotranspiration flux at the time of the remote sensing test. Iso-moisture straight lines are then distributed linearly between the wet edge and the dry edge. Based on a statistical approach for the evaluation of the trapezoid vertices position, plots of the mean WAI values in the T-NDVI space and of the corresponding standard error were built in (Krapez 2009) (see fig. 2). The right plot shows in particular that the precision in evaluating the Water Availability Index worsens for rising NDVI, i.e. high vegetation cover fraction. Sensitivity of thermal remote sensing to soil moisture thus decreases in presence of dense vegetation.

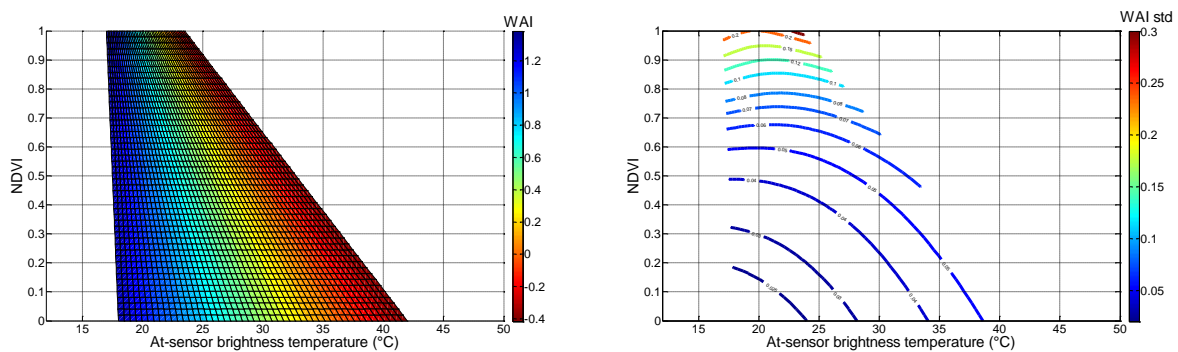


Figure 62 : Left : Colormap of mean Water Availability Index (WAI) in the T-NDVI space. Right : Isolevel curves describing the WAI standard error in the T-NDVI space (from Krapez 2009).

The method of Carlson 1995, 2005, is based on the use of a SVAT model (Soil Vegetation Atmosphere Transfer). This model allows evaluating the radiation flux, the convective flux and the water/vapor fluxes between soil, vegetation and atmosphere. For a given soil moisture content, it thus enables to calculate the brightness temperature averaged over soil and vegetation for the time of the acquisition. Iso-moisture lines, which are not necessarily straight lines, can then be drawn. These isopleths can be interpolated with a bivariate polynomial to get a practical inversion tool. Additional simulations were performed by Krapez 2009, with SETHyS model by assuming different values for the root

zone mean water content (see fig. 3). The results highlighted the fact that the temperature sensitivity to the upper soil layer moisture is most important at low NDVI (i.e. low vegetation cover fraction) whereas at high NDVI temperature is essentially sensitive to root zone moisture.

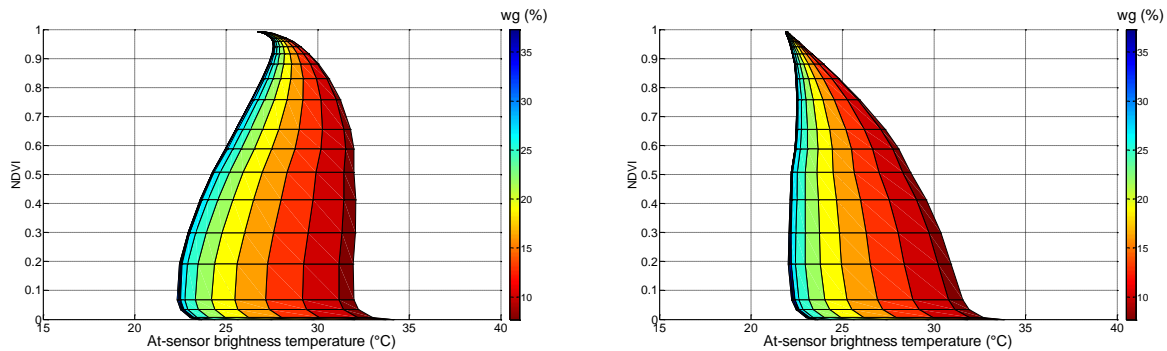


Figure 63 : Temperature versus NDVI and upper soil layer water content (wg %vol.). Root zone mean water content was considered constant for each plot: 10% vol. (left) and 20% vol. (right). (from Krapez 2009)

The methods presented so far rely on a preliminary calculation of the iso-moisture lines, let them be straight lines, like in the Moran method, or curved lines, like in the Carlson method. The temperature calculation requires a substantial number of parameters, particularly when using a SVAT model (meteorological data, soil and vegetation properties...). In addition, due to the estimation error of most parameters, the T-NDVI experimental scatterplot rarely matches with the theoretical one. A normalizing/stretching procedure is therefore often required for them to fit together and for allowing soil moisture identification (Carlson 2005). This normalizing/stretching procedure relaxes the requirement for precise data about radiative fluxes and atmospheric fluxes and about soil/vegetation intrinsic properties. However, in some way it justifies a simpler approach which is the empirical method proposed by Sandholt 2002. This method is based on the experimental T-VI distribution only; no temperature computation is required. Two linear regressions are simply performed for fitting the low temperature border and the high temperature border of the scatterplot. The iso-moisture lines, assumed to be straight, are then evenly, i.e. linearly distributed between the wet edge and the dry edge. A large number of applications can now be found in the literature, they mainly deal with low resolution data, i.e. at field scale and landscape scale, as provided by satellite based sensors. The applicability to high resolution and multitemporal data was recently discussed (Maltese, 2010, Krapez 2011, 2012).

The drawing of the lines defining the wet and dry edges as described by Sandholt 2002 is rather subjective. A more systematic and objective approach was described in (Krapez 2011, 2012): for each VI interval, a low temperature limit and a high temperature limit are defined from the p percentile and the $100-p$ percentile (typically p is between 0.5% and 1.5%). The results are then smoothed with cubic splines to provide the wet and dry edges as reported on fig. 4. By this way the scatterplot is tightly bounded; in the same time,

possible outliers are rejected. At each Vegetation Index level, the Soil Vegetation Wetness Index (SVWI) is defined as the relative distance to the dry edge:

$$SVWI_{ij} = \frac{T_{ij} - T_{dry}(VI_{ij})}{T_{wet}(VI_{ij}) - T_{dry}(VI_{ij})}$$

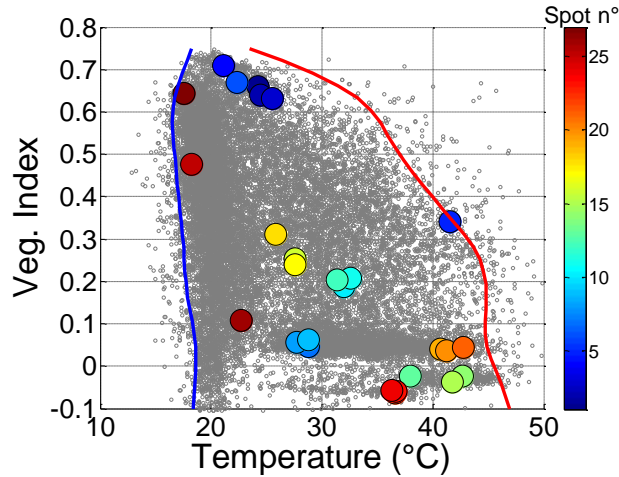


Figure 64 : Temperature-Vegetation Index scatterplot obtained during HyEurope 2007 campaign (from Krapez 2011).

The wet edge (in blue) and the dry edge (in red) are built from 1% and 99% percentile temperature values for varying vegetation index. The dots with scaled color correspond to different spots/fields and crops.

This “more objective” approach tightly follows the cold and hot borders of the scatterplot. Let us however stress that it assumes that this scatterplot is fully populated which means that the pixels in the scanned area must cover the whole vegetation cover fraction dynamic together with the whole soil wetness dynamic. If the scatterplot is not well populated along one of its edges, the corresponding edge line will show a depression in this area. The consequence is that the Soil Vegetation Wetness Index will show a bias in the affected VI range. In such a case it would probably be better to use straight lines for the cold and wet edges instead of matching too tightly to the experimental scatterplot. Nevertheless, when the flight line is definitely too short, even the implementation of straight edges will lead errors since the experimental scatterplot will not be representative enough of the full theoretical scatterplot showing all possible T-VI combinations.

The works described so far use only two observation variables, namely temperature and a vegetation index. They rely on an over-simplified representation of the heat and mass transfers between the elements of the complex soil/vegetation/ atmosphere system. A large number of parameters, in addition to soil moisture, actually have an impact on the apparent soil/canopy temperature. As these parameters may vary between the different vegetation types and soil types, it is expected that moisture cannot be unambiguously retrieved from a given couple of T-VI values. The inversion cannot lead to a unique solution. To solve this problem one has to consider additional observations.

Chauhan 2003 suggested adding surface albedo. When introducing the albedo, it is expected to separate areas according to the absorbed solar radiation. Albedo can be evaluated with a good precision from the reflectance measurement in a limited number of spectral channels in the solar spectrum. Recently we looked for separating vegetated areas according to another property, namely the fraction of green vegetation versus senescent vegetation (Krapez, 2011, 2012). A suitable index for quantifying the fraction of senescent vegetation is CAI (Cellulose Absorption Index). It is computed from the reflectance measured in three bands: one at $2.1\mu\text{m}$, the cellulose–lignin absorption maximum, and two at the shoulders of this absorption band, at $2\mu\text{m}$ and $2.2\mu\text{m}$:

$$CAI = 0.5(\rho_{2.0} + \rho_{2.2} - 2\rho_{2.1})$$

Two examples of 3D scatterplots with respectively albedo and CAI as the third parameter are reported on fig. 5. The boundary surfaces corresponding to the dry border, respectively the wet border, are again built from the p% percentile and the 100-p% percentile temperature values.

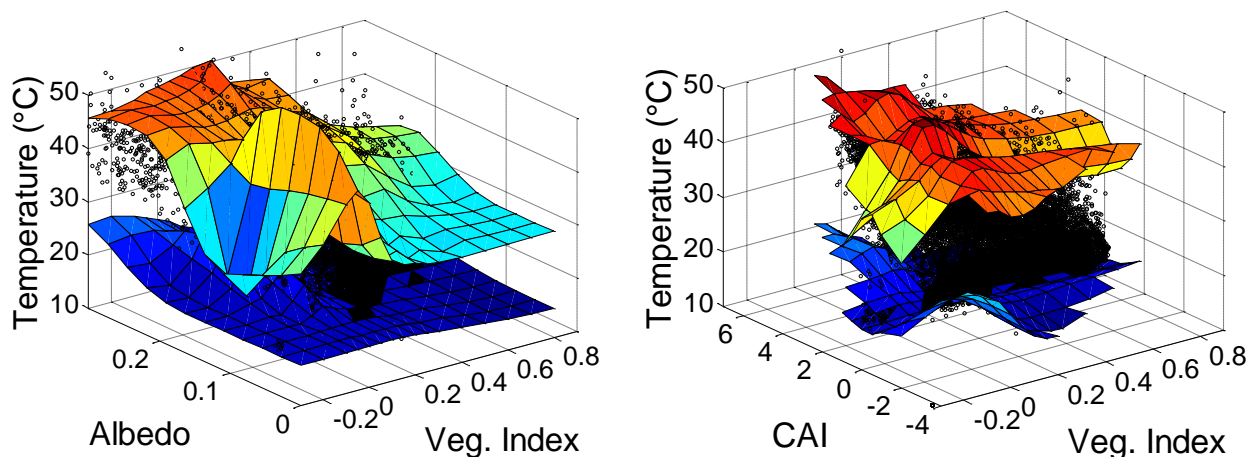


Figure 65 : Distribution of temperature, Vegetation Index and repectively albedo (left) and Cellulose Absorption Index (right). Each distribution is bounded on the hot side and on the cold side by the “dry”, respectively the “wet” boundary surfaces (from Krapez, 2011)

Introducing albedo didn't seem to provide an improvement in Krapez, 2011, whereas the addition of the Cellulose Absorption Index (CAI) showed to be more promising, indeed the correlation coefficient R^2 between Soil Vegetation Wetness Index and the gravimetric moisture content increased from 0.61 to 0.69. Nevertheless, the drawback of the proposed statistical approach for defining the wetness index is that the scatterplot must be well populated, i.e. it should present both dry soil and wet soil areas, for each couple of considered albedo-VI or CAI-VI values in the gridded plane. This is not always the case for a region of small extent.



2.3.2 Other Water Indexes

2.3.2.1 PWI (Plant Water Index) or WBI (Water Band Index)

The PWI (Plant Water Index) also called WBI (Water Band Index) as obtained by the ratio of R900 and R970 was used to map vegetation water content (Panaulas, 1997). It was however found to be affected not only by water content, but also by canopy structure and viewing geometry therefore highly dependent on bi-directional and geometrical effects of the vegetation canopy (Zarco, 2003).

2.3.2.2 NDWI (Normalized Difference Water Index) and SRWI (Simple Ratio Water Index)

The Normalized Difference Water Index (NDWI₁₂₄₀) as defined by $(R_{858} - R_{1240}) / (R_{858} + R_{1240})$ was suggested by Gao, 1996 in a theoretical study, demonstrating its potential applicability for canopy-level water content estimation based on the liquid water absorption band centered at 1240 nm enhanced by canopy scattering (Zarco, 2003). The Simple Ratio Water Index (SRWI) has also been considered R_{858} / R_{1240} (Zarco 2001, 2003). Since the same wavelength are used for NDWI₁₂₄₀ and for SRWI, without any doubt, the sensitivity of these indices to water content should be tightly correlated.

NDWI (Normalized Difference Water Index) and SRWI (Simple Ratio Water Index)

Other water indexes based on a normalized difference of reflectances were proposed in the past (Chen 2005): $NDWI_{1640} = (R_{858} - R_{1640}) / (R_{858} + R_{1640})$ and $NDWI_{2130} = (R_{858} - R_{2130}) / (R_{858} + R_{2130})$.

They all showed potential in estimating the vegetation water content (the measurements made by Chen, 2005 were conducted over corn and soybeans fields over a crop-growing period).

2.3.2.3 Indexes based on SWIR signal only

We also considered four other indexes specifically designed for evaluating the soil moisture content (SMC) for bare soils.

The WISOIL (Water Index SOIL) index was introduced by Whalley 1991. It is a ratio-based index between the reflectance at a strong water absorption band (1.45 μm) and the reflectance at weak water absorption band (1.3 μm). This index was shown to be linearly correlated with the SMC for three different soils (Bryant, 2003).

The three other indices are normalized indices: the NSMI (Normalized Soil Moisture Index) was introduced by Haubrock 2008: $NSMI = (R_{1800} - R_{2120}) / (R_{1800} + R_{2120})$.

The NINSOL (Normalized Index of NSWIR domain for SMC estimation from Linear correlation) and the NINSON (Normalized Index of NSWIR domain for SMC estimation from Non Linear correlation) were both introduced by Lesaignoux, 2010, Fabre 2015. In order to get an index that increases with moisture content we chose to take the opposite of NINSOL and NINSON and called them RNINSOL and RNINSON (R for "revised"):



$RNINSOL = -(R2080 - R2230) / (R2080 + R2230)$ and $RNINSON = -(R2120 - R2230) / (R2120 + R2230)$.

Since all these indices were designed for bare soils, we applied a mask in order to reject the pixels that corresponded to vegetated areas. The mask criterium was based on whether the OSAVI value was lower (1) or higher (0) than 0.3.

2.4 WADI 1 Campaign

2.4.1 Application of the VI-TIR Trapezoid method to Esparron and St Maximin data

As a preliminary result we present the outcome of the data processing performed on the images recorded on Feb. 16th along the Esparron North flight line (sequence n°7).

We first applied the VI-TIR Trapezoid method with the cold/warm edges setting according to the empirical method proposed by Sandholt 2002.

The spectral images provided by the VNIR hyperspectral camera used to compute the OSAVI index are shown on Fig. 66. The resulting OSAVI image is shown on Fig. 67.

The Thermal Infrared image (TIR) as constructed from the microbolometer infrared camera 2D data is shown on Fig. 68. The processing includes mosaiking with georeferencing and finally coregistration with respect to the VNIR images (GeFolki software, Brigot, 2016).

The 2D scatterplot obtained from the OSAVI image and the TIR image is shown on Fig. 69. The cold edge (blue) and the warm edge (red) are straight lines that have been set empirically. The objective was to tightly fit to the boundaries of the scatter while possibly excluding a few outliers (outliers may originate from real artefacts like shadows, man-made small or thin structures, or from local residual errors occurring during the TIR construction process: mosaiking, georeferencing, coregistration).

Let us mention that the 2D scatterplot seems not evenly populated: the cold edge looks more bent than it is usually observed in the results from satellite images suggesting that vegetated areas with high water content are missing in the considered flight line. Similar remarks could be made about the warm side of the scatter: very dry areas with either low VI or high VI seem to be missing.

The Wetness Index (WI) as inferred from these two cold (wet) and warm (dry) edges is shown on Fig. 70. The scale for this water index should be understood as follows: it ranges from 0 to 1; 0 corresponds to the warmest temperature pixels (interpreted as the driest pixels) observed for this particular VI range, resp. 1 corresponds to the coldest temperature pixels (interpreted as the wettest pixels) observed for this particular VI range.

Two areas were selected in the Water Index (WI) map that are representative of a "wet" surface and a "dry" surface (see fig. 11). They are particularly distinctive on the thermal image (fig. 68) and on the Water Index map as well. Near the south-east corner of the "wet" area is a pipe elbow.

On fig. 72 we reported a composite picture of this area that was taken four months later (June 12th) during an on-site search for leaks. The selected "dry" and "wet" surfaces are delineated. We can guess that the "wet" area corresponds actually to a cuvette. The

areas on both sides are more elevated (on the left is the selected “dry” area and on the right is a nearly bare soil surface with sparse grass).

As a matter of fact, at the south border of the “wet” area was detected a puddle continuously fed with fresh water has been detected(see fig. 73).

The quantitative results are:

“Dry” area : Mean: 0.63119 Std: 0.039889

“Wet” area : Mean: 0.83425 Std: 0.042874

Differential Signal : 0.20305 Noise: 0.04183 S/N: 4.8542

The so-called differential “Signal” corresponds to the difference between the mean values observed on both surfaces. The “noise” corresponds to the standard deviation of the signal observed on both surfaces after suppressing the difference on the mean levels.

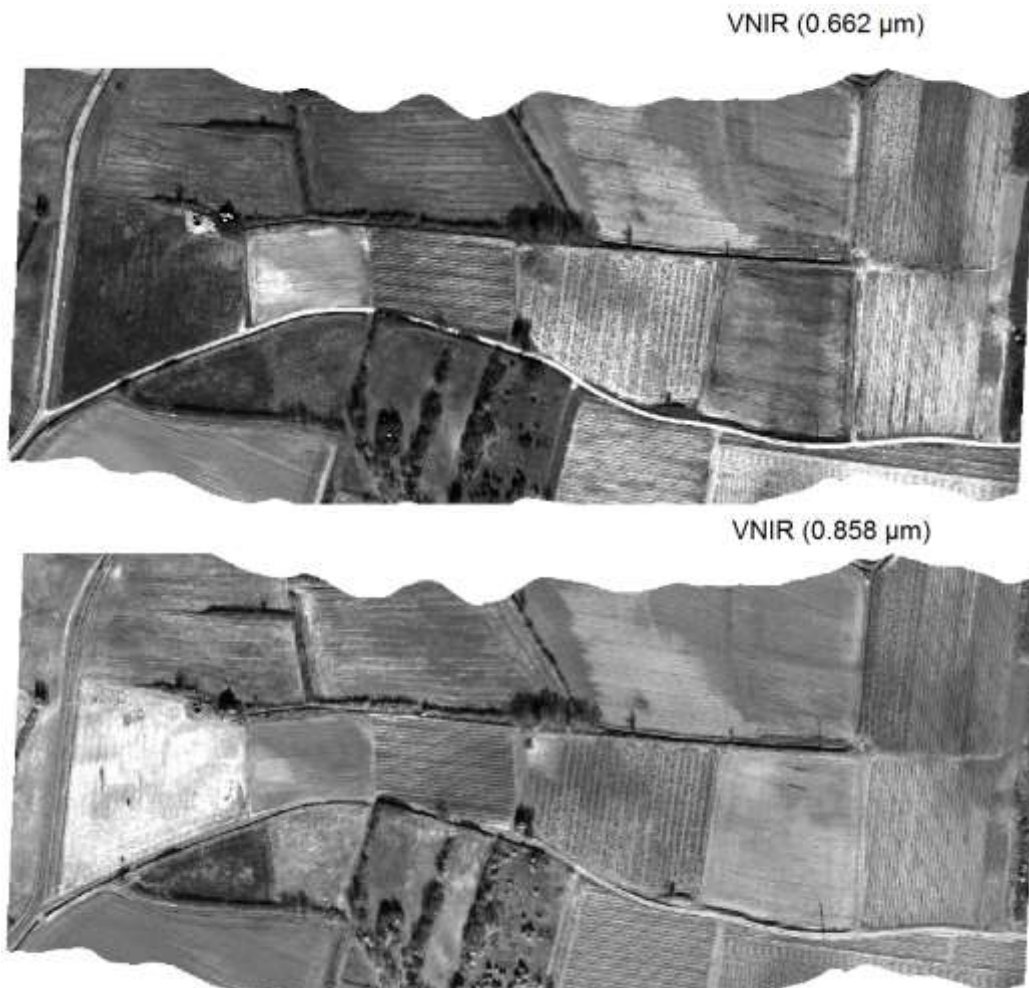


Figure 66 : Esparron North (seq. 7). Images recorded by the VNIR hyperspectral camera. Band 0.662 μ m (top) and band 0.858 μ m (bottom).

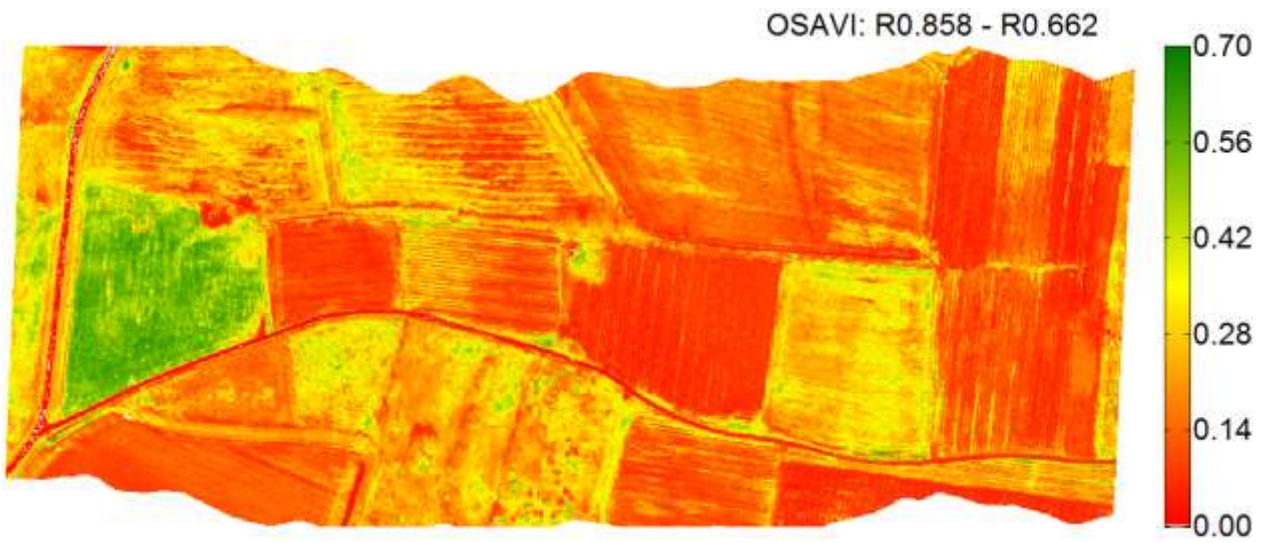


Figure 67 : Esparron North (seq. 7). OSAVI Vegetation index map. Higher values correspond to vegetated areas, lower values correspond to bare soil.

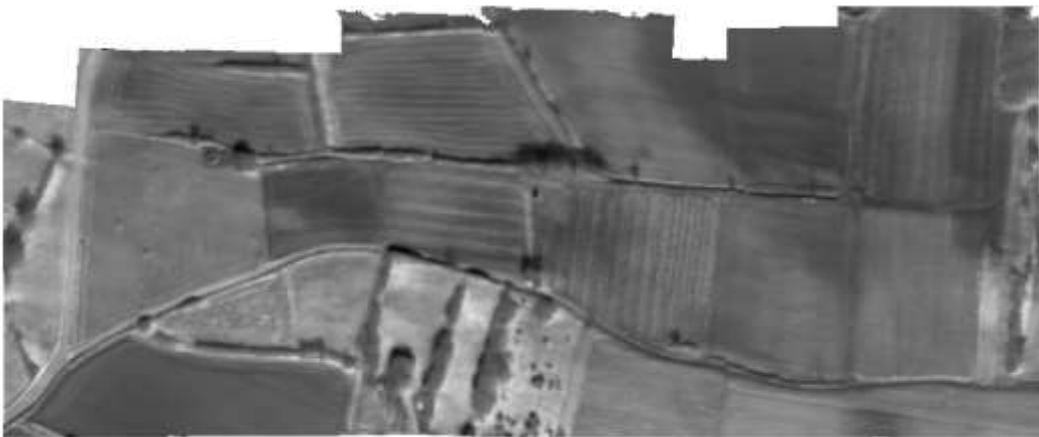


Figure 68 : Esparron North (seq. 7). Thermal Infrared Image (TIR) as built from the individual 2D images provided by the microbolometer camera. Interpretation of the grey levels: dark or clear pixels correspond to low radiance temperature, resp. higher radiance temperature.

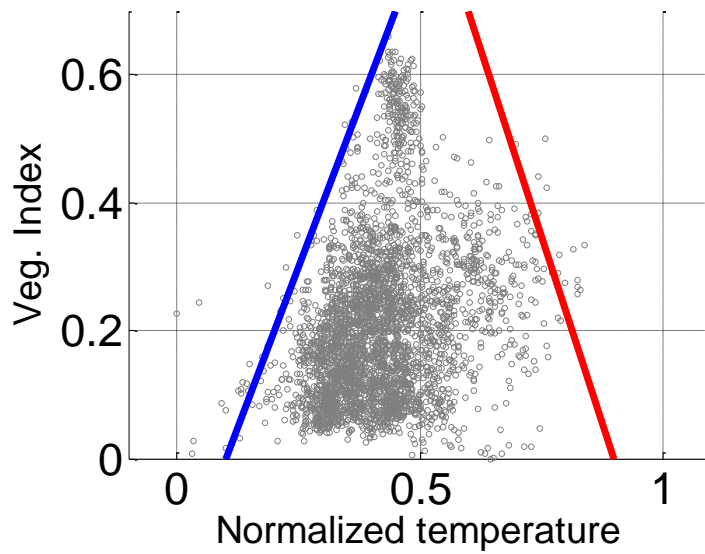


Figure 69 : 2D distribution of normalized temperature and vegetation index (OSAVI). The cold edge (blue) and the warm edge (red) have been positioned so that the trapezoid figure contains essentially all the scatter, except a few outliers.

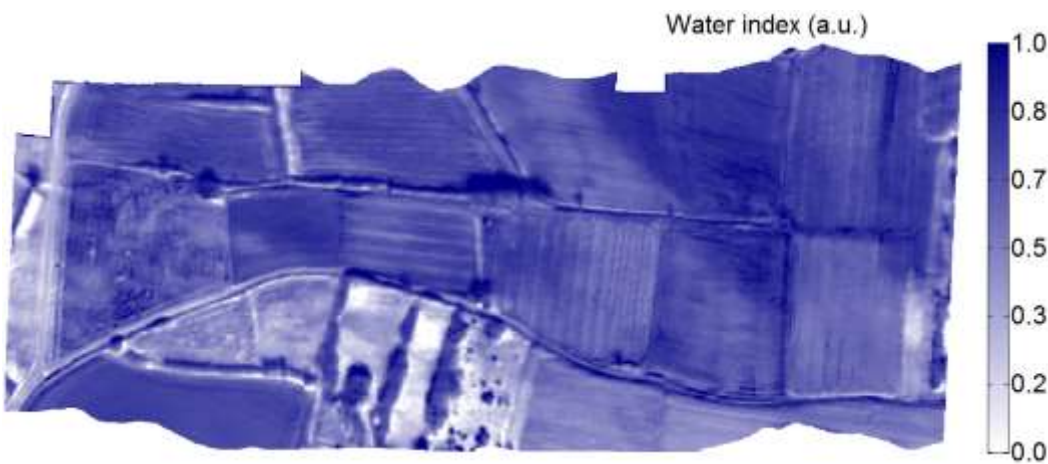


Figure 70 : Water Index (WI) map as obtained from the scaling of brightness temperature defined by the cold and wet edges on fig. 9. The scale for the WA is arbitrary.

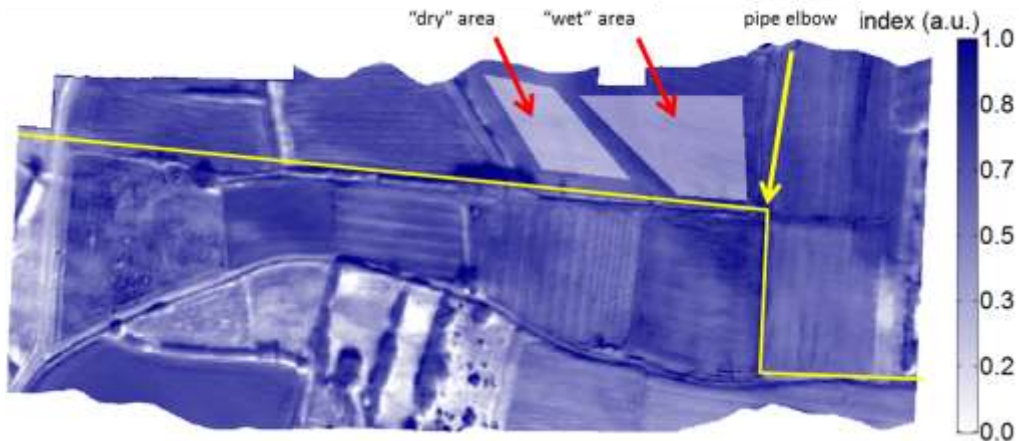


Figure 71 : Selection of two areas in the Water Index (WI) map that are representative of a “wet” surface and a “dry” surface. A buried pipe (in yellow) is running south from these two areas with an elbow near the south-east corner of the “wet” area.

"Dry" area : Mean: 0.63119 Std: 0.039889
 "Wet" area : Mean: 0.83425 Std: 0.042874
 Differential Signal : 0.20305 Noise: 0.04183 S/N: 4.8542



Figure 72 : “Wet” surface (blue polygon) and “dry” surface (red polygon) selected for the performance comparison. This picture was taken on June 12th after meadow has well grown.

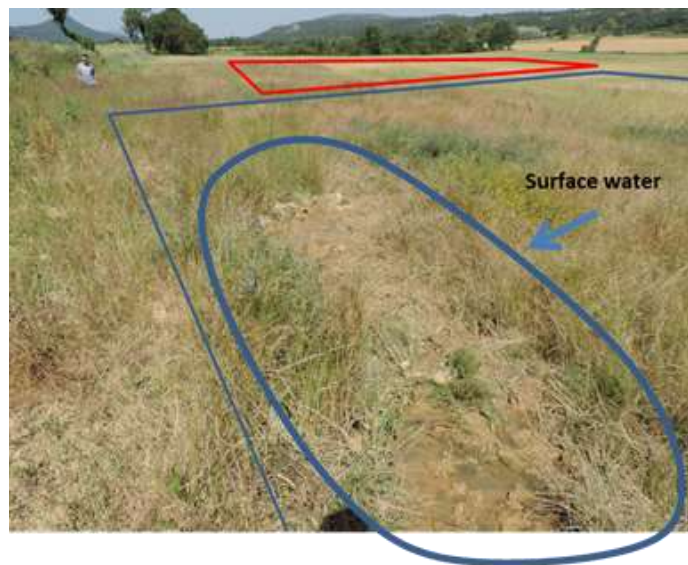


Figure 73 : In the south part of the “wet” area (blue polygon) a continuously fed puddle has been detected.

The results obtained in the Saint Maximin area are reported on fig. 74 - 75.

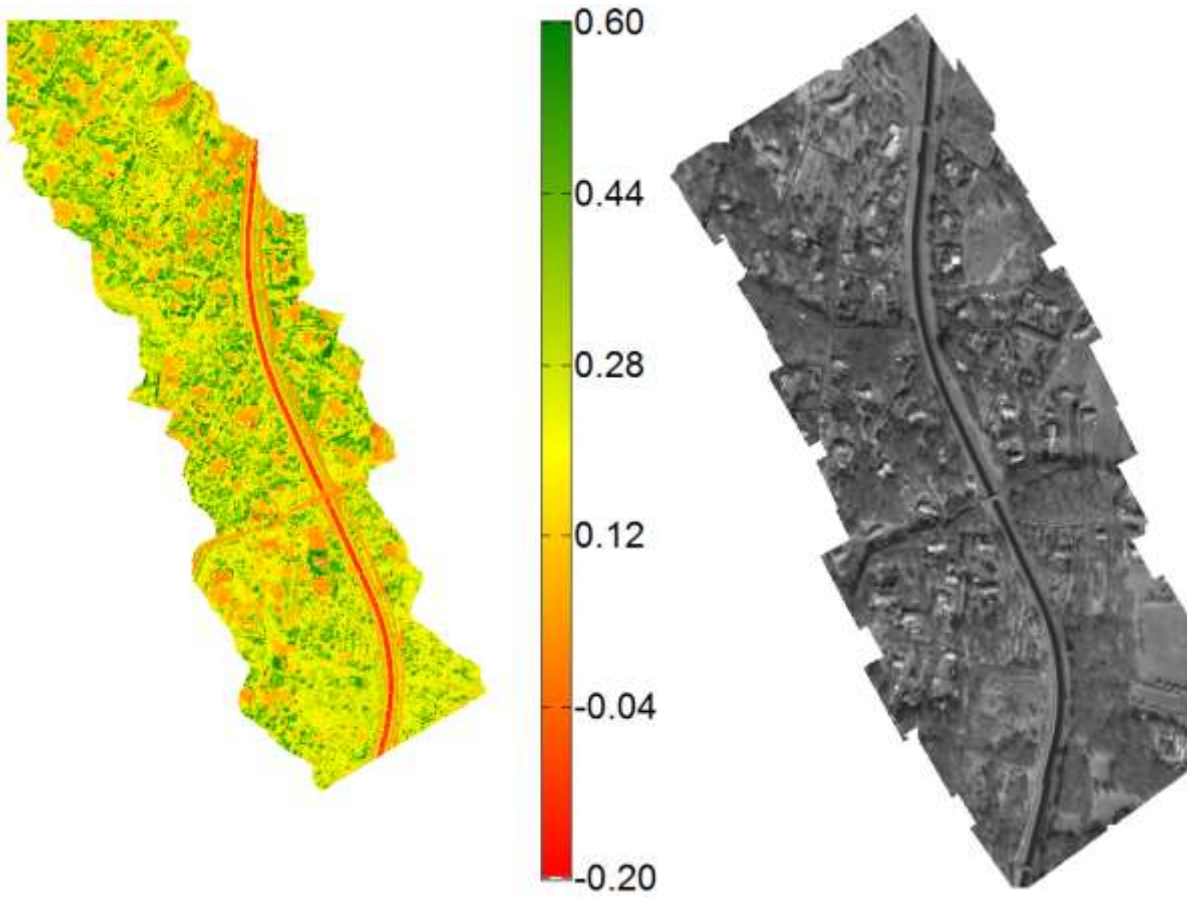


Figure 74 : Saint Maximin. Image of the OSAVI index (left) and mosaic of TIR images.

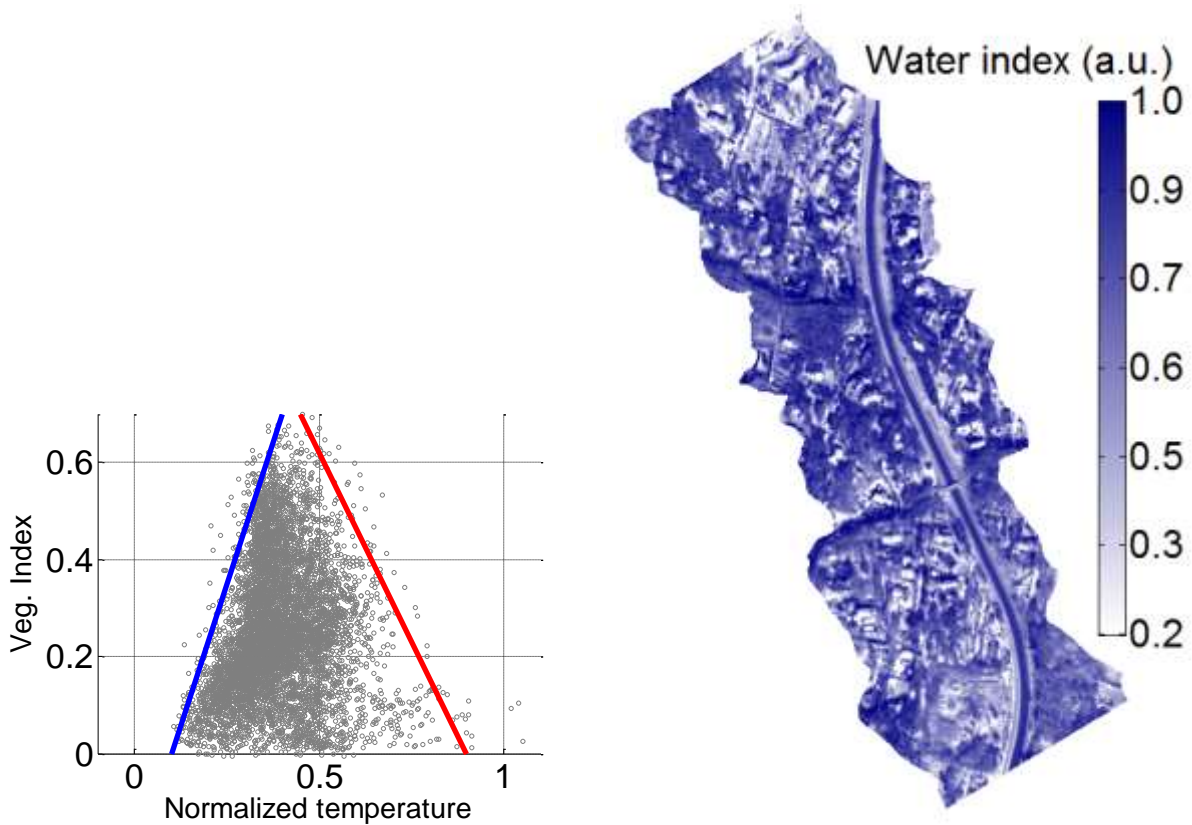


Figure 75 : Saint Maximin. Two-dimensional scatter of OSAVI and TIR values (left) and resulting water index map (right).

2.4.2 Assessment of other Water Indexes to Esparron data

The spectral images in the VNIR band that were necessary to process these supplementary indices are presented on Fig. 76.

Those in the SWIR band are on Fig. 77.



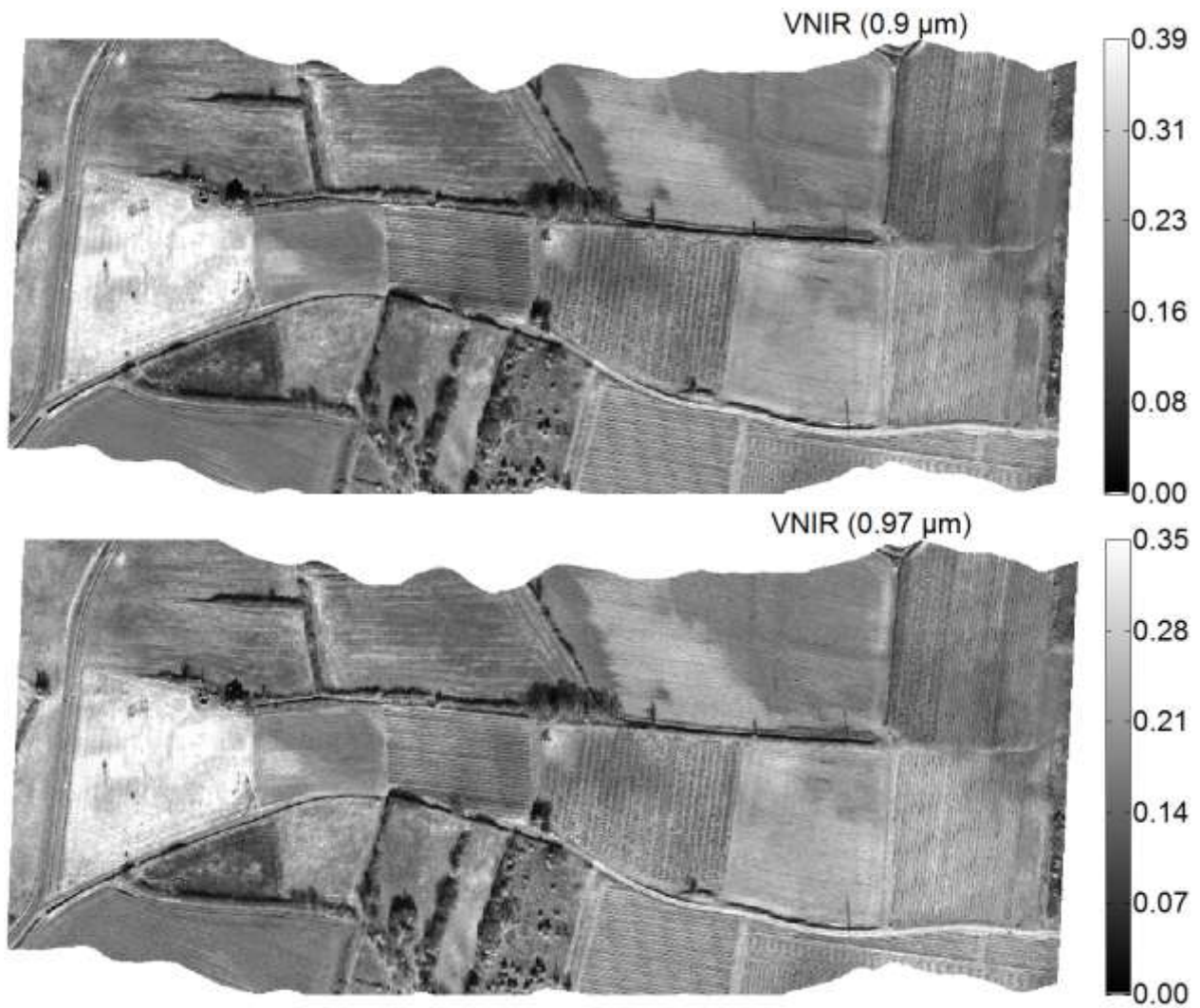
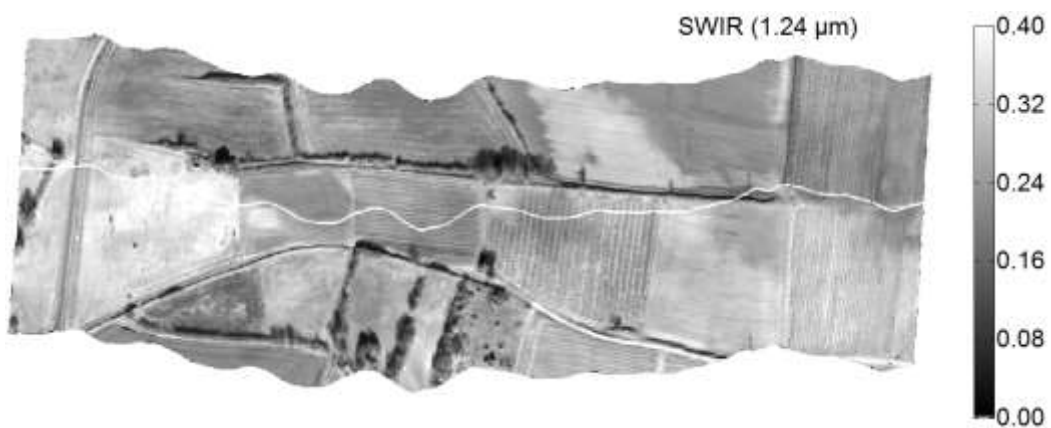
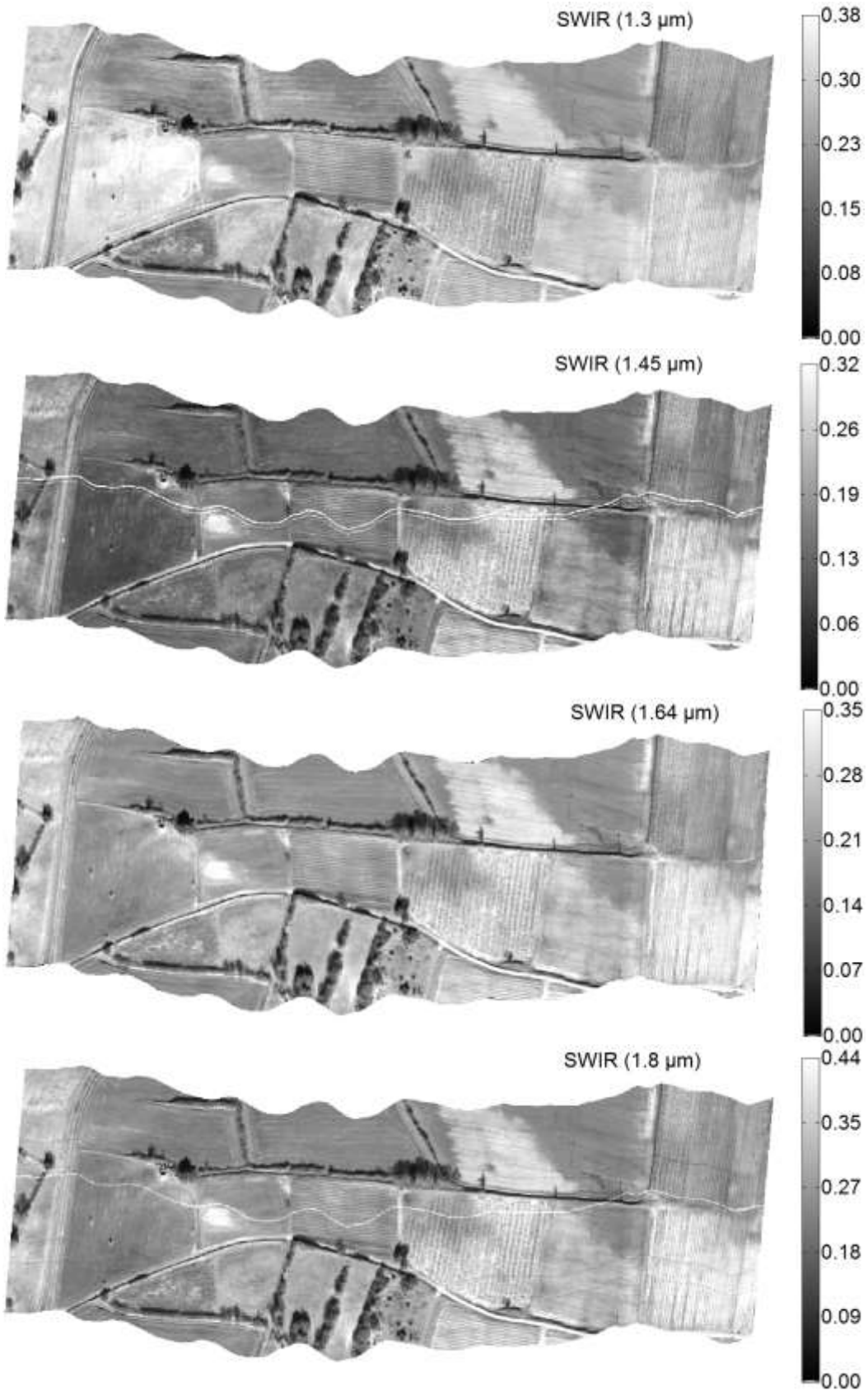
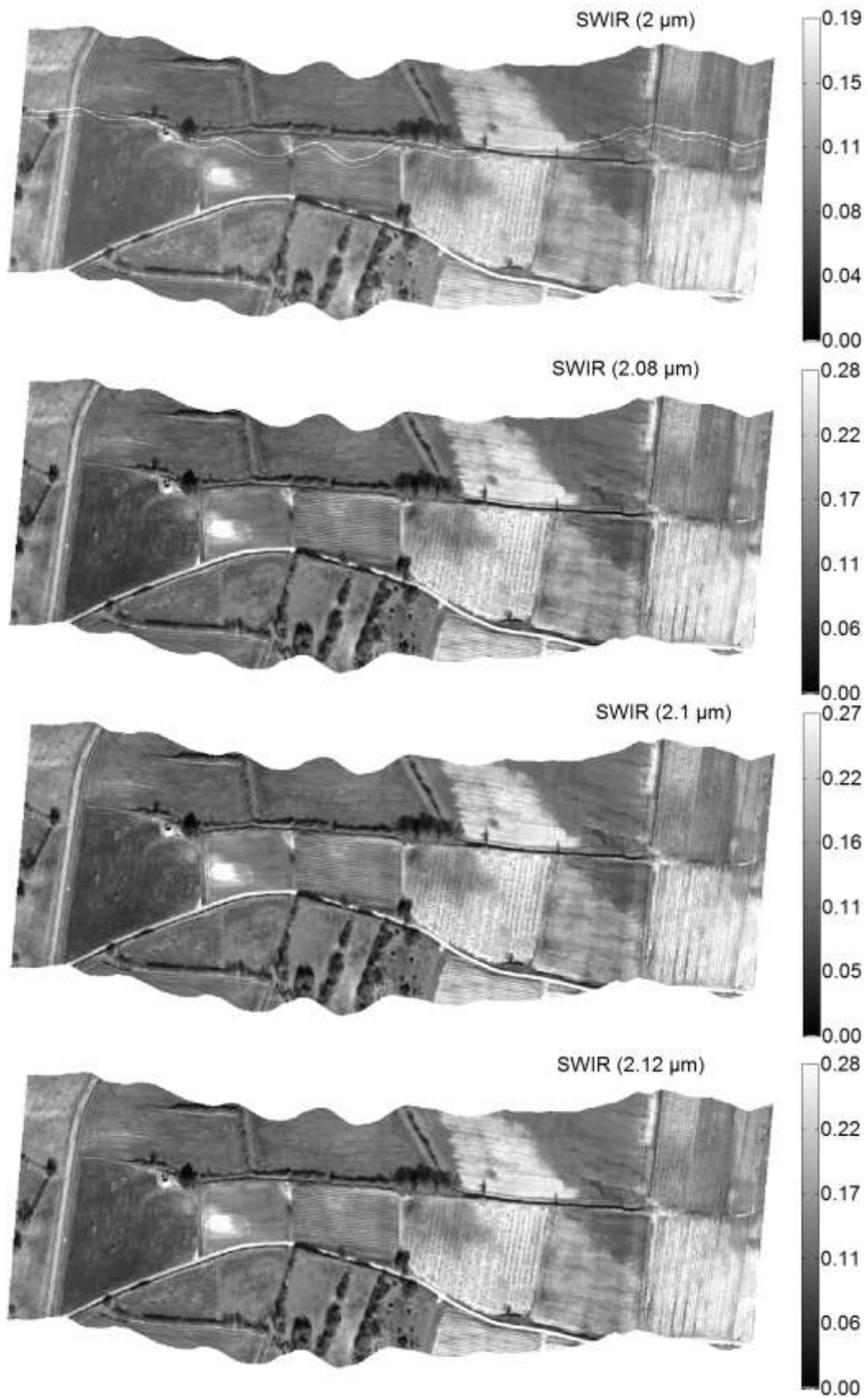


Figure 76 : Esparron North (seq. 7). Images in the VNIR band used for processing the Water Indexes.







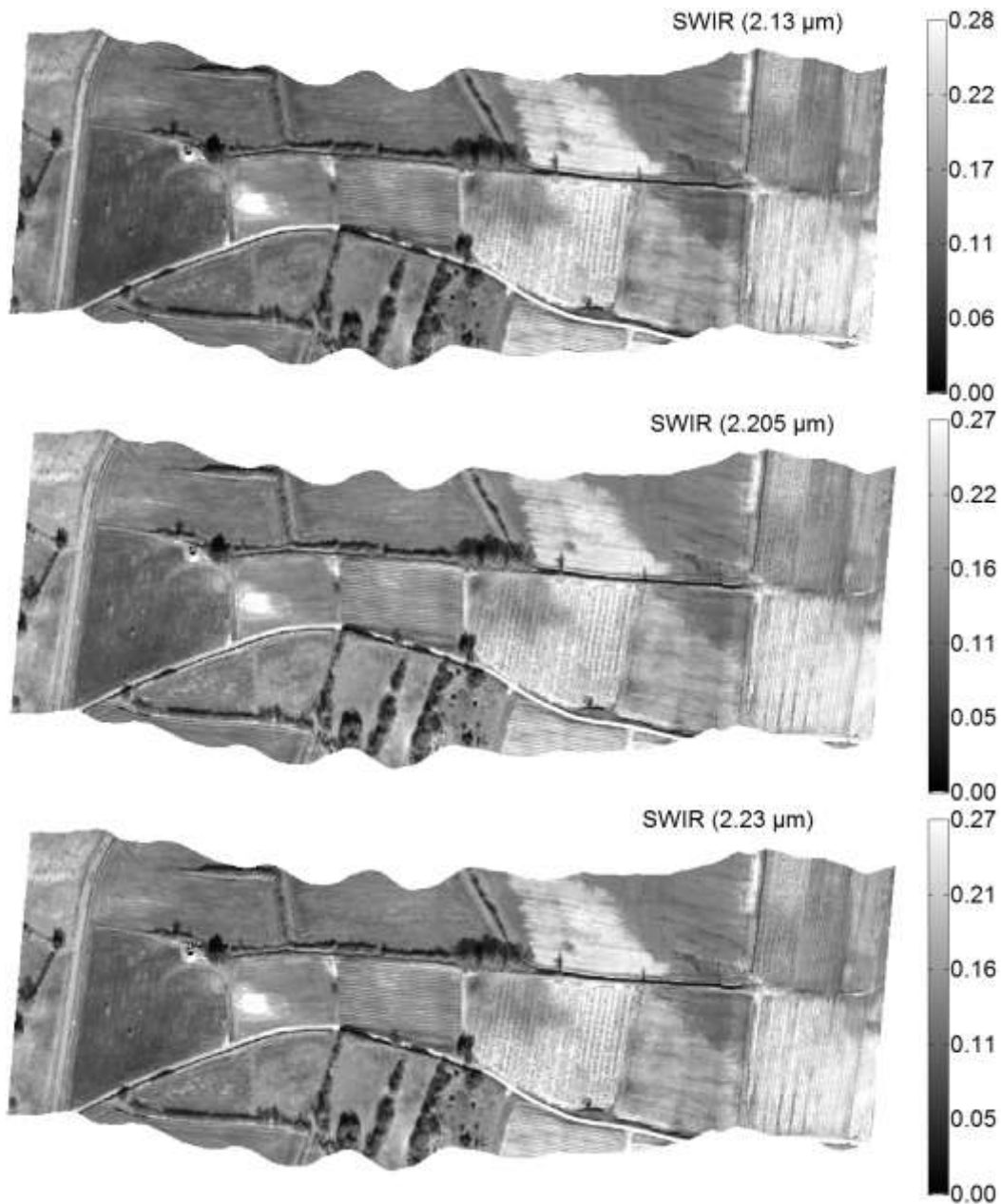


Figure 77 : Esparron North (seq. 7). Images in the SWIR band used for processing the Water Indexes.

2.4.2.1 PWI (Plant Water Index) or WBI (Water Band Index)

The spectral images at 900nm and 970nm are provided on Fig. 78.

The PWI (or WBI) index is reported on Fig. 70. Since during the February flight the vegetation was still dormant, most of the plots were with bare or nearly bare soil. As a matter of fact, the OSAVI plot on Fig. 61 showed rather low values of the vegetation index, except in a plot in the left part of the image (green area on fig. 61). Processing the PWI (WBI) on this type of surfaces is therefore not very well justified. A mask revealing only vegetated surfaces should be applied. Anyway, the PWI (WBI) map on Fig. 68 shows extremely low contrasts. In particular, there is no detectable difference between the

reference "wet" and "dry" polygons. Anyway, the mean difference (0.01 a.u.) is far below the noise level (0.25 a.u.).

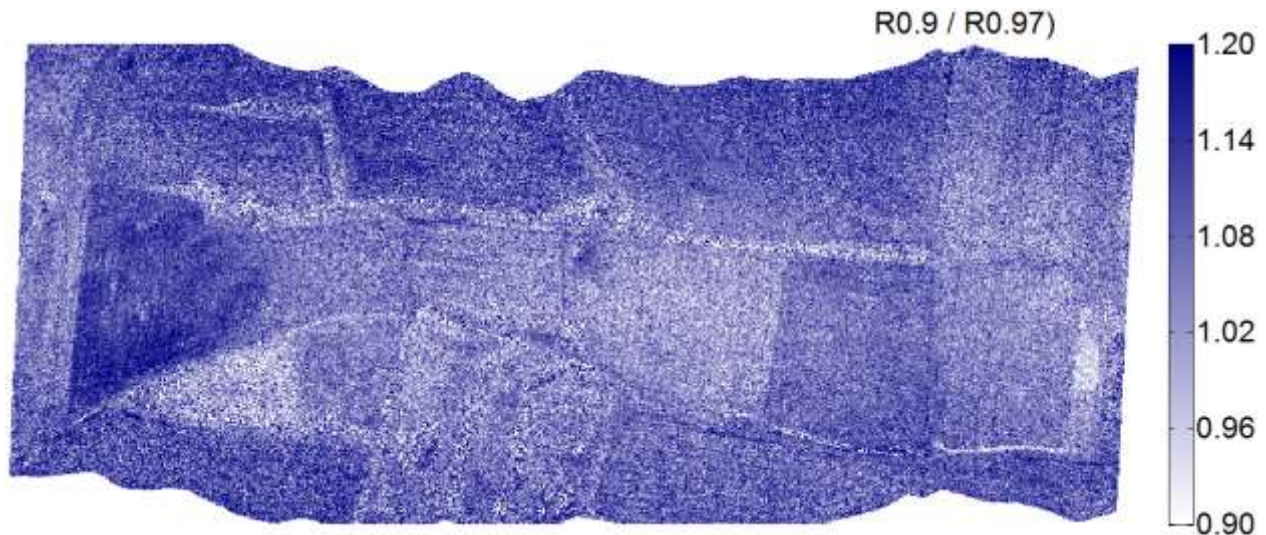


Figure 78 : Esparron North (seq. 7). Map of the WBI or PWI index.

"Dry" area, Mean: 1.0938 Std: 0.065958

"Wet" area, Mean: 1.0969 Std: 0.080357

Differential signal : 0.0030988 Noise: 0.07552 S/N: 0.041033

2.4.2.2 NDWI (Normalized Difference Water Index) and SRWI (Simple Ratio Water Index)

The map of $NDWI_{1240}$ is reported on Fig. 79. The one of SRWI is on Fig. 80.

Again, like for WBI(PWI), a vegetation mask should be applied. Nevertheless, the differentiation between the reference "wet" and "dry" areas is still very difficult. $NDWI_{1240}$ (fig. 79) and SRWI (fig. 80) provide nearly the same S/Nof about 0.6 which is unfortunately still less than 1.

In the present case, $NDWI_{1640}$ and $NDWI_{2130}$ only showed a marginal improvement over the maps of $NDWI_{1640}$ and $NDWI_{2130}$ are reported on fig. 81 and 82. The contrast to noise ratio over the two reference areas increased from 0.6 for $NDWI_{1240}$ to 1 for $NDWI_{1640}$ and then 1.6 for $NDWI_{2130}$.

The point is that, as already mentioned, the references areas were not covered with dense, green vegetation during the experiment performed in February. For this reason, without surprise, the water indexes designed for vegetation water content sensing don't show high performances.

The analysis should be performed again on images recorded during the growing season before discarding these indexes.

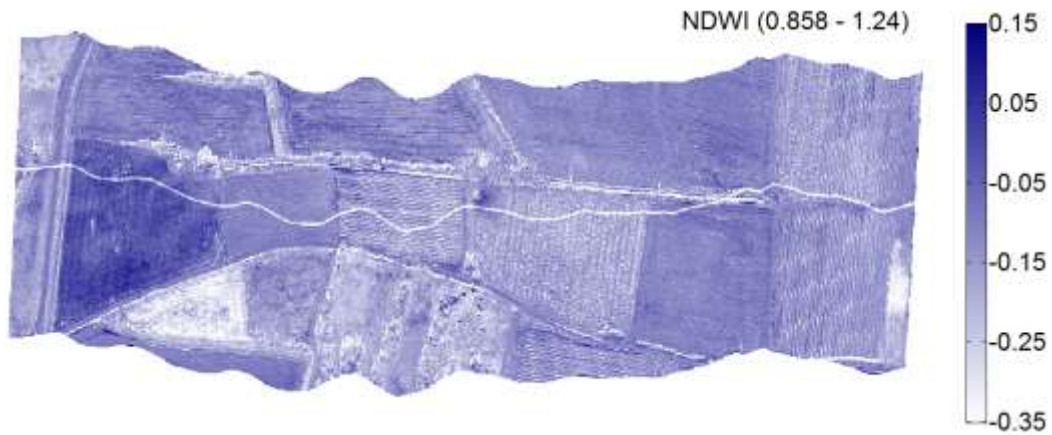


Figure 79 : Esparron North (seq. 7). Map of the NDWI₁₂₄₀ index.

"Dry" area: Mean: -0.12253 Std: 0.035129
 "Wet" area: Mean: -0.10023 Std: 0.038397
 Differential signal : 0.022295 Noise: 0.037392 S/N: 0.59625

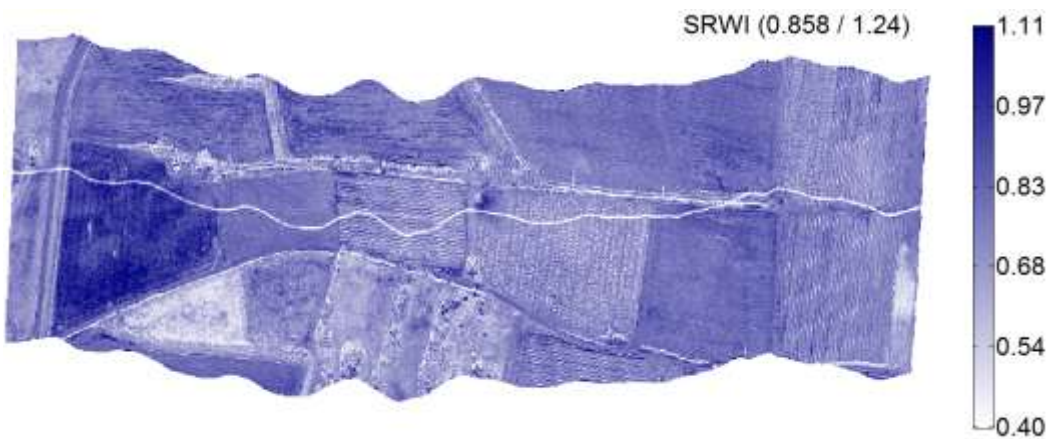


Figure 80 : Esparron North (seq. 7). Map of the SRWI index.

"Dry" area: Mean: 0.78291 Std: 0.053922
 "Wet" area: Mean: 0.81958 Std: 0.062926
 Differential signal : 0.036668 Noise: 0.060218 S/N: 0.60892

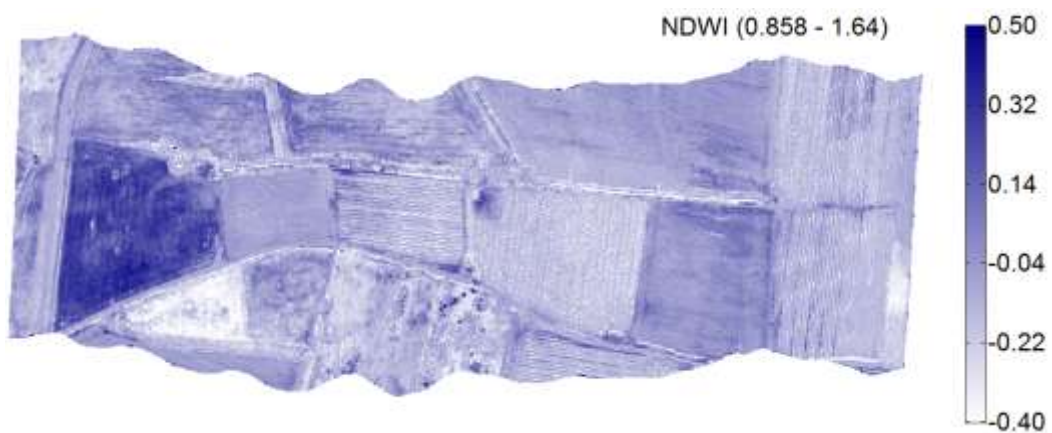


Figure 81 : Esparron North (seq. 7). Map of the NDWI₁₆₄₀ index.

"Dry" area: Mean: -0.088658 Std: 0.047857
 "Wet" area: Mean: -0.035625 Std: 0.053319
 Differential signal : 0.053032 Noise: 0.051649 S/N: 1.0268

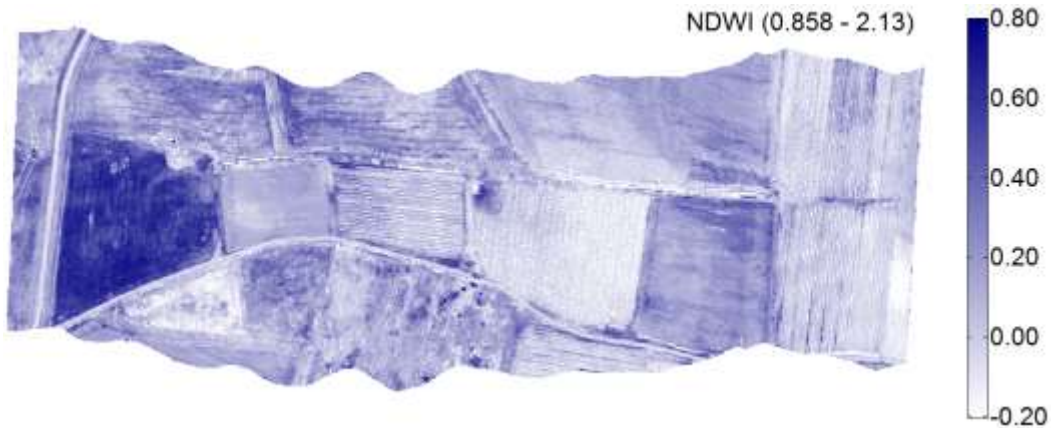


Figure 82 : Esparron North (seq. 7). Map of the NDWI₂₁₃₀ index.

"Dry" area: Mean: 0.062477 Std: 0.067868
 "Wet" area: Mean: 0.17836 Std: 0.070958
 Differential signal : 0.11588 Noise: 0.069992 S/N: 1.6557

2.4.2.3 Indexes based on SWIR signal only

The results for WISOIL, NSMI, RNINSOL and RNINSON are respectively on fig. 83, 84, 85 and 86. The highest contrast to noise ratio over the two reference areas is obtained with the RNINSOL index, i.e. about 3.0.



Figure 83 : Esparron North (seq. 7). Map of the WISOIL index.

"Dry" area: Mean: 1.3456 Std: 0.11238
 "Wet" area: Mean: 1.6091 Std: 0.14427

Differential signal : 0.26359 Noise: 0.13507 S/N: 1.9514

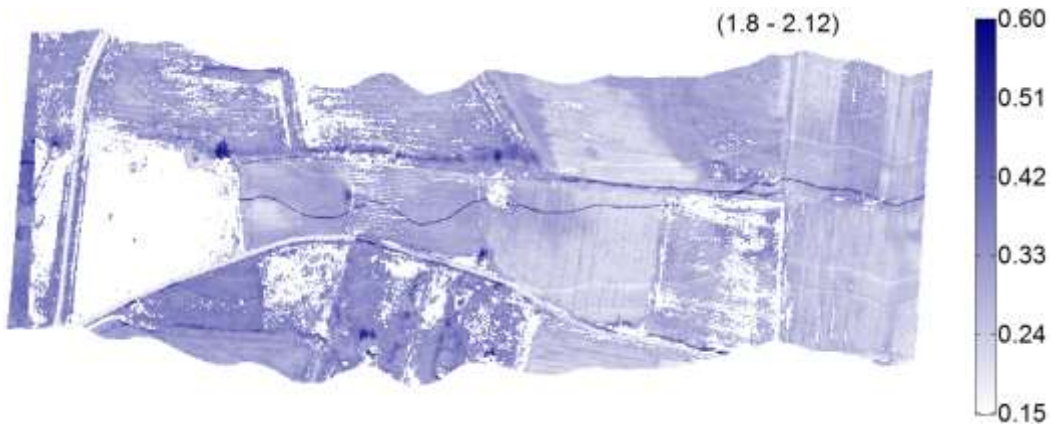


Figure 84 : Esparron North (seq. 7). Map of the NSMIindex.

"Dry" area: Mean: 0.24618 Std: 0.024267

"Wet" area: Mean: 0.30931 Std: 0.024865

Differential signal : 0.063136 Noise: 0.024679 S/N: 2.5583



Figure 85 : Esparron North (seq. 7). Map of the RNINSOLindex (the opposite is shown here for getting an increasing index value with increasing moisture)

"Dry" area: Mean: 0.0076934 Std: 0.018615

"Wet" area: Mean: 0.064392 Std: 0.018582

Differential signal : 0.056699 Noise: 0.018592 S/N: 3.0496



Figure 86 : Esparron North (seq. 7). Map of the RNINSON index (the opposite is shown here for getting an increasing index value with increasing moisture)

"Dry" area: Mean: -0.0011 Std: 0.0095491

"Wet" area: Mean: 0.028399 Std: 0.010811

Differential signal : 0.029499 Noise: 0.010424 S/N: 2.83

We also plotted the CAI index on fig. 87:

The cellulose–lignin broad absorption feature at 2.1 μ m was used by Daughtry 12001 to discriminate crop residues from soil. However, as water content increases, this feature progressively disappears. This tendency was also observed by Kokaly, 2009, between fresh and dry vegetation (pine needles) and on modelled leaf reflectance spectra. Altogether, a high positive CAI would indicate the presence of senescent or dry vegetation. On the opposite, a CAI close to 0 would indicate wet vegetation (senescent or fresh). The soil spectra in Lesaignoux thesis indicate that the CAI should be a negative increasing function of the moisture content. In summary the presence of water (in soil or vegetation) would be revealed by a CAI close to 0. On the contrary high absolute values indicate either the presence of dry vegetation (CAI>0) or dry bare soil (CAI <0).

The CAI index is plotted on fig. 87. This representation is rather difficult to interpret since the CAI is a decreasing or increasing function of wetness depending on the type of surface. Since values close to 0 are those of higher interest we plotted the absolute value of CAI on fig. 88.

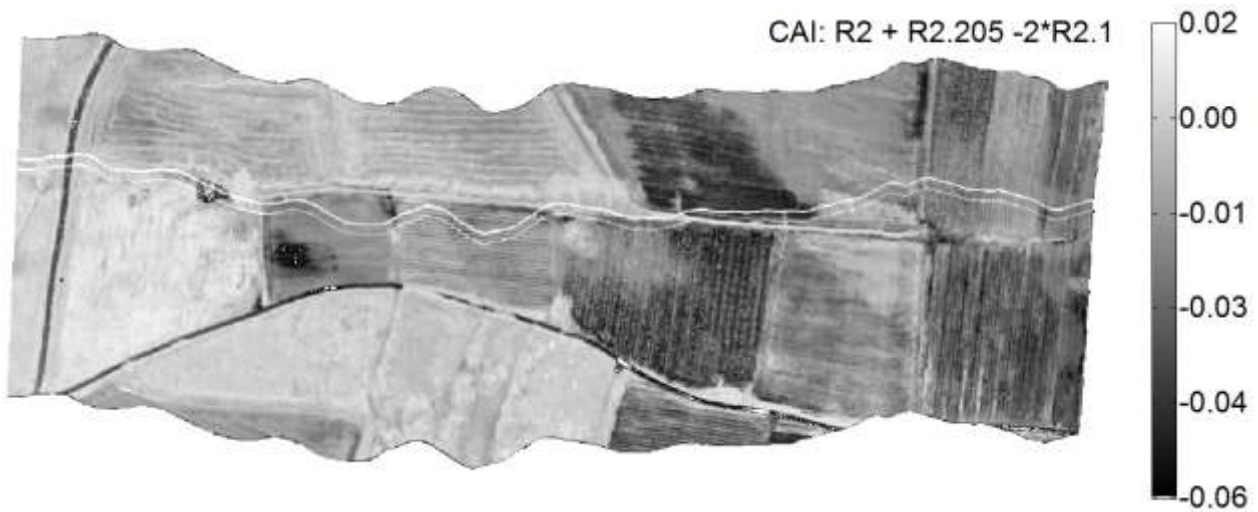


Figure 87 : Esparron North (seq. 7). Map of the CAI index. The double wavy line is an artefact of the hyperspectral camera. Values close to 0 indicate wet soil or wet or fresh vegetation.

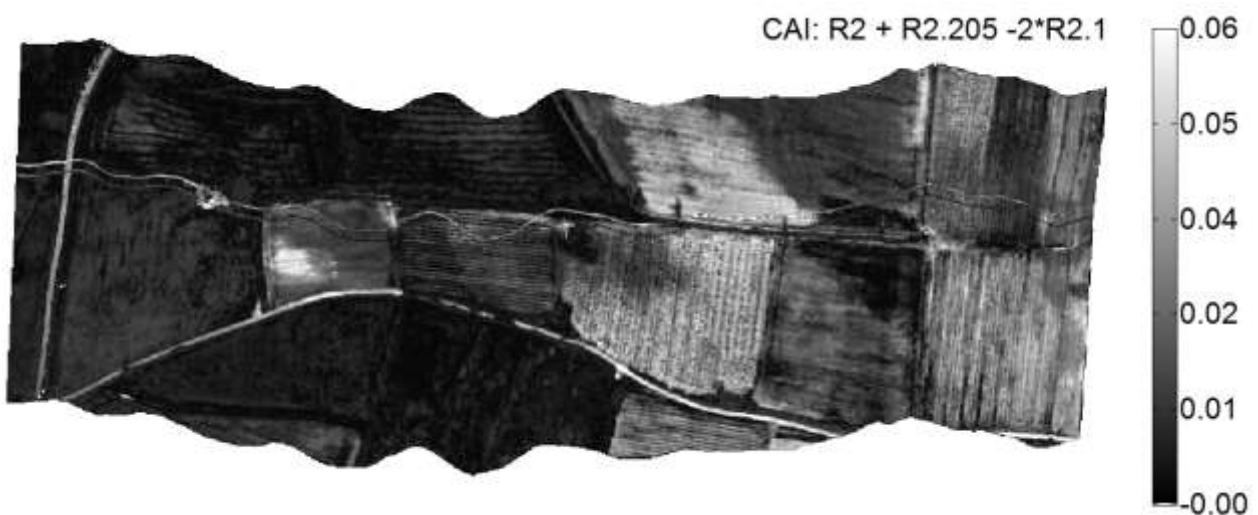


Figure 88 : Esparron North (seq. 7). Map of the absolute value of the CAI index. The double wavy line is an artefact of the hyperspectral camera. Values close to 0 indicate wet soil or wet or fresh vegetation.

Based on the global tendency that for both vegetation and soil the reflectance slope between $2\mu\text{m}$ and $2.2\mu\text{m}$ increases with moisture content, from negative values to positive values, we propose the following moisture normalized index:

$$\text{NMI}_{222} = \frac{(R_{2200} - R_{2000})}{(R_{2200} + R_{2000})}$$

It is plotted on fig. 89.

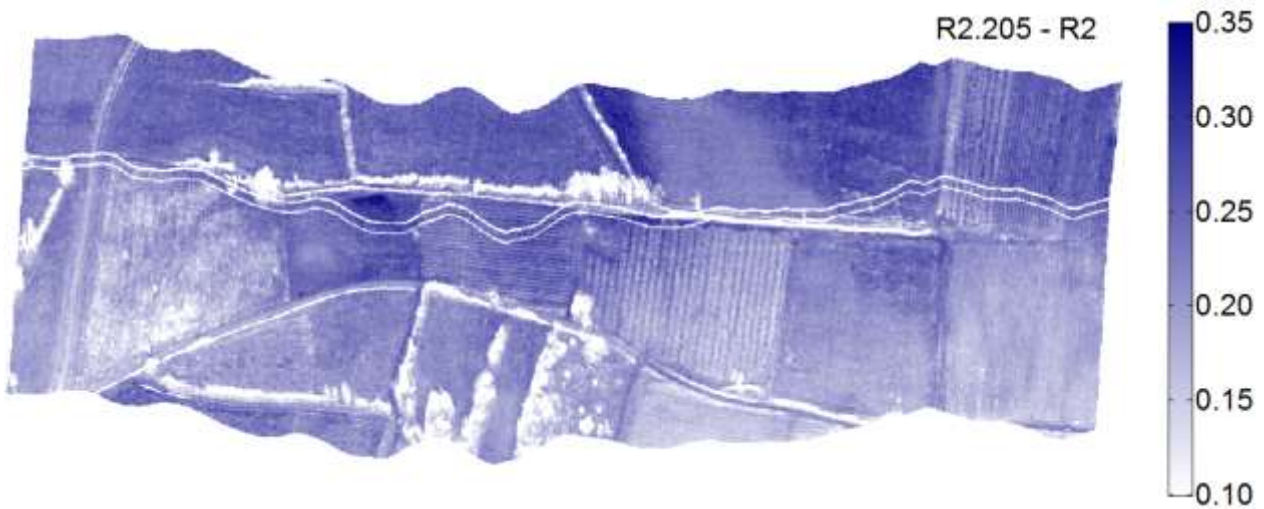


Figure 89 : Esparron North (seq. 7). Map of the NMI222 index. The double wavy line is an artefact of the hyperspectral camera.

"Dry" area: Mean: 0.23126 Std: 0.029888

"Wet" area: Mean: 0.27224 Std: 0.027196 (after excluding the spurious signal)

Summary: Differential signal : 0.040982 Noise: 0.028251 S/N: 1.4506

2.4.3 Comparison of the results

The results in terms of contrast to noise ratio between two areas, one of them showing a higher humidity than the other one (large puddle at the highest level border –south border) are summarized on fig. 90.

These first results clearly highlight that the Trapeze method (VNIR + TIR) shows the best performances in terms of discrimination between the two surfaces.

Further work is needed for confirming this tendency by processing the data recorded over other places and other seasons.

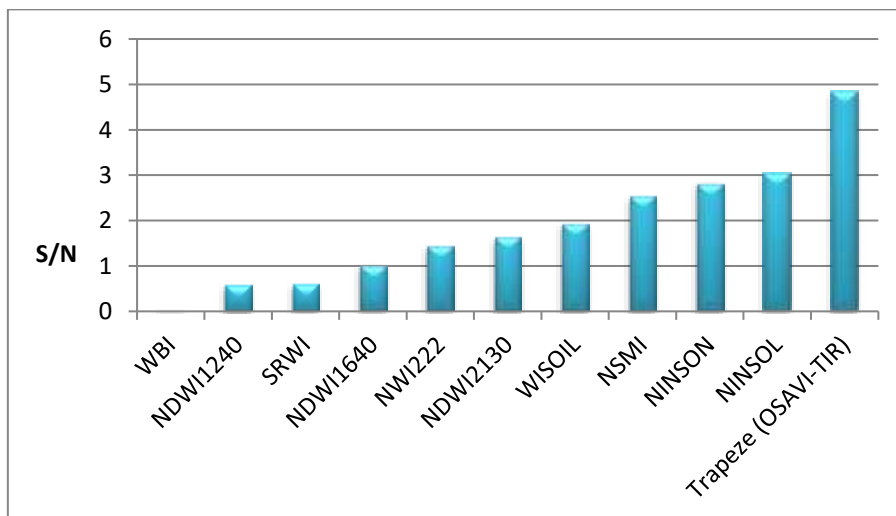


Figure 90 : Esparron North (seq. 7). Signal (contrast) to noise ratio between a "wet" area and a "dry" area obtained with different water indices.

2.5 WADI 2 Campaign

2.5.1 Le Tholonet

The OSAVI map is on fig. 91. The thermal infrared map is on fig. 92. The 2D scatter of OSAVI vs TIR is on fig. 93 and the resulting water index map is on fig. 94. A close up in the leak area is on fig. 95. The left arrow indicates the position of a real leak (leak made on purpose on a buried pipe – the trench was refilled and bare soil was on surface). The right arrow indicates the position of a reference area (bare soil at the surface like over the left trench). The leakage is clearly seen on fig. 95 (dark area encompassing both refilled trenches). It is likely that water diffused on both sides of the left trench and reached the reference area.

The RNINSOL images are on fig. 96. The refilled trenches with bare soil are clearly seen. However no contrast is detected over the nearby vegetation that would indicate a leakage.

The RNINSON images on fig. 97 and CAI images on fig. 98 are equally negative.

On fig. 98b to 98g we added a close-up of the maps of all the other considered indexes: NSMI, WISOIL, NDWI2130, NDWI1640, SRWI, NDWI1240. None of them shows a significant contrast in the vicinity of the leak.

It is now clear that the Thermal Infrared signal is the only one that reveals an important contrast around the leak (see the close-up on fig. 92). The trapezoid method is then capable of providing images bringing robust information on the present soil moisture.

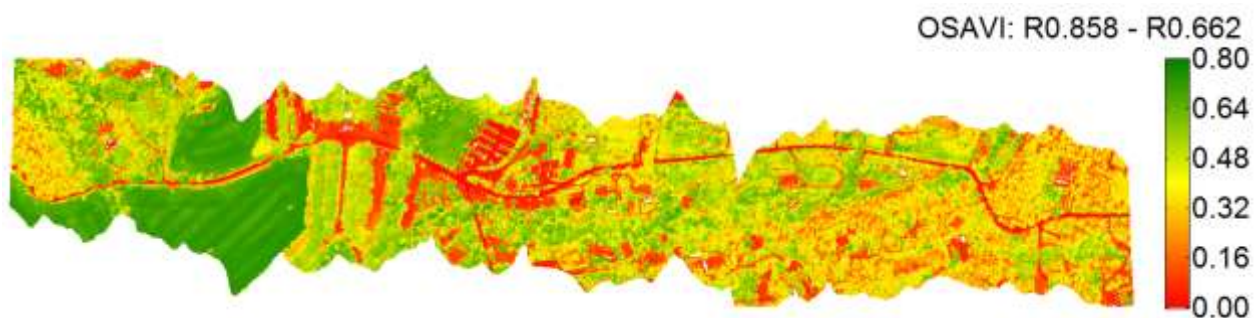


Figure 91 : Le Tholonet (seq. 2). OSAVI Vegetation index map. Higher values correspond to vegetated areas, lower values correspond to bare soil.

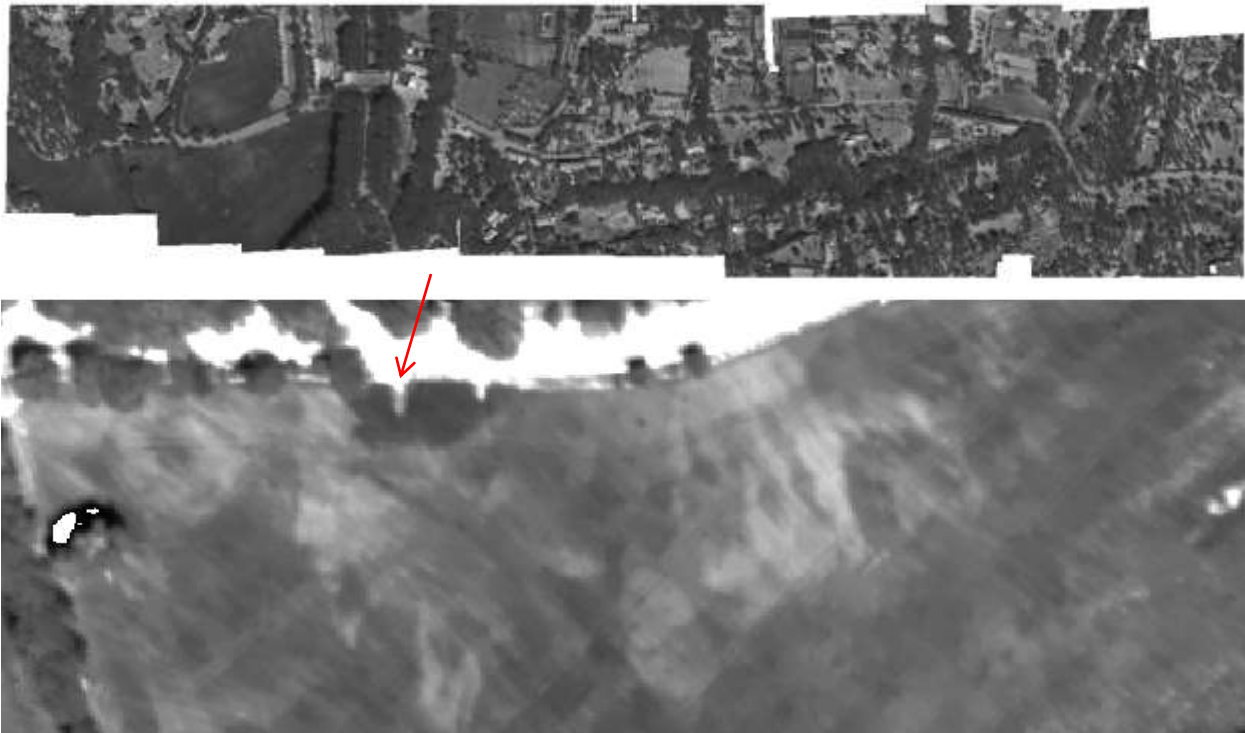


Figure 92 : Le Tholonet (seq. 2). Top: thermal Infrared Image (TIR) as built from the individual 2D images provided by the microbolometer camera. Interpretation of the grey levels: dark or clear pixels correspond to low radiance temperature, resp. higher radiance temperature. Bottom: close-up of the area with a leak (shown with a red arrow).

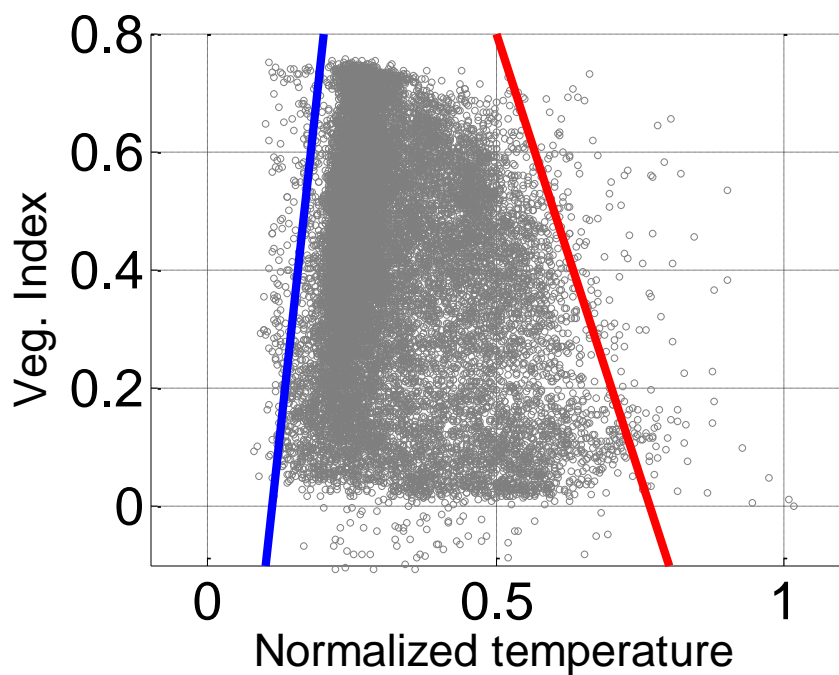


Figure 93 : 2D distribution of normalized temperature and vegetation index (OSAVI). The cold edge (blue) and the warm edge (red) have been positioned so that the trapezoid figure contains essentially all the scatter, except a few outliers.



Figure 94 : Water Index (WI) map as obtained from the scaling of brightness temperature defined by the cold and wet edges in the previous figure. Next figure corresponds to a close-up of the area with the leak.

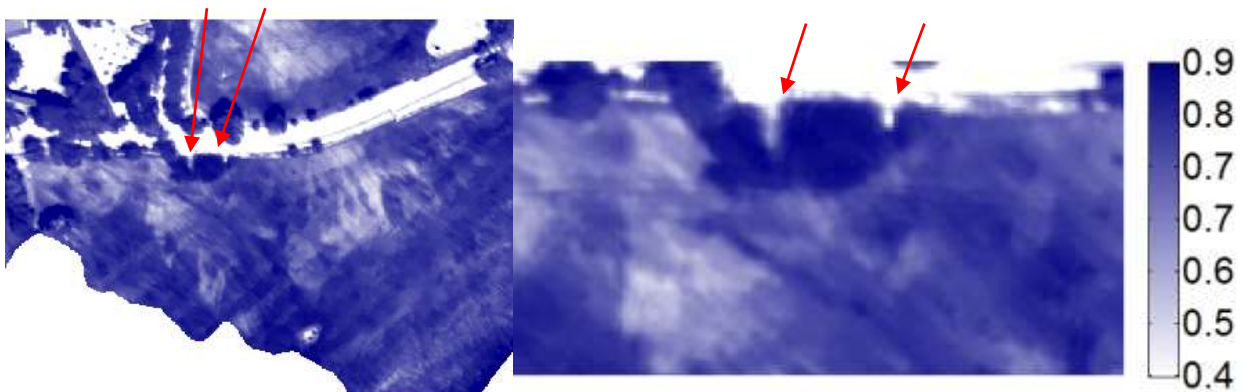
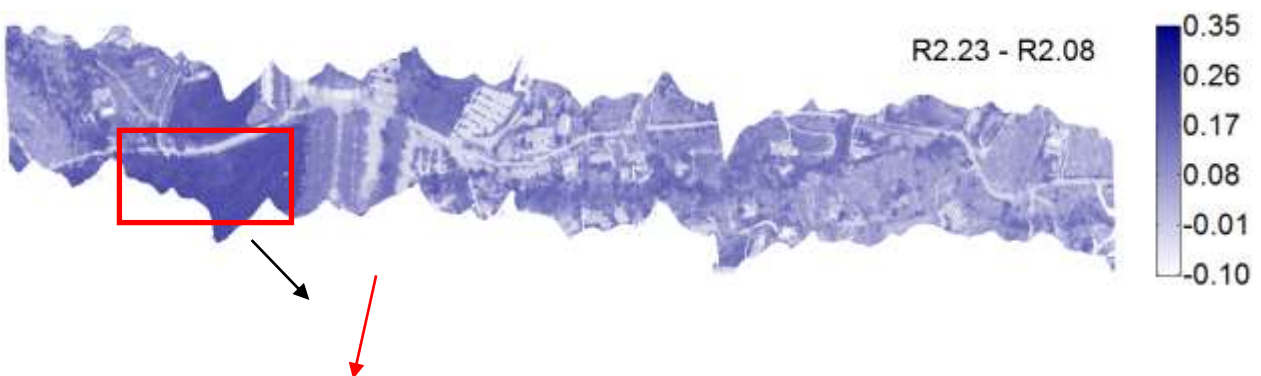


Figure 95 : Two closer views of the area containing a leak. The left arrow indicates the position of a real leak. The right arrow indicates the position of a reference area. The leakage water obviously diffused on both sides of the left trench and reached the reference area.



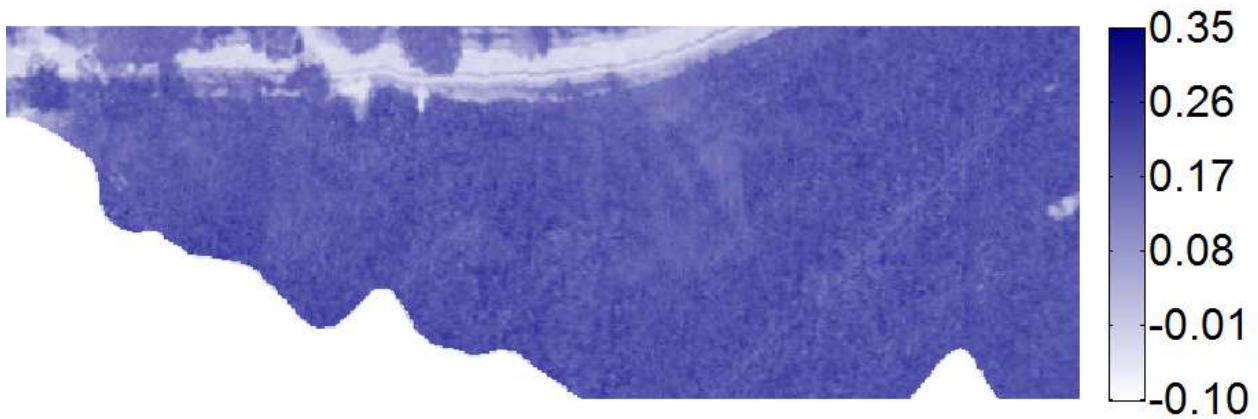


Figure 96 : Le Tholonet (seq. 2). Map of the RNINSOLindex and close up in the leak area. No significant contrast is observed in the vicinity of the leak (shown by an arrow).

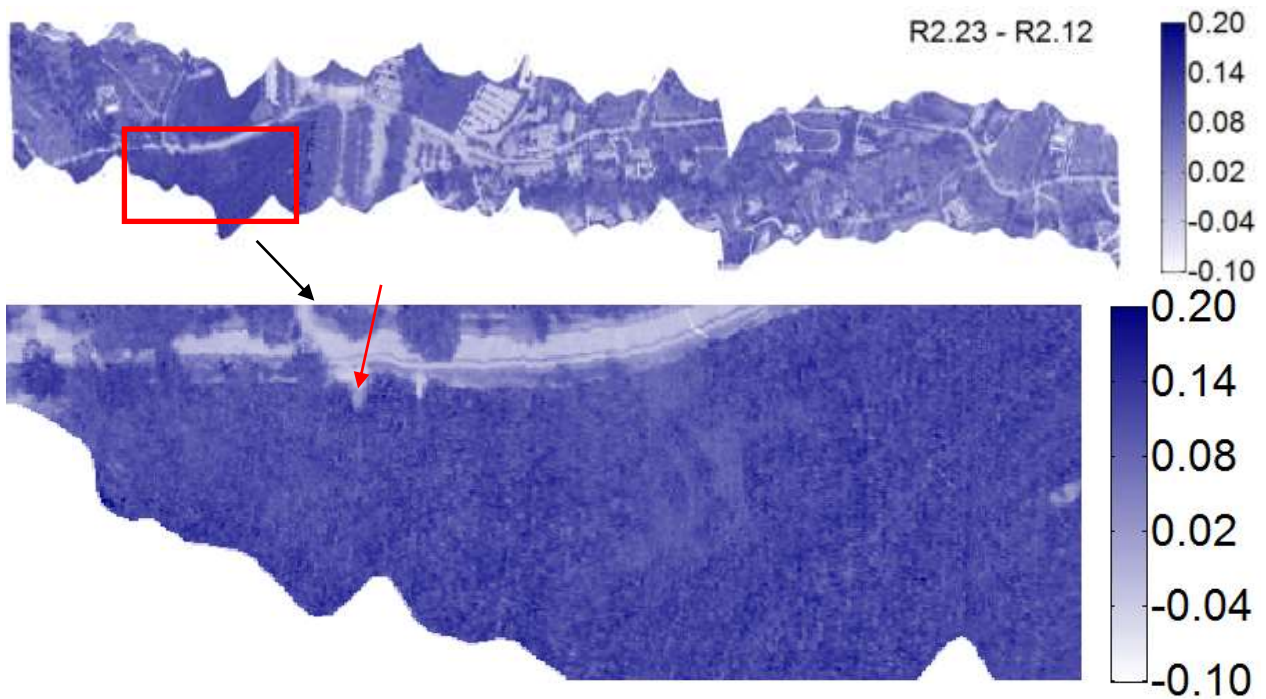
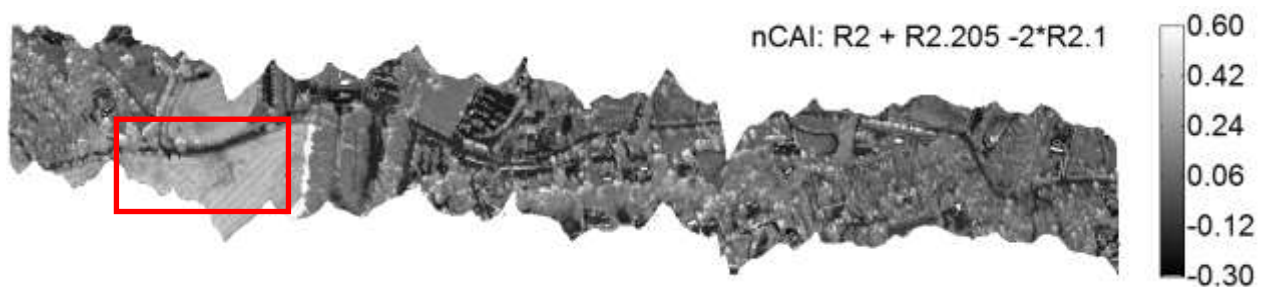


Figure 97 : Le Tholonet (seq. 2). Map of the RNINSONindex and close up in the leak area. No significant contrast is observed in the vicinity of the leak (shown by an arrow).



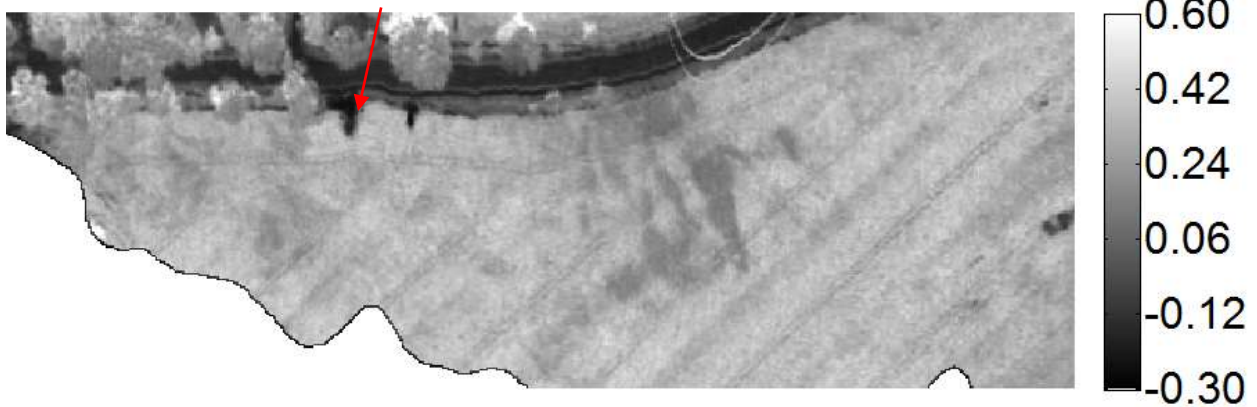


Figure 98 : Le Tholonet (seq. 2). Map of the normalized CAindex and close up in the leak area. No significant contrast is observed in the vicinity of the leak (shown by an arrow).

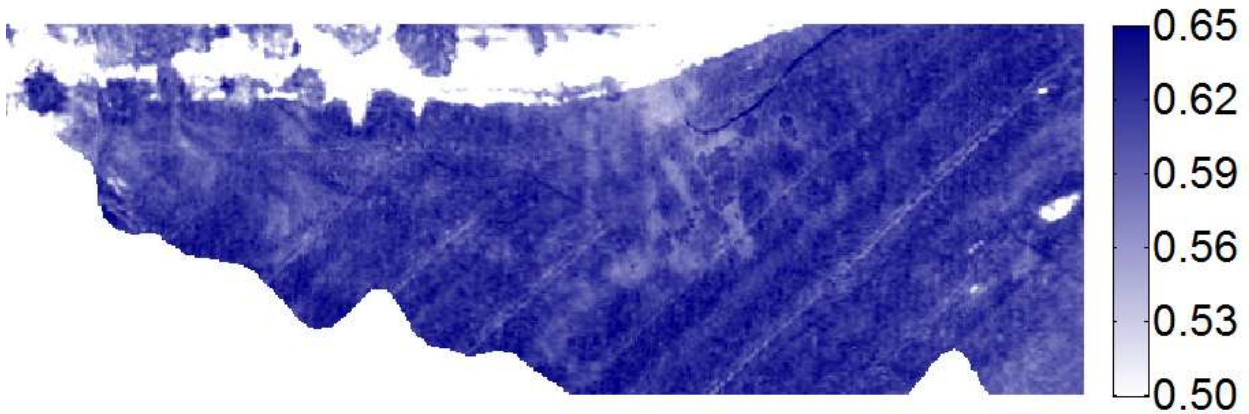


Figure 98b: Le Tholonet (seq. 2). Close up of the map of the normalized NSMIindex.

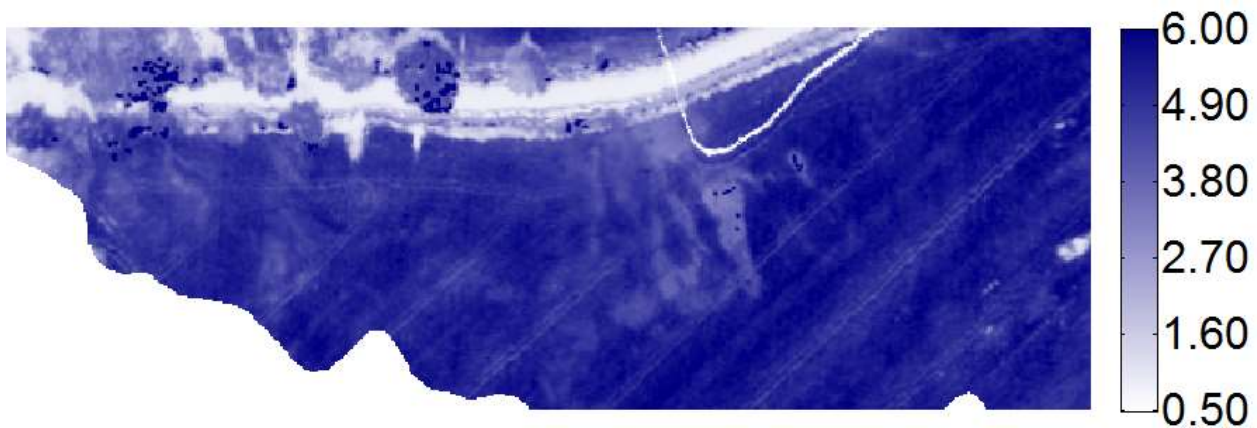


Figure 98c: Le Tholonet (seq. 2). Close up of the map of the normalized WISOIL index.

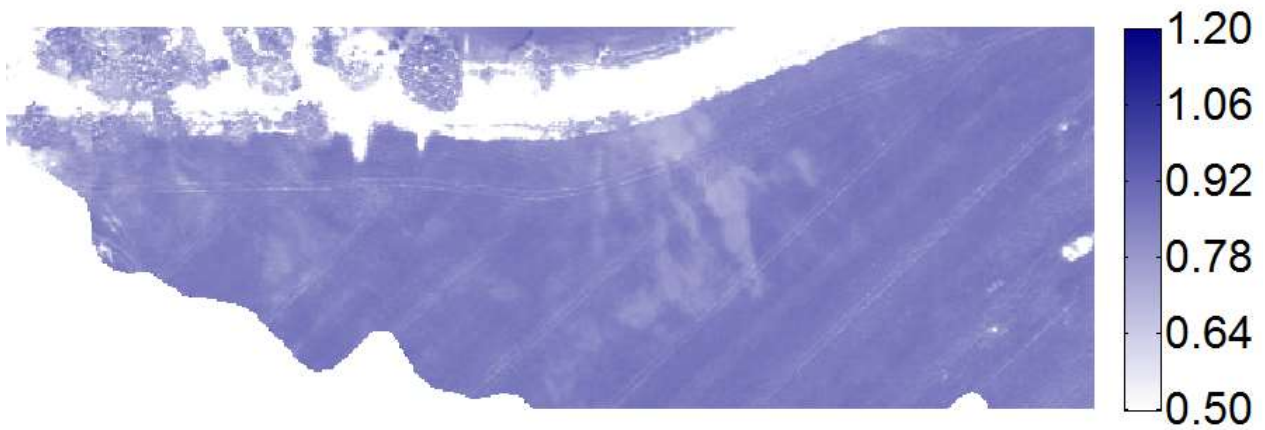


Figure 98d: Le Tholonet (seq. 2). Close up of the map of the normalized NDWI2130 index.

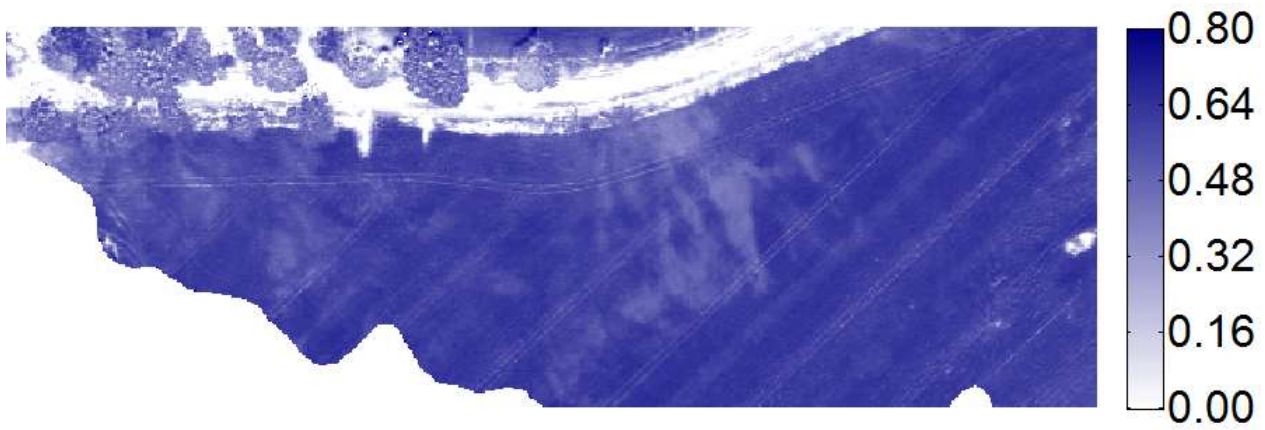


Figure 98e: Le Tholonet (seq. 2). Close up of the map of the normalized NDWI1640 index.

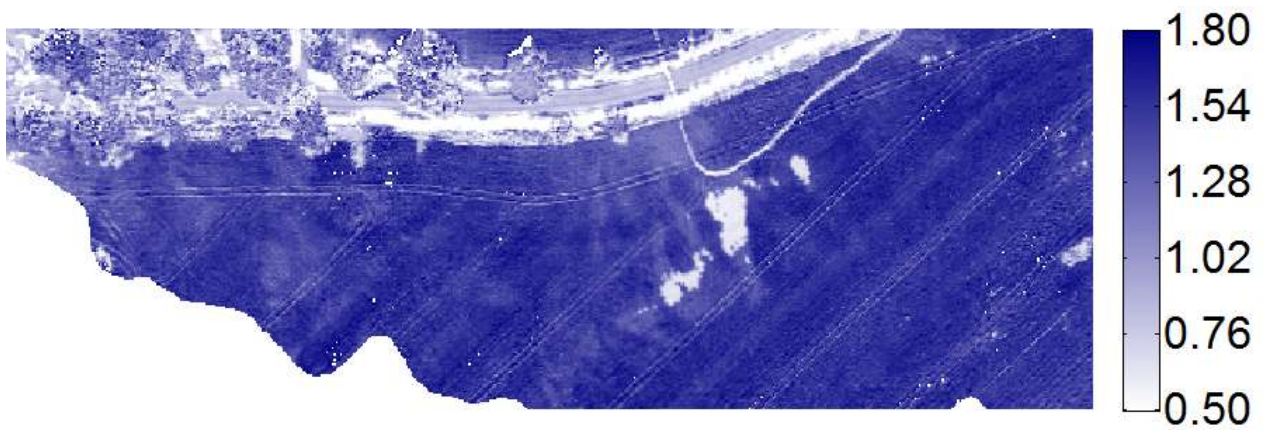


Figure 98f: Le Tholonet (seq. 2). Close up of the map of the SRWI index.

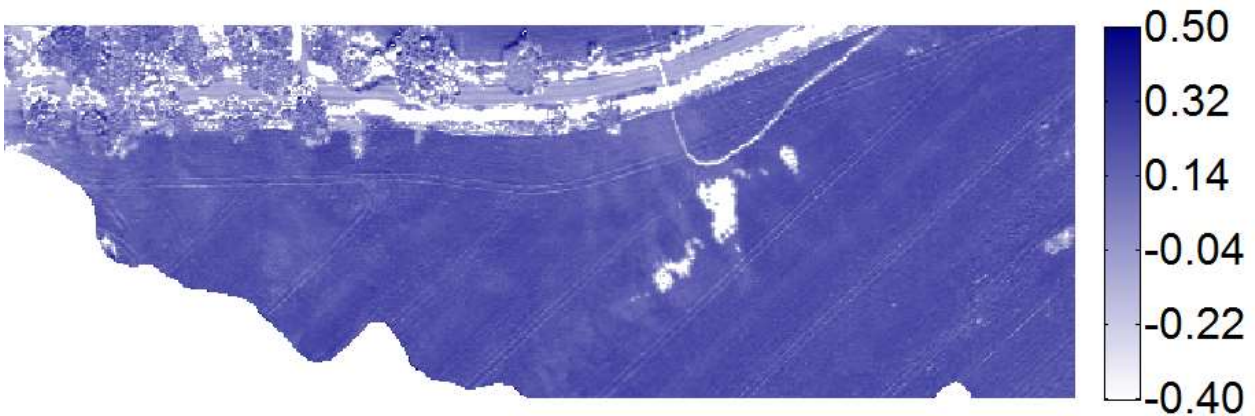


Figure 98g: Le Tholonet (seq. 2). Close up of the map of the NDWI1240 index.

2.5.2 Rians

The spectral image at $0.858\mu\text{m}$ is on fig. 99 (the dark rendering in the middle is due to cloud shadow). The OSAVI map is on fig. 100. The thermal infrared map is on fig. 101. The 2D scatter of OSAVI vs TIR is on fig. 102 and the resulting water index map is on fig. 103. A close up on the leak area is on fig. 104. The line of leaks (shown with a red arrow) appears as a line of increased water index.

The RNINSOL images are on fig. 105. The line of leaks appears as a bright line (low or even negative RNINSOL values) indicated by the arrow. This is in contradiction with the fact that a wet bare soil should show an increased RNINSOL value. Furthermore, this “white” line extends to the north to a wide elliptical shape well beyond the leak area.

The CAI images on fig. 106 are equally negative. The line of leaks shows negative values with high magnitude. This is usually interpreted as dry bare soil.



Figure 99 : Rians (seq. 6). Reflectance at $0.858\mu\text{m}$ (VNIR). Cloud shadows seem to be present in the central part of the image

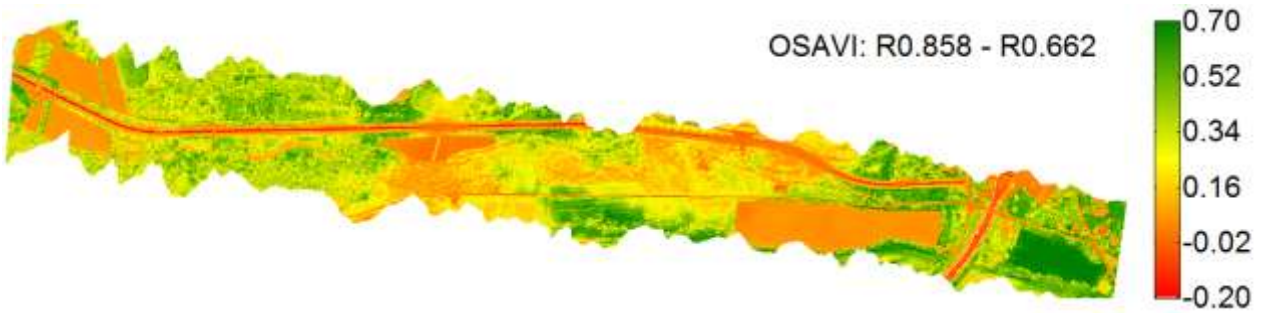


Figure 100 : Rians (seq. 6). Image of the OSAVI vegetation index.



Figure 101 : Rians (seq. 6). Mosaic of Thermal IR images.

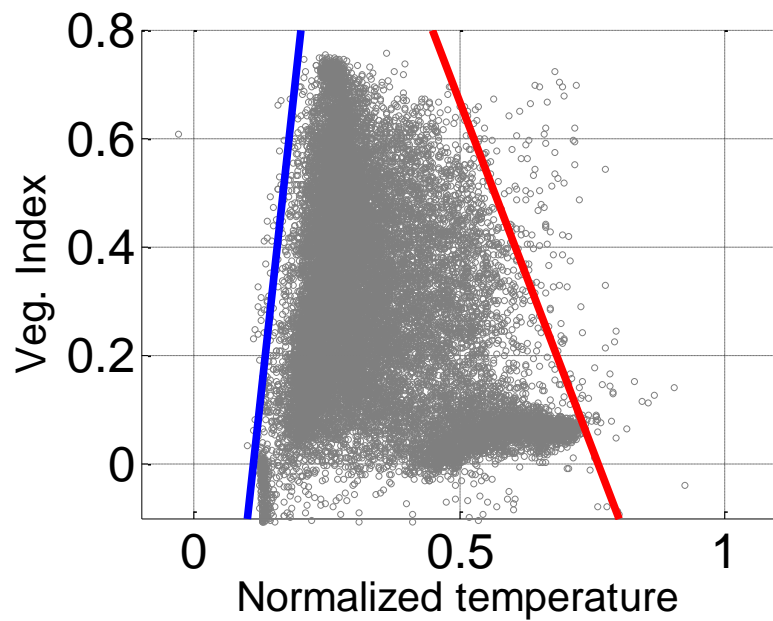


Figure 102 : 2D distribution of the normalized temperature vs. the vegetation index (OSAVI). The cold edge (blue) and the warm edge (red) have been positioned so that the trapezoid figure contains essentially all the scatter, except a few outliers.



Figure 103 : Water Index (WI) map as obtained from the scaling of brightness temperature defined by the cold and wet edges in the previous figure. Next figure corresponds to a close-up of the area with the leak.

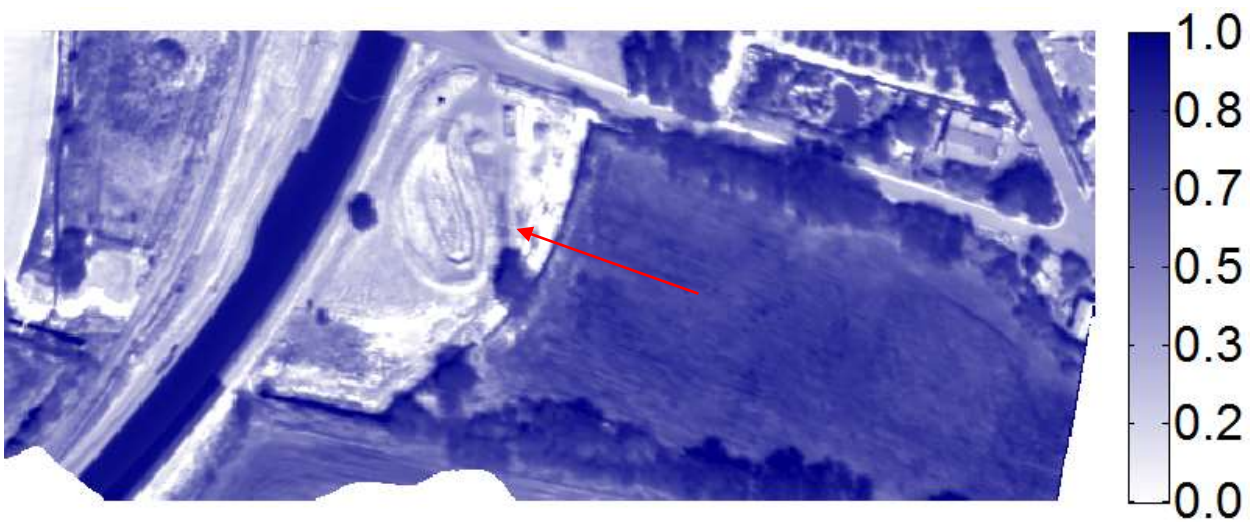
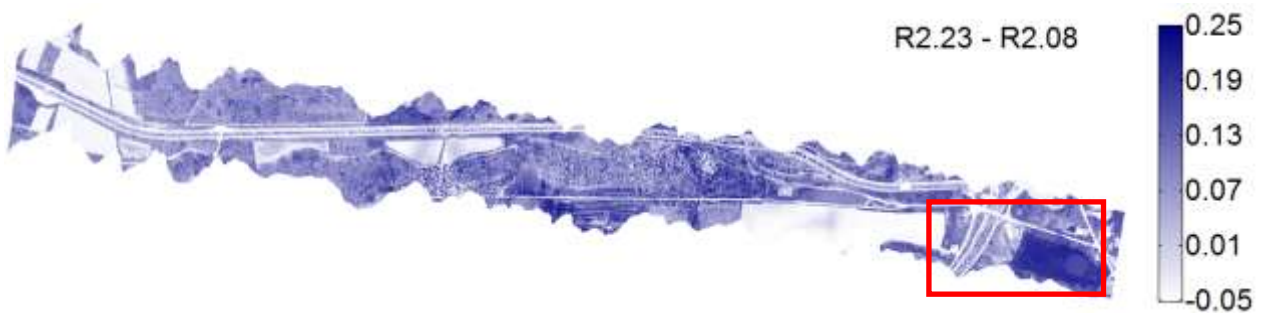


Figure 104 : Close-up of the leak area. The line of leaks (shown with a red arrow) appears as a line of increased water index.



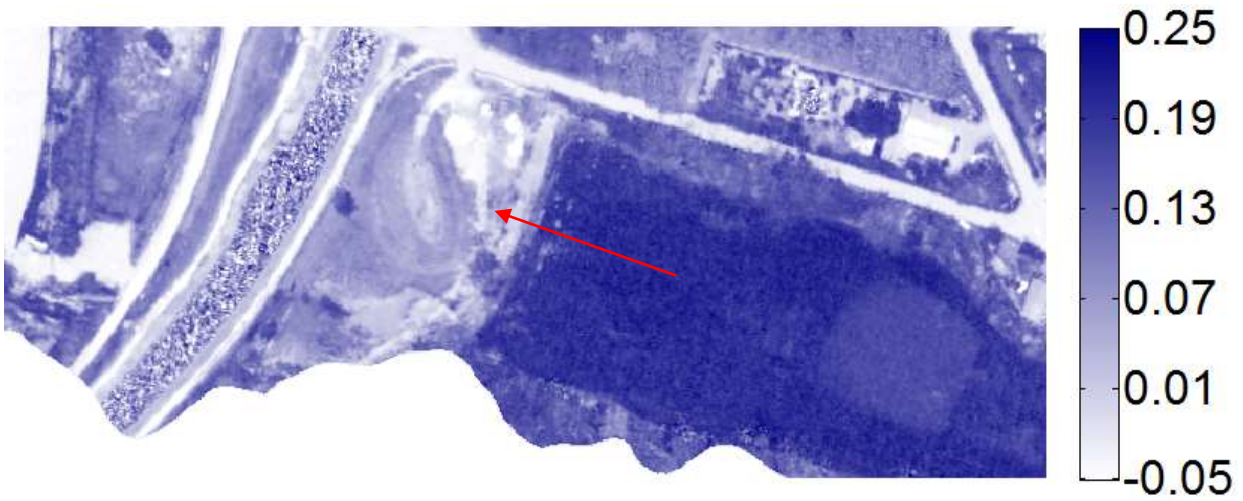


Figure 105 : Rians (seq. 6). RNINSOL index image and close-up of the leak area (bottom). The line of leaks (shown with a red arrow) surprisingly appears as a line of decreased water index.

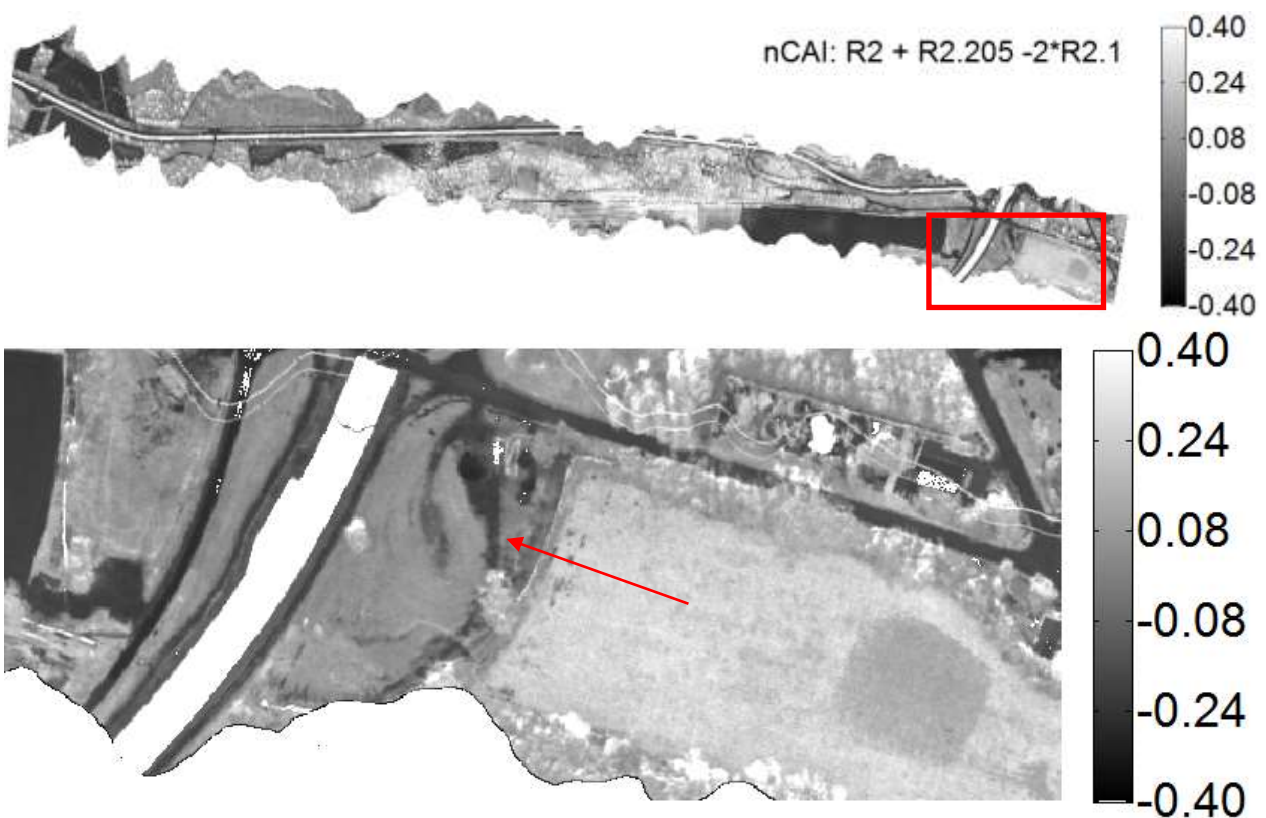


Figure 106 : Rians (seq. 6). CAI index image and close-up of the leak area (bottom). The line of leaks (shown with a red arrow) appears as a line of decreased (negative) CAI index.

2.5.3 Vauvenargues

The OSAVI map is on fig. 107. The thermal infrared map is on fig. 108. The 2D scatter of OSAVI vs TIR is on fig. 109 and the resulting water index map with a close up is on fig. 110. The line of leaks extends from east to west just north from the path. However, no significant

contrast is observed. We can just guess a very small dark patch near the high vegetation bordering the path (as indicated by the arrow).

The RNINSOL images are on fig. 111. The field with the line of leaks appears very uniform without any indication of the presence of water.

The CAI images on fig. 112 are equally negative. In the close up image the texture of the field is richer; however there is no specific contrast for indicating the leakage.

Altogether, the optical data have not provided a clear evidence of the presence of water in this area.

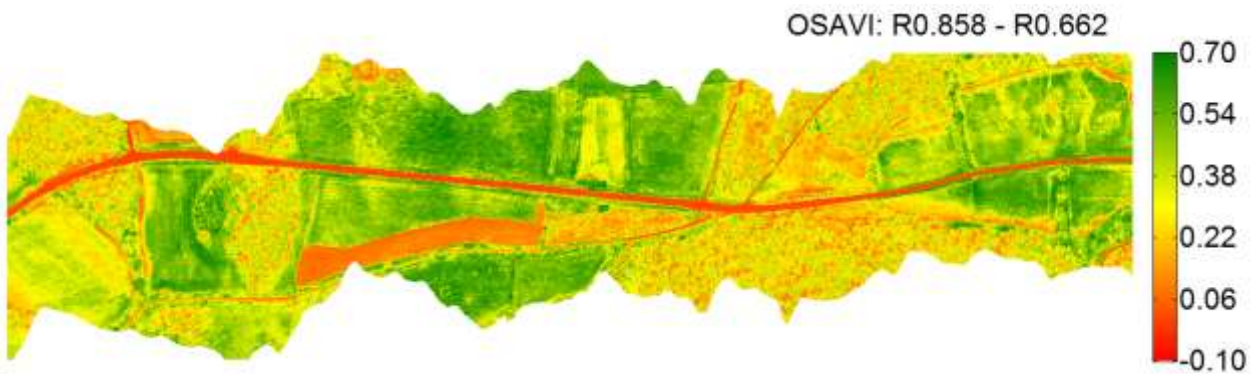


Figure 107 : Vauvenargues (seq. 4). Image of the OSAVI vegetation index.



Figure 108 : Vauvenargues (seq. 4). Mosaic of TIR images.

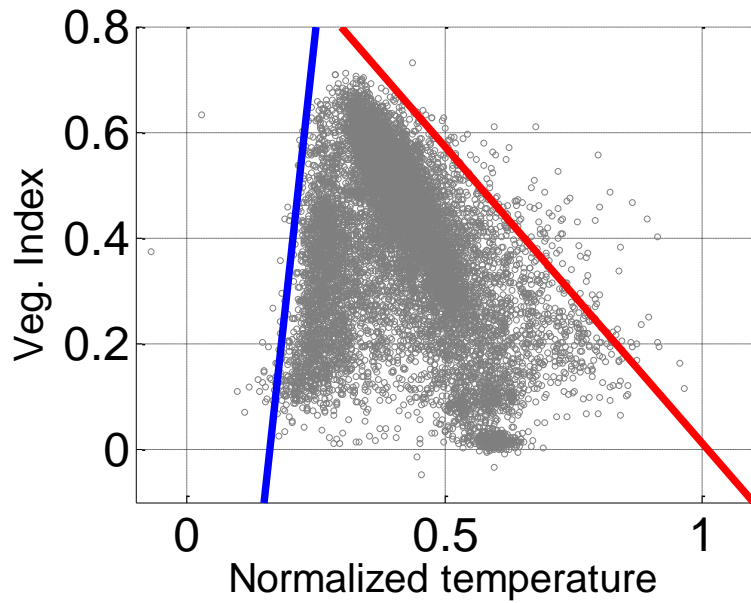


Figure 109 : Trapezoidal distribution of the normalized temperature vs. the vegetation index (OSAVI). The cold edge (blue) and the warm edge (red) have been positioned so that the trapezoid figure contains most of the scatter, except some outliers.

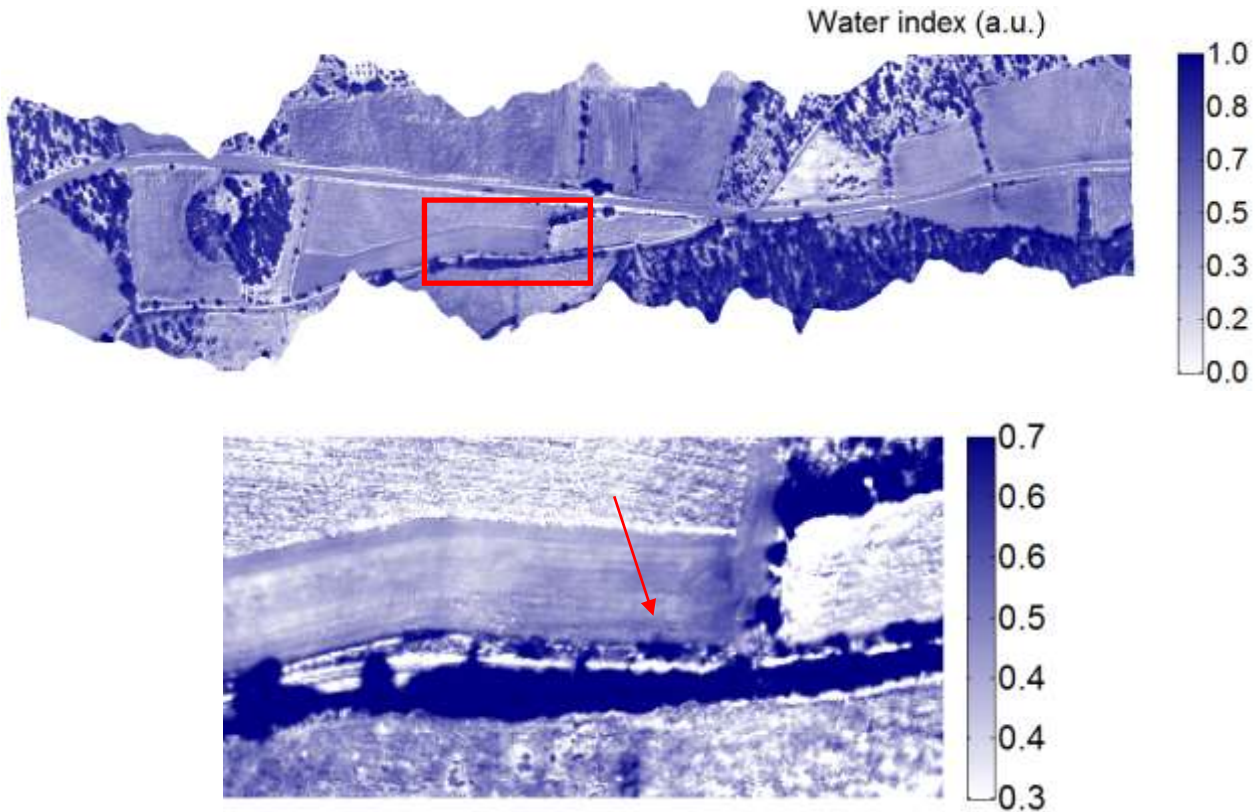


Figure 110 : Water Index (WI) map obtained by the trapezoid method (top) and close-up of the leak area (bottom). No significant contrast is observed along the line of leaks.

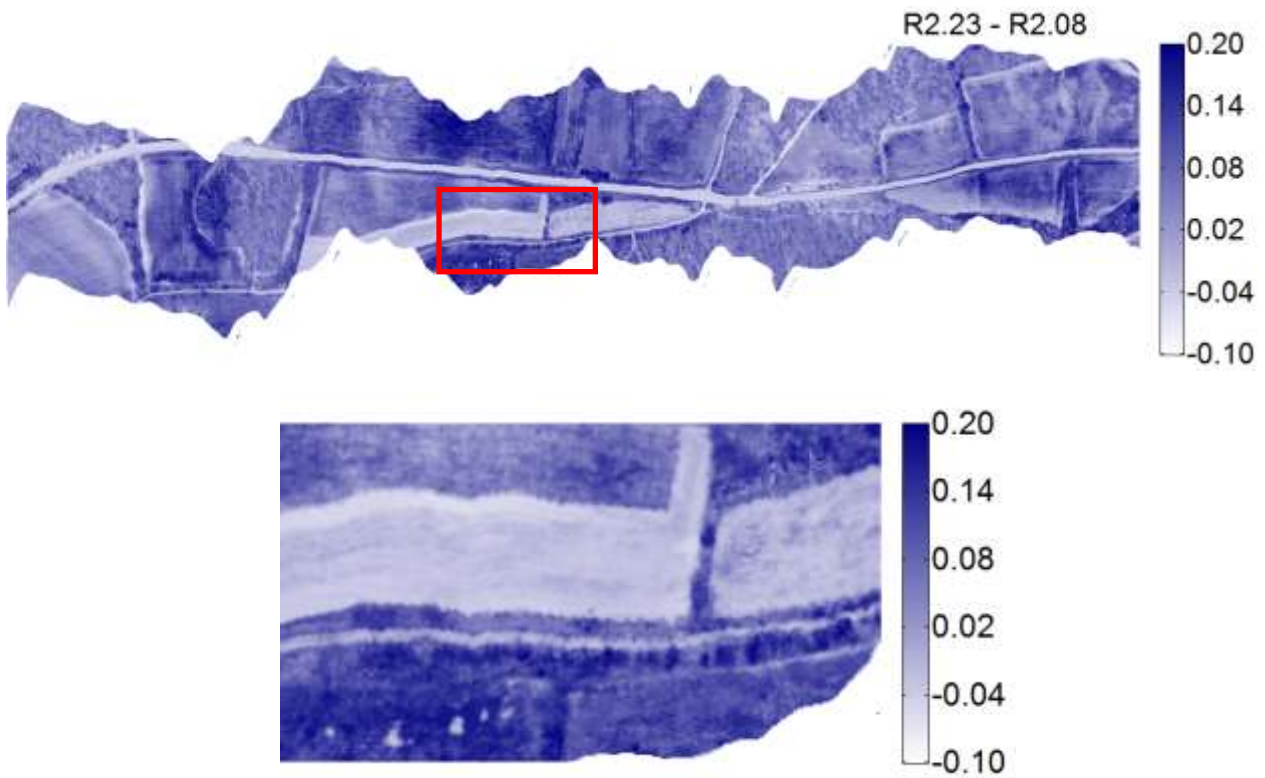


Figure 111 : Vauvenargues (seq. 4). Map of the RNINSOLindex and close up in the leak area. No significant contrast is observed along the line of leaks.

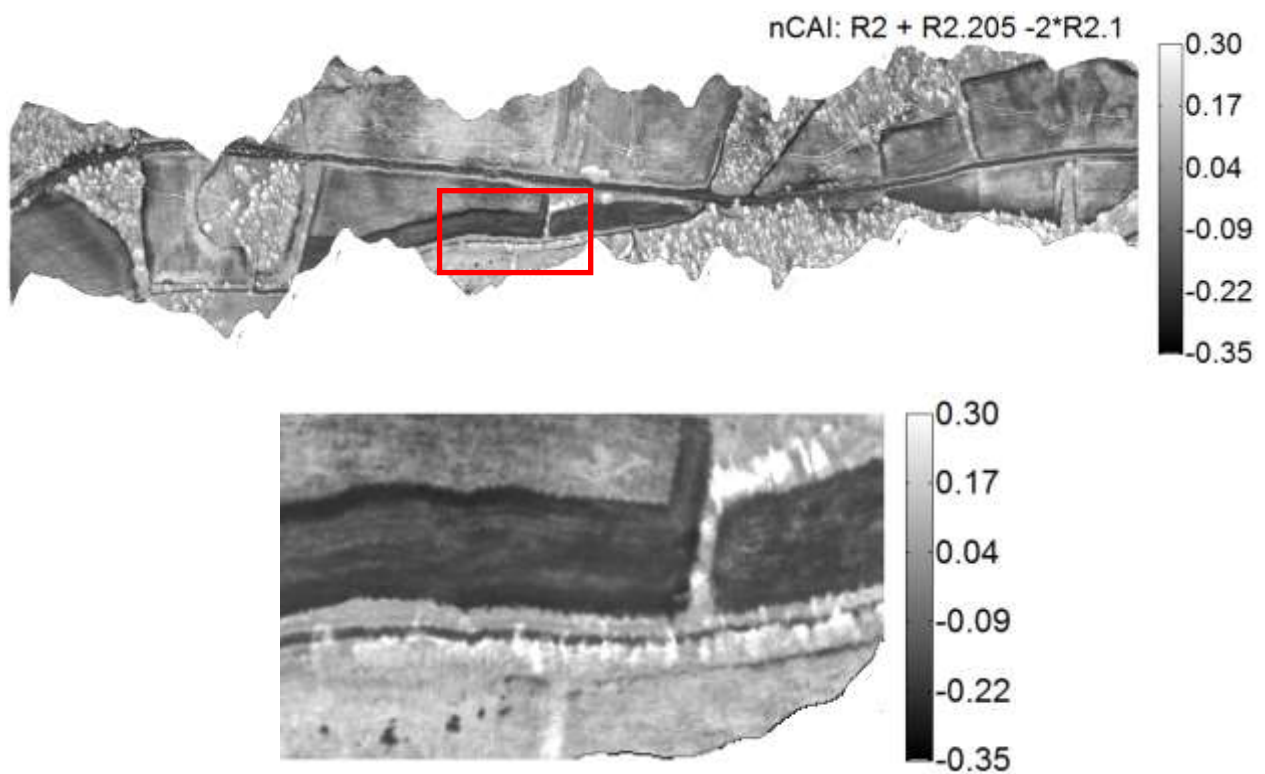


Figure 112 : Vauvenargues (seq. 4). Map of the normalized CAindex and close up in the leak area. No significant contrast is observed along the line of leaks.

2.5.4 Saint-Maximin

The results obtained in the Saint Maximin area during the second campaign are reported on fig. 113-114.

They should be compared with the figures 74-75 obtained during the first campaign.

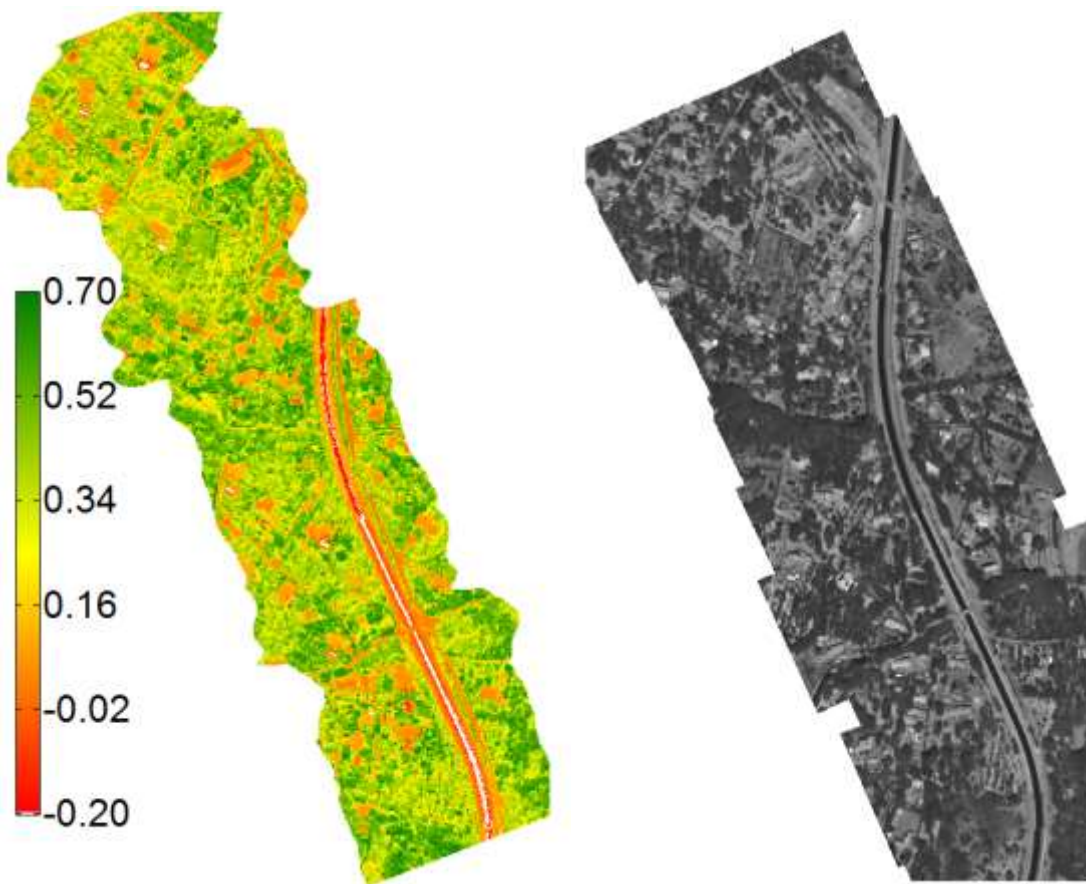


Figure 113 : Saint Maximin. Image of the OSAVI index (left) and mosaic of TIR images.

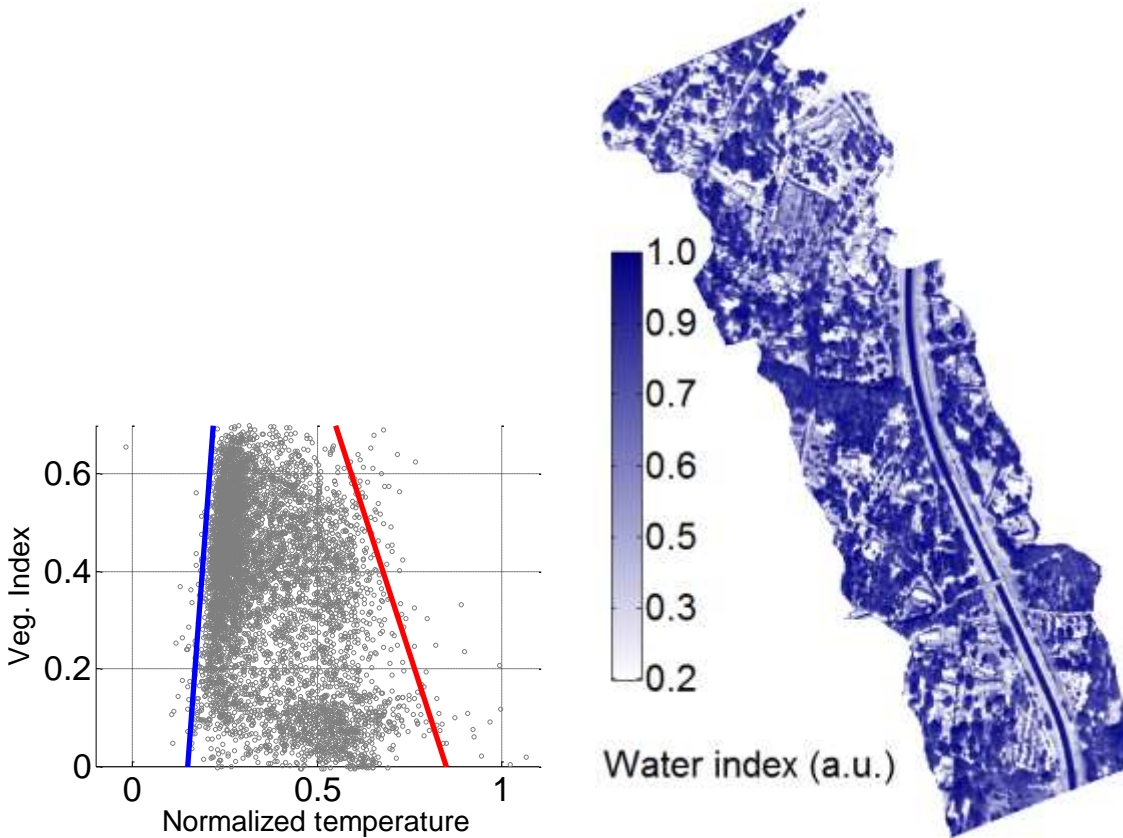


Figure 114 : Saint Maximin. Two-dimensional scatter of OSAVI and TIR values (left) and resulting water index map (right).

2.6 Conclusion

ecttted

A focus was made on trials and areas where known or intentional leaks were present. The processing is summarized in the next table.

		WBI	NDWI 1240	NDWI 1640	NDWI 2130	SRWI	NWI222	WISOIL	NSMI	RNINSON	RNINSOL	CAI	Trapezoid method
WADI1	Esparron	X	X	X	X	X	X	X	X	X	X	X	X
	St Maximin												X
WADI2	Le Tholonet		X	X	X	X	X	X	X	X	X	X	X
	Rians										X	X	X
	Vauvenargues										X	X	X
	St Maximin												X

Table 19: Indices used for WADI1 and WADI2 data processing.

2.7 WADI 3 Campaign

The last airborne measurements of July (WADI-3) have been carried out too close to the deadline of the report D3.1 to allow using the date in the pre-processed images database.

The data processing methods will be applied later and the outcome will be used to prepare the validation cases for the WP4 (Task 4.2.3).

2.8 Optimized detection wavelengths determination

The wavelengths that were considered during the two campaigns for getting the different water indices are listed in the following table.

													Trapezoid method	
	(μm)	WBI	NDWI 1240	NDWI 1640	NDWI 2130	SRWI	NWI222	WISOIL	NSMI	RNINSON	RNINSOL	CAI	OSAVI	TIR
VNIR	0.662												X	
	0.858		X	X	X	X							X	
	0.9	X												
	0.97	X												
SWIR	1.24		X			X								
	1.3							X						
	1.45							X						
	1.64			X										
	1.8								X					
	2						X					X		
	2.08										X			
	2.1											X		
	2.12								X	X				
	2.13					X								
	2.205						X					X		
2.23									X	X				
TIR	8-12													X

Table 20: Wavelengths considered during WADI1 and WADI2 campaigns

Depending on the possibility of discriminating two fields having presumably a low and a high moisture and on the possibility of detecting artificial leaks, we have filled the following table. Different colours are used to indicate the respective performance: green for good detection/discrimination, orange for medium/low S/N, red for a S/N lower than 2 or for no detection. Magenta is used for reporting detection with a difficult interpretation (namely an unexpected signal change of the contrast).

													Trapezoid method	
		WBI	NDWI 1240	NDWI 1640	NDWI 2130	SRWI	NWI222	WISOIL	NSMI	RNINSON	RNINSOL	CAI	OSAVI	TIR
WADI1	Esparron	X	X	X	X	X	X	X	X	X	X	X	X	X
	St Maximin													X
WADI2	Le Tholonet		X	X	X	X	X	X	X	X	X	X	X	X
	Rians										X	X	X	X
	Vauvenargues										X	X	X	X
	St Maximin													X

Table 21: Performance (S/N) obtained with the different indices.

Based on these results we recommend focusing on a combined TIR-VNIR remote sensing followed by a signal processing according to the triangle/trapezoid method.

An infrared camera in the thermal wavelength (8-12 μm) should be preferred. Depending on the flight speed, a slow microbolometer camera could be sufficient. Otherwise, one should prefer a faster cooled HgCdTe camera.

To process the vegetation index necessary for the triangle/trapezoid method (NDVI, or preferably OSAVI), one wavelength on each side of the red edge is necessary. The choice is not very strict: typically between 0.65 μm and 0.675 μm for the first one and between 0.79 μm and 0.87 μm for the second one.

2.9 Measurement strategy

The measurement strategy results from several requirements:

- The nature of the effect observed for the water leak detection (see 1.15)
- The surveillance constraints and requirements from water provider company
- The data processing method needs
- Complementary use of aircraft and UAV platforms

2.9.1 The nature of the effect observed

The nature of the effect observed for the water leak detection can be determined by using a measurement strategy.

2.9.1.1 The inertial thermal effect use for water leak detection

The IR emission of the soil during a fast change of the temperature enables to detect an anomalous emission related to presence of a moist underground volume. The detection of this "thermal inertial effect" requires airborne measurements at several times of the day (sunrise, sunset or midday).

2.9.1.2 The anomalous vegetation growth or nature of the vegetation

An anomalous vegetation growth or the detection of a change in the type of vegetation require a multi-temporal surveillance service at different times or seasons. Furthermore, the change of vegetation nature can require a comparison with a reference scene.

2.9.2 The surveillance constraints and requirements from water provider

A requirement to observe the main water network and the secondary at the same time has been expressed by a water provider partner. The feasibility will be analyzed. Three methods can be studied: an observation using a large field of view, several measurement flights at different altitudes, a complementary use of aircraft and UAV platforms.

The surveillance of a specific area after repairing can require temporal observation in order to calibrate the recovery time.

In some case the recording of a reference scene at a specific time/season will be necessary.

2.9.3 Data processing requirements

The efficient detection of anomalous effect on an image requires the presence of the anomalous on several pixels of the image. The field of the view of the instrument must be adapted but also the altitude of the flight. In fact the use of a better spatial resolution than the end-user need can be required.

The use of the high powerful triangular data processing method requires a set of different environmental conditions measurements. This can be obtained by the use of a large field of the view around the surveillance area but also by the main of several flights at different altitudes.

2.9.4 Complementary use of aircraft and UAV platform

All parameters such as the nature of the observed effects, the end user and data processing needs will contribute to define the strategy of complementary use of two aircraft/UAV platforms. The airborne prototype configuration and the flight constraints will be also take into account.

Water leak detection using anomalous effects

Soil without vegetation

- Darkening effect
- Soil surface modified by water evaporation
- Temperature surface
- Behaviour of soil thermal inertia

Soil with vegetation added effects

- Vegetation growth
- Change of vegetation
- Scale observation effect



darkening and soil surface effects



Undirect effect:
thermal inertia

All effects are detectable using remote sensing hyper/multi-spectral cameras coupled with IR cameras

The effects observed define

- the optimal wavelength detection
- the measurement strategy (multitemporal, reference scene,...)
- The data processing method for inverse process (triangular method or/and spectral reflectance)

Figure 115 : Water leak detection using anomalous effects

3 Multispectral and IR cameras selection

Water leaks induce soil moisture and /or anomalous vegetation growth which affect the typical physical effects in terms of darkening surface, surface temperature, thermal inertial soil behaviour, and vegetation characterization. The associated physical parameters (i.e. reflectance and temperature) can be extracted from the images acquired in particular spectral ranges. The temperature is measured in the infrared (IR) spectral range. The other parameters require measurements in the VNIR and SWIR spectral ranges.

The airborne measurement campaigns using hyperspectral/IR BUSARD platform have been used as a basis to determine the optimized detection wavelengths. The development of WADI's innovative concept (which is based on the use of the existing multi-spectral/IR cameras to replace complex and expensive hyperspectral system) requires selecting the most suitable, existing (off-the-shelf) cameras operating at the required wavelengths. The most promising cameras will be selected and purchased taking into account all relevant requirements of the application.

This section consists of two main parts. In the first one, the requirements for the cameras are identified. Building on this set of requirements, recommendations for the optimal selection of an in-flight multi-spectral/IR cameras and IMU payload are exposed in the second part.

3.1 Identification of the requirements for the airborne multi-spectral/IR cameras

In order to give recommendations for the optimal selection of a flying multi-spectral/IR cameras payload, system requirements must be defined beforehand. These points that will constrain the architecture of the system will be defined based on requirements elaborated in WP2, on-board platform constraints, and other relevant considerations (e.g. the easiness of use, best value for money, best time to deliver...).

Apart from the compactness needed in airborne operations, the performance requirements for the airborne cameras are rather similar to those of ground cameras. In general, the more sensitive, selective, robust and reproducible the cameras are the better. Low frequency and smoothness of maintenance as well as low costs would also make sensors attractive. However, there are certain features inherent to the operation of airborne sensors that need to be recognized.

We will deliver sort of overall requirements collection consisting of some high level functional and non-functional requirements. These requirements are based on ONERA's know-how. Priorities of these requirements were proposed by ONERA:

- Essential (E): the product is not acceptable unless these requirements are satisfied
- Conditional (C): would enhance the product, but the product is not unacceptable if absent



Description of selected requirements can be found below in four groups according to airborne cameras architecture:

- General
- Sensors
- Control/Command and data acquisition
- Airborne platform

This set of high level qualitative requirements is:

- Consistent - requirements do not contradict any other requirements.
- Unambiguous - requirements are concisely stated without recourse to technical jargon, or other acronyms. It is subject to one and only one interpretation.
- Complete - requirements are fully stated in one place with no missing information.
- Testable - these are requirements that have been broken down to a level where they are precise, non-ambiguous and no longer divisible into lower level.

The following conventions have been adopted for this document:

- Requirement numbering: [R_xx] is a unique identifier, in order to make each requirement traceable throughout the development process.
- Functional requirements: the essential subject matter of the product. They describe what the product has to do or what processing actions it is to take.
- Non-functional requirements, the properties that the functions must have, such as performance and usability.

3.1.1 Requirements

3.1.1.1 Functional requirements

3.1.1.1.1 General

[R_01] System should provide an easy adaptation to area size (E).

One should take into account that the size of monitoring areas might differ and different surveillance strategy might be necessary. Adaptation to area size features should consider also an optimal number of system elements that should be used on given area.

3.1.1.1.2 Sensors

Characteristics of cameras shall correspond to those expected for the following scenario:

- Scenario 1: The aircraft flies with a speed $V = 120$ KTS (220 km/h) with respect to the ground while camera is pointing the nadir. The flying altitude is taken as 800 ft AGL (250 m from ground level) and the camera is configured to get a ground sampling distance of 1 m.

[R_02] Cameras shall meet the measurement requirements at the set of optimized detection wavelengths determined in Subtask 3.1.2 (E)



[R_03] The system should provide the precise angular positioning of line of sight for each camera [E].

The measurement results should be located on a map the GPS-position. Therefore, the roll, pitch and heading of the cameras must be known.

[R_04] Blurring of the image occurs as a result of motion of the aircraft during the time Δt during which the camera shutter is open. The image blur induced by the principal movement of the airplane (which is, in first order approximation, rectilinear and uniform), should not exceed 1/5 of a pixel (C).

Under conditions of scenario 1, exposure (or integration) time Δt should not exceed 3 ms.

[R_05] Aircraft acceleration and turn also induce image blur. Therefore, angular motion should be minimized by gyro stabilizing mounts (C).

3.1.1.1.3 Control/Command and data acquisition

[R_06] UAV operator shall be able to control the cameras (E).

[R_07] In order to adapt to environment changes and electronic drifts and to ensure Image uniformity and accurate radiometric calibration, the infrared camera shall be equipped with a non-uniformity correction (NUC) and radiometric calibration function (E).

[R_08] The IR camera software will allow manual control of non-uniformity correction (E).

[R_09] Data from the cameras and environment data must be recorded for post analysis (E).

[R_10] The recording devices must be able to record data at the rates specified in each instrument and support at least up to 2 hours of flight time (C).

[R_11] Operator shall be able to activate/terminate data recording and monitor the cameras data in real-time (C).

[R_12] All onboard instruments shall be time synchronized when measurement is activated or terminated by operator (E).

[R_13] The level of automation and operator control must be such that the system is capable of monitoring the progress of the mission and assessing the quality of the data to reduce the needed expertise level of the operator, on in the case of a UAV application, operate autonomously (C).

[R_14] System should send out a warning whenever there is an event that the end-user should be aware of (identification of a possible water leakage) (C).

[R_15] The data collected during a survey will be tagged with a GPS timestamp with the end result being a geographic position (E).

[R_16] Cameras software shall be compatible with all major operating systems such as Windows, Mac OS X or Linux (E).



[R_17] IR camera software shall provide real-time images in absolute radiometric temperature format (E).

3.1.1.1.4 Airborne platform

[R_18] The airborne multispectral/IR cameras should be able to operate on manned and unmanned aircrafts (C).

3.1.1.2 Operational requirements

3.1.1.2.1 Payload readiness

[R_19] The cameras shall be ready for operation in less than 10 minutes after applying power (C).

3.1.1.3 Interface requirements

[R_20] Volume, height, weight and centre of gravity location of the cameras shall be such that they would fit into Air Marine Tecnam P 2006 aircraft (E) and NTGS UAV (C).

[R_21] The total power budget of the payload shall be within the available power provided by the aircraft or UAV generator (E).

[R_22] The cameras shall interface with the aircraft or UAV avionics in a manner which is easy to install and maintain (E).

[R_23] Cameras shall be connected to acquisition system via standard video interfaces (E).

3.1.2 Constraints

[R_24] Environmental conditions which the sensors shall be capable of sustaining (operated and non-operated) shall be as follows (C):

- Operating temperature range: from -20°C to +40°C
- Relative humidity up to 95% (without condensation)
- Altitude (pressure): till 1000 m
- Storage temperature range: from -40°C to +40°C

[R_25] Each camera shall be contained in a single lightweight compact unit, which includes all the electronics necessary to operate the sensor (E).

[R_26] The cameras and IMU shall be rigidly fixed to each other (E).

[R_27] Onboard sensors shall be able to withstand the flight environment and vibration to carry out measurement (E).

[R_28] The cameras shall be robust and resilient to vibrations and shocks thus enabling deployment on a mobile platform (E).

In order to isolate the cameras from direct contact with the airframe, decreasing the mechanical noise (vibration) and shocks to the cameras components (depending on the



vibration/angular velocity inputs levels and characteristics), the cameras payload might be required to be mounted on aircraft or UAV airframe by means of shock absorbers.

The necessity for using external shock mount will have to be evaluated based on measured/spec. environmental inputs relative to required performances.

[R_29] The cameras shall be protected from dust and water droplets (E).

[R_30] Moisture and condensation should be avoided during operation and in stand-by mode as much as possible (E).

[R_31] The cameras shall function in electromagnetic compatibility with the external environment during all flight profiles and modes of operation. In particular, grounding and shielding design of the cameras shall be established to control EMC (E).

[R_32] The cameras should be capable of operating in an unpressurized, cold environment (C).

3.2 Recommendations for the optimal selection of a flying multi-spectral/IR cameras and IMU payload

3.2.1 IR camera

There are two classes of thermal imaging camera systems available on the market today: cooled and uncooled systems:

- Cooled infrared cameras, having an imaging sensor that is integrated with a cryocooler, allowing a better sensitivity (thermal contrast). The lower the thermal contrast (NETD), the easier it is to detect objects against a background that may not be much colder or hotter than the object. Cooled cameras have adjustable integration times and make use of a global shutter. This means that they will read out all pixels at the same time, as opposed to reading them out line by line, which is the case with uncooled cameras. This allows cooled cameras to capture images and take measurements on moving objects without image blurring.
- Uncooled infrared cameras (microbolometers), in which the imaging sensor does not require cryogenic cooling, are generally much less expensive than cooled infrared cameras, have fewer moving parts and tend to have much longer service lives than cooled cameras under similar operating conditions. They have smaller sensitivity characteristics than cooled cameras and their response time is not adjustable.

Potential IR cameras (cooled and uncooled) candidates are listed in Table 24(see Annex 1).

Due to their better sensitivity and faster response time (factor limiting image blurring), cooled LWIR cameras are preferred.

3.2.2 Multispectral VNIR/SWIR camera

Imaging spectrometers collect data over three dimensions—two spatial (x, y) and one spectral (λ)—so that the complete (x, y, λ) dataset is typically referred to as a datacube. The most common method used to categorize the various types of imaging spectrometers is by the portion of the datacube collected in single detector readout [3]. The main characteristics of multispectral cameras acquisition modes are summarized below:

Line-scanning (push-broom)	<ul style="list-style-type: none"> • High spatial resolution • Requires motion to occur
Multi-cameras	<ul style="list-style-type: none"> • Simultaneous capture of several discrete spectral bands (up to 6) • Rugged design with no moving parts • Up to 6 optical paths
Sequential multispectral	<ul style="list-style-type: none"> • Interchangeable standard or custom spectral filters • Non simultaneous acquisition of multispectral information from a scene (rotating filter wheel)
Snapshot mosaic	<ul style="list-style-type: none"> • 4×4 or 5×5 mosaic patterns repeated continuously on the sensor surface • Snapshot multispectral imager eliminates artifacts caused by motions in flight (global shutters expose the entire image at the same instant)

Table 22 : Pros and cons of multispectral acquisition modes.

Potential VNIR/SWIR multispectral sensor candidates are listed in Tables 25 and 26 (see Annex 2).

In order to facilitate inter-band data registration, multispectral cameras with simultaneous acquisition of multispectral information from the scene are preferred.

3.2.3 Inertial Measurement Unit (IMU) and GPS

These components give the attitude of the aircraft and its position. Two categories of IMU are commercially available today:

- low cost and low performance IMU which provides only information on rotation velocity and acceleration based on gyroscopes and accelerometers sensors,
- high performance IMU, equipped with a directional gyroscope hybridized with a global positioning system (GPS).

In order to give recommendations for this type of equipment, even if the choice will depend on constraints linked to the airborne platform (manned or unmanned: compactness, weight, electric consumption...), it is possible to give technical characteristics for these two classes of IMUs. We have selected three models proposed by two different suppliers and the main characteristics are exposed in table 23:

Model	Systron MMQ 50	Systron C-MIGITS III	iMAR iTrace 200
			
Type	IMU Gyroscope & accelerometer / 3 axis	IMU / GPS	IMU/GPS
size	5x5x6cm	9x9x14cm	15x15x10cm
Weight	227 g	1.1 kg	2.42 kg
Accuracy	0.3°/√h 500µg/√h - - -	0.035°/√h 60µg/√h 0.06° pitch/roll 0.09° heading 3.9 m	0.1°/√h 50µg/√h 0.01° pitch/roll 0.025° heading 0.1 m
Advantages	Compactness Weight RS 232 interface Power consumption <5W	« All in one » solution Real time Attitude RS 232 interface Compactness Angular accuracy	« All in one » solution Real time Attitude USB / RS232 / CAN interface Angular accuracy
Disadvantages	No integrated GPS Attitude, to be calculated	Low accuracy of position	size weight

Table 23: Characteristics of state-of-the-art IMUs.

The best technical and economic trade-off between these three models seems to be the class of Systron C-MIGITS III which enables to fulfill the main requirements for the airborne platform (TECNAM P2006 of Air Marine).

For the UAV platform, more compact and cheaper solutions are proposed on the RPAS market and the partners involved in the integration of the WADI onboard system should select the best sensors for this kind of platform.



4 Conclusions

This document is focused on the determination of the optimal wavelengths for water leakage detection and determines the characteristics of cameras adapted for the two aerial platforms (manned or unmanned) used for operational environment demonstrations over the two pilot sites (WP5 and WP6). A camera selection has been proposed for the aircraft platform.

The most significant findings can be outlined as follow:

- The selection of sites of water transportation infrastructures for the WP3 demonstrations has been decided in close collaboration with SCP involved in this WP. Choice criteria have been defined to fulfill the main requirements of the WADI project (rural areas, buried pipes, canals, concrete/steel/ conduits, pressurized/gravity flow in pipes...). Nevertheless, the aim of the task T3.1 was to overflow areas with a high potential of soil moisture due to controlled or uncontrolled water leaks in order to collect relevant images for the data processing. The first airborne tests (February) have been achieved over zones without controlled water leaks and on the basis of 2015 water balance, SCP had identified several sites near BUSARD airbase with low efficiency ratio. For the second part of the airborne tests, other criteria for the selection of interest areas have been proposed and selected for building artificial water leaks; these special facilities for the BUSARD campaign have resulted in high quality optical remote sensing correlated with ground truth measurement.
- The trials were conducted over 6 months, between February and July 2017, with ONERA's aerial platform BUSARD instrumented with two hyperspectral cameras and one uncooled infrared camera coupled with ground truth measurement. The lines of flights and scenarios (aircraft altitude, spatial resolution, speed...) decided during this campaign have led to build up a rich and unique database (VNIR, SWIR, TIR) with different weather conditions (winter, spring and summer seasons), type of soil and vegetation and rate of water leaks. The main difficulties experienced during this task were linked to availability of Hyperspectral payload, bad weather conditions (wind, rain, clouds cover,...) and flight clearance near protected areas (civil airport, military and restricted zone,...).
- The hyperspectral and IR data have been pre-processed (geometrics and radiometric correction, registration) in order to be exploited for the determination of optimized wavelengths for leakage detection. Different data sets (soil reflectance and temperature) from WADI1 and WADI 2 campaigns were considered and a focus was made on trials and areas where known or intentional leaks were present. A series of maps of different indicators that are believed to reveal the presence of water (water indices: NDVI & OSAVI) are generated by the



trapezoid method using the Thermal infrared signal (TIR) combined with the VNIR signals. A series of 11 other indices were obtained by combining two or three reflectance maps in VNIR or SWIR bands. The determination of the optimized detection wavelengths is based on classification of water indices in function of possibility of discriminating two fields having presumably low and high moisture content and on the possibility of detecting artificial leaks. Based on these results it is recommended to select a combined TIR-VNIR remote sensing followed by a signal processing based on the triangle/trapezoid method.

- To check the validity of trapezoid method on images of the BUSARD campaign, the Esparron site was selected based on SCP information (low efficiency ratio) as well as on raw images of the IR channel. On this site of Esparron, overflowed in February 2017, high moisture areas were detected with WADI method and these results have been presented to the partners at the global meeting in Madrid (10 – 11 May 2017). SCP and ONERA decided in June to use acoustic method on this area and to dig to confirm the presence of water leaks. On the ground, puddles were found near the pipe as revealed by the WADI humidity maps and one connecting manhole was completely drowned. SCP carried out the investigation on different parts of the pipes equipped with acoustic microphones and recorders. The analysis of the signals and digging works were not conclusive, this method hasn't identified any water leak in the pipe. The origin of water was probably natural (spring discharge or transfer of water creek by layers ground...) even if the surface vegetation didn't reveal wet areas. The knowledge of the WADI context (topology of the places, geological data...) should avoid this kind of false alarms based on water leak detection results. The solution proposed by the WADI project for the optimization of water leak detection is the development of a water leak detection probability performance matrix, as a function of parameters such as infrastructure type, e.g. pressurized or gravity pipes; soil and vegetation type... (WP7).
- The airborne measurement campaigns using hyperspectral/IR BUSARD platform have been used as a basis to determine the optimized detection wavelengths. The development of WADI's innovative concept (based on the use of existing multi-spectral/IR cameras to replace complex and expensive hyperspectral system) led to the selection of existing (off-the-shelf) cameras operating at the defined wavelengths described above. Different data sets from WADI campaigns have been processed. The outcome is a series of maps of different indicators that are believed to reveal the water presence (water indices). In order to provide a water index with the triangle/trapezoid method, thermal infrared signal (8-12 μ m) combined with OSAVI index (one wavelength on each side of the red edge, between 0.65 μ m and 0.675 μ m and between 0.79 μ m and 0.87 μ m) is necessary. Other indices, obtained by combining two or three reflectance maps in VNIR or SWIR bands, were not selected because of their lower performance (S/N). A series of high level requirements has been defined. In Task 3.2, scenarios will be defined as well as detailed requirements. For the manned platform, the most promising



cameras will then be selected in Tasks 3.2 and 3.3 among those proposed in Annex 1 and purchased taking into account all relevant requirements of the application.

- An overview of measurement strategy has been provided for the continuation of the project. It is based on the nature of the effect observed, the surveillance constraints and requirements, the data processing method needs and the complementary use of aircraft and UAV platforms.

5 References

- Brigot G., Colin-Koeniguer E., Plyer A., Janez F., Adaptation and evaluation of an optical flow method applied to coregistration of forest remote sensing images, *IEEE J.Sel. Topics Appl. Earth Obs. Rem. Sensing*, 9(7) 2923-2939 (2016).
- Bryant, R.; Thoma, D.; Moran, S.; Holifield, C.; Goodrich, D.; Deefer, T.; Paige, G.; Williams, D.; Skirvin, S. Evaluation of hyperspectral, infrared temperature and radar measurements for monitoring surface soil moisture. In *Proceedings of the First Interagency Conference on Research in the Watersheds*, Benson, AZ, USA, 27–30 October 2003; pp. 528–533
- Carlson, T.N., Gillies, R.R., Schmugge, T. G., "An interpretation of methodologies for indirect measurement of soil water content", *Agricultural and Forest Meteorology*, 77, 191-205, 1995.
- Carlson T.N., "An overview of the triangle method for estimating surface evapotranspiration and soil moisture from satellite imagery", *Sensors*, 7, pp. 1612-1629 (2007).
- Chauhan N.S., Miller S., Ardanuy P., "Spaceborne soil moisture estimation at high resolution: a microwave-optical/IR synergistic approach", *Int. J. Remote Sensing* 24(22), 4599-4622 (2003) Krapez J.-C., Oliso A., Coudert B., "Comparison of three methods based on the temperature-NDVI diagram for soil moisture characterization", *Proc. of SPIE* 7472, 74720y, 1-12 (2009).
- Chen, D., Huang, J., & Jackson, T. J. (2005). Vegetation water content estimation for corn and soybeans using spectral indices derived from MODIS near-and short-wave infrared bands. *Remote Sensing of Environment*, 98(2), 225-236.
- Daughtry C.S.T., "Discriminating Crop Residues from Soil by Shortwave Infrared Reflectance", *Agronomy J.*, 93:125–131, 2001
- Fabre, S.; Briottet, X.; Lesaignoux, A. Estimation of soil moisture content from the spectral reflectance of bare soils in the 0.4–2.5 μm domain. *Sensors* 2015, 15, 3262–3281
- Gao, B. -C. (1996). NDWI—a normalized difference water index for remote sensing of vegetation liquid water from space. *Remote Sens. Environ.*, 58, 257– 266.
- Haubrock, S.N.; Chabrillat, S.; Lemmertz, C.; Kaufmann, H. Surface soil moisture quantification models from reflectance data under field conditions. *Int. J. Remote Sens.* 2008, 29, 3–29
- Kokaly, R. F., Asner, G. P., Ollinger, S. V., Martin, M. E., & Wessman, C. A. (2009). Characterizing canopy biochemistry from imaging spectroscopy and its application to ecosystem studies. *Remote Sensing of Environment*, 113, S78-S91.
- Krapez, J. C., Oliso, A., & Coudert, B. (2009, September). Comparison of three methods based on the Temperature-NDVI diagram for soil moisture characterization. In *Proc. of SPIE Vol (Vol. 7472, pp. 74720Y-1)*.
- Krapez, J. C., & Oliso, A. (2011, October). Improvement of the Triangle method for soil moisture evaluation by adding a third index: albedo or Cellulose Absorption Index. In *Proc. of SPIE Vol (Vol. 8174, pp. 81740L-1)*.
- Krapez, J. C., & Oliso, A. (2011). A combination of temperature, vegetation indexes and albedo, as obtained by airborne hyperspectral remote sensing, for the evaluation of soil moisture. *Quantitative InfraRed Thermography Journal*, 8(2), 187-200.
- Krapez J.-C., Chatelard C, Nouvel J.-F., Deliot P., "Combined Airborne Thermography And Visible-To-Near Infrared Reflectance Measurement For Soil Moisture Mapping", 11th Quantitative Infrared Thermography Conf., Naples, June 11-14, 2012.
- Lesaignoux A., Estimation de l'humidité de surface des sols nus à partir de l'imagerie hyperspectrale à haute résolution spatiale sur le domaine optique 0.4-14 μm , Thèse de l'Univ. de Toulouse, 16/12/2010.
- Maltese A., Cammalleri C., Capodici F., Ciralo G., la Loggia G., "Surface soil humidity retrieval using remote sensing techniques: a triangle method validation", *Proc. of SPIE* 7824, 782425, 1-8(2010)
- Moran M.S., Clarke T.R., Inoue Y., Vidal A., "Estimating Crop water deficit using the relation between surface air temperature and spectral vegetation index", *Remote Sensing of Environment* 49, 246-263 (1994).
- Peñuelas, J., Pinol, J., Ogaya, R., & Filella, I. (1997). Estimation of plant water concentration by the reflectance water index WI (R900/R970). *International Journal of Remote Sensing*, 18(13), 2869-2875

D3.1 Definition of optimal wavelengths and cameras



Rondeaux G., Steven M., Baret F., "Optimization of soil adjusted vegetation indices", *Remote Sensing of Environment*, vol. 55, 95-107, 1996

Sandholt I., Rasmussen K., Andersen J., "A simple interpretation of the surface temperature-vegetation index space for assessment of surface moisture status", *Remote Sensing of Environment* 79, 213-224 (2002).

Whalley, W.R.; Leeds-Harrison, P.B.; Bowman, G.E. Estimation of soil moisture status using near infrared reflectance. *Hydrol. Process.* 1991, 5, 321–327

Zarco-Tejada, P. J., & Ustin, S. L. (2001). Modeling canopy water content for carbon estimates from MODIS data at land EOS validation sites. *International Geoscience and Remote Sensing Symposium*, 2001. IGARSS '01, Vol. 1 (pp. 342–344).

Zarco-Tejada, P. J., Rueda, C. A., & Ustin, S. L. (2003). Water content estimation in vegetation with MODIS reflectance data and model inversion methods. *Remote Sensing of Environment*, 85(1), 109-124

6 Annex 1: Potential IR sensor candidates

							
Detector	MCT	SLS	MCT	MCT	Microbolometer	Microbolometer	Microbolometer
Spectral range	8 - 10.2 μm	7.5 - 9.5 μm	7.7 - 9.3 μm	7.7 - 9.3 μm	7.5 - 14.0 μm	7.5 - 14.0 μm	7.5 - 14.0 μm
Number of pixels	640 x 512	640 x 512	640 x 512	640 x 512	640 x 480	640 x 480	640 x 480
Detector pitch	16 μm	15 μm	15 μm	15 μm	25 μm	17 μm	17 μm
Sensor cooling	YES (stirling)	YES (stirling)	YES (stirling)	YES (stirling)	NO	NO	NO
Maximum frame rate (full frame)	100 Hz	125 Hz		230 Hz	60 Hz	50 Hz	50 Hz
Accuracy	+/-1 °C or +/-1 %	$\pm 2^\circ\text{C}$ ou $\pm 2\%$	+/-1 °C	1 K ou 1 % (°C)	$\pm 1.5\text{ K}$ ou $\pm 1.5\%$	$\pm 2^\circ\text{C}$ ou $\pm 2\%$	
NETD	< 40 mK	< 30 mK	< 30 mK	22 mK	< 30 mK	< 30 mK	50 mK
Integration/Response time	50 μs à 200 μs	480 nsec. à 687 sec.				Typical 8 ms	
Computer interface	GigE, USB	GigE	GigE	Camlink, GigE	GigE	GigE	GigE
Digitization	14 bit	14 bit	14 bit	16 bit	16 bit	16 bit	16 bit
Power consumption		< 50 W	< 50 W	50 W	~ 8 W		< 4.5 W
Optics	13 mm (43 x 35)°	13mm (40,5 x 33°)	12 mm	13 mm (32.9 x 40.9°)	15 mm (56.1 x 43.6°)	13 mm (45 x 34°)	15 mm
Size (mm)	250 x 160 x 123	200 x 100 x 100	186 x 136 x 146	320 x 198 x 135	190 x 90 x 94	216 x 73 x 75	49 x 49 x 77
Weight w/o lens	4.0 kg	2.3 kg	< 2,3 kg	< 8 kg	1.15 kg	0.9 kg	0.22 kg
Distributor	Distrame SA	FLIR	Noxant	TELOPS	Distrame SA	FLIR	STEMMER Imaging

Table 24 : Potential IR cameras candidates.

7 Annex 2: Potential VNIR/SWIR multispectral sensor candidates

							
Acquisition mode	Snapshot	Snapshot	Snapshot	Snapshot	Snapshot	Snapshot	Snapshot
Detector	Si CMOS	Si CMOS	Si CCD				CMOS
Spectral range	600 - 875 nm	380 - 1100 nm	380 - 1100 nm	480-550-660-720-830 nm	550-660-735-790 nm	530-570-660-790 nm	380 - 1000 nm
Number of spectral bands	25	4	6	5	4	4	4
Number of pixels	400*218	4x 1296*966	4x 1296*966	1280*960	4x 1280*960 pixels	4 x 1.2 Mpix	4x 1280*1024 pixels
Spectral resolution/Channel width	20 nm	20 nm	20 nm	10 - 40 nm	10 - 40 nm		
FOV				47.2° (f = 5.5 mm)	70.6° x 52.6°	67° x 53°	38.3° x 31°
SNR	39 dB	39 dB					
Pitch on the ground @ 800 ft (AGL)				16 cm	26 cm	22 cm (IFOV: 0.9 mrad)	13 cm
Swath width @ 800 ft (AGL)				213 m	345 m	323 x 243	168 x 134 m
Exposure time	0.1 - 1000 ms	0.1 - 1000 ms	0.1 - 1000 ms				
Frame rate	20 FPS	4 FPS	typ. 2 FPS (max. 10)	1 capture/s (all bands)	up to 2 FPS		
Shutter	Global	Global	Global	Global	Global	Global	
Digitization	10 bit	8 bit	8 bit	12 bit	10 bit		10 bit
Power	15 W @ 9-24 V	15 W @ 9-24 V	DC 15 W @ 9-24 V	5.0 V DC, 4 W nominal	8 W nominal (12 W peak)		
Weight	350 g	800 g	500 g	180 g	135 g	160 g	500 g
Size				121 x 66 x 46 mm ³	59 x 41 x 28 mm ³	78 x 121 x 61 mm ³	116 x 80 x 68 mm ³
Computer interface	USB, GigE	USB, GigE	USB, GigE	Serial, Ethernet, GPS			USB 2.0
Operating temperature	0°C to +40°C	0°C to +40°C	0°C to +40°C				0°C to +40°C
Manufacturer	Cubert	Cubert	Cubert	MicaSense	Parrot	Airinov	Tetracam
Remarq		4 sensors	6 sensors	5 cameras	4 cameras	4 cameras	

Table 25: Potential VNIR/SWIR multispectral sensor candidates

D3.1 Definition of optimal wavelengths and cameras



							
Acquisition mode	Push-broom	Snapshot	Snapshot	Sequential (filter wheel)	Snapshot	Push-broom	Push-broom
Detector				Si CCD	CMOS	MCT	MCT
Spectral range	400 - 1000 nm	600 - 1000 nm	450 - 800 nm	400 - 1000 nm	600 - 975 nm	964 - 2500 nm	900 - 2500 nm
Number of spectral bands	8	Approx. 20-25	7	8	25	256	166
Number of pixels		Up to 400*200		2456*2058	409*217 pixels (5 x 5)	320	384
Spectral resolution/Channel width	5 - 7 nm FWHM	12-15 nm				6 nm	
FOV	21° (f = 16 mm)	18° (f = 35 mm)		26.5° x 22.3° (f=18 mm)	18.3° x 9.8°	9° (f = 61 mm)	
SNR							
Pitch on the ground @ 800 ft (AGL)	8 cm	19 cm ?		4 cm	19 cm	12 cm	
Swath width @ 800 ft (AGL)	90 m	77 m		115 x 96 m	78 x 42 m	38 m	
Exposure time	0.1 - 300 ms	1 - 300 ms					
Frame rate	Up to 120 frames/sec	Up to 120 frames/sec		Up to 15 FPS	Up to 170 cubes/s	> 100 Hz	450 Hz maxi
Shutter			Global				
Digitization				12 bit	10 bit	14 bit	16 bit
Power	< 2 W	< 4 W			1.6 W	64 W @ 12 VDC	14.4 W
Weight	180 g (with lens)	180 g (with lens)	600 g	910 g	107 g	2.6 kg	2 kg (without lens)
Size	80 x 60 x 60 mm ³	80 x 60 x 60 mm ³	215 x 76 x 78 mm ³	136 x 124 x 116 mm ³	26 x 26 x 31 mm ³	152 x 127 x 76 mm ³	
Computer interface	USB 3.0	USB 3.0		Gig-E	USB3.0	Cameralink	Cameralink
Operating temperature	-20°C to +60°C	-20°C to +60°C					
Manufacturer	BaySpec	BaySpec	Sensilize	Pixelteq	Ximea	Corning	Headwall Photonics
Remarq					5x5 mosaic pattern		Stirling cooled

Table 26: Potential VNIR/SWIR multispectral sensor candidates (continuing and ending)